BREAKUP OF TURBULENT ROUND LIQUID JETS IN UNIFORM GASEOUS CROSSFLOW

By

RAMPRAKASH SANKARAKRISHNAN

Bachelor of Engineering in Mechanical Engineering

University of Madras

Chennai, Tamilnadu, India

2003

Submitted to the Faculty of the
Graduate College of the
Oklahoma State University
in partial fulfillment of
the requirements for
the Degree of
MASTER OF SCIENCE
December, 2005

BREAKUP OF TURBULENT ROUND LIQUID

JETS IN UNIFORM GASEOUS CROSSFLOW

Thesis Approved:

Dr. Khaled A. Sallam
Thesis Adviser

Dr. Afshin J. Ghajar

Dr. Frank W. Chambers

A. Gordon Emslie
Dean of the Graduate College

ACKNOWLEDGMENTS

I would like to acknowledge my advisor, Dr. Khaled A. Sallam, for his advice, guidance, support and encouragement during the period of this research at Oklahoma State University. I am also thankful to Dr. Afshin J. Ghajar and Dr. Frank W. Chambers for their advice and participation on the thesis committee. I would like to thank all the students working in my research laboratory for their help with building up this laboratory and for their assistance and co-operation during this research period, and all the staff of the School of Mechanical and Aerospace Engineering for their technical assistance. Finally, I would like to thank my parents for their love and support during my whole academic career.

This research was sponsored by the National Science Foundation (NSF) under Grant No. EPS-0132534 (Oklahoma - EPSCoR).

TABLE OF CONTENTS

Chapter Page

LIST OF TABLES

LIST OF FIGURES

Figure Page

Figure Page

LIST OF APPENDICES

Appendix Page

NOMENCLATURE

C_d	Drag co-efficient
C_i	Empirical constant for the SMD at onset of drop formation
C_l	Empirical constant for the size at the onset of ligament formation
C_t	Empirical constant for the time of onset of ligament formation
C_{xb}	Empirical constant for crosswise location of breakup of liquid column
C_{xi}	Empirical constant for the location of onset of ligament formation
C_y	Empirical constant for the SMD variation along the streamwise distance
C_{yb}	Empirical constant for time of breakup of liquid column
d_h	Hydraulic diameter
d_j	Jet exit diameter
d_l	Ligament effective diameter
d_p	Drop diameter
MMD	Mass median drop diameter of the spray
Oh_{Ld}	Ohnesorge number, $\mu_L / (\rho_L d_j \sigma)^{1/2}$
q	Liquid/gas jet momentum ratio, $\rho_L v_j^2/\rho_\infty u_\infty^2$
Re_{Ld}	Jet exit Reynolds number, $\rho_L v_j d_j / \mu_L$
SMD	Sauter mean diameter
SMD_i	Sauter mean diameter at the onset of breakup
t	Time
t_b	Time taken for the streamwise breakup of liquid column

t_{bi}	Time at onset of bag formation
t_i	Time at the onset of breakup
t^*	Aerodynamic characteristic time, $d_j (\rho_L/\rho_\infty)^{1/2} / u_\infty$
t_v^*	Characteristic viscous time, d_j^2/ν_L
u	Mean streamwise velocity
u_L	Characteristic liquid phase velocity
v_j	Average jet exit velocity
v_{surf}	Jet surface velocity
v'	Cross stream velocity fluctuation
v_λ	Turbulent eddy characteristic cross stream velocity
We_∞	Crossflow Weber number based on jet exit diameter, $\rho_\infty d_j u_\infty^2/\sigma$
We_{Ld}	Weber number based on jet exit diameter, $\rho_L d_j v_j^2/\sigma$
$We_{L\Lambda}$	Weber number based on jet exit radial (cross stream) integral length scale, $\rho_L \Lambda v_j^2/\sigma$
x	Crosswise distance from the jet exit
x_b	Crosswise distance of the end of liquid core
y	Streamwise distance from the jet exit
y_i	Length to initiate turbulent primary breakup

Greek

Δt	Pulse separation
λ	Turbulent eddy length scale
Λ	Radial (cross stream) integral length scale
μ_L	Liquid molecular viscosity
ν	Kinematic viscosity

ρ_L	Liquid density
ρ_∞	Gas density
σ	Surface tension

Subscripts

i	Onset property
j	Jet exit property
L	Liquid property
∞	Gas property
l	Ligament property
p	Drop property
surf	Surface property

Superscripts

$(')$	Fluctuation of quantity
$(\bar{})$	time average of quantity

CHAPTER I

INTRODUCTION

1.1 General Statement of the Problem

1.1.1 Background

Breakup processes along the free surface of round turbulent liquid jets in uniform air crossflow were studied experimentally due to its importance in various industrial and natural processes, e.g., spray breakup in aircraft propulsion systems, liquid rocket engines, diesel engines, spark ignition engines and agricultural sprays, among others.

Liquid jet primary breakup in crossflow is a simple classical flow that is influenced by aerodynamic effects and must be understood in order to provide a background for other more complex spray atomization processes. Initial studies of liquid jet in crossflow have been mainly focused on trajectories and penetration of liquid jets. Additional details about the properties of round nonturbulent liquid jets in gaseous crossflow were recently obtained by Wu et al. (1997), Mazallon et al. (1999), and Sallam et al. (2004) and references cited therein.

Past work on turbulent liquid jets in still gases showed considerable aerodynamic effects on turbulent primary breakup (Wu and Faeth, 1993) for liquid/gas density ratios less than 500. Moreover, Wu et al. (1995) concluded that for nonturbulent slug flow with boundary layer removal at the inlet to the constant diameter section involving $L/d > 4 – 6$ and jet exit Reynolds numbers $> 1.4 \times 10^4$, the turbulent primary breakup regime was independent of the aerodynamic effects for density ratios in the range 104 – 7240.

Recently, Aalburg et al. (2005) investigated the breakup of turbulent liquid jets in uniform gaseous crossflow, and provided measurements of the surface properties including properties at the onset of breakup, ligament and drop sizes, drop velocities after breakup and the rates of breakup, but the liquid turbulence was considered at the limit of fully developed turbulent pipe flow. However, most practical injectors, e.g., jet engine afterburners, introduce partial level of liquid turbulence whose effects on breakup must be understood.

In contrast to liquid jets in crossflow, gas jets in crossflow have been studied extensively and the internal and external flow fields have been detailed by (Andreopoulos and Rodi, 1984), Chu (1985) and (Sherif and Pletcher, 1989) through the use of hot-wire probes and hot wire anemometers. Measurements involved turbulence characteristics including mean and fluctuating velocity components, Reynolds stresses, correlation coefficients, and turbulent kinetic energy.

1.1.2 Problem Statement

The objectives of the current investigation were to perform experimental investigation of primary breakup of partially and fully turbulent round liquid jets in uniform gaseous crossflow, to confirm the recent results of Aalburg et al. (2005) for the breakup of fully developed turbulent liquid jets in uniform crossflow, and to interpret and correlate new measurements using phenomenological analyses. Present experiments involved the use of round nozzles having smooth rounded entrances and length to diameter ratios greater than 40:1 to help insure fully developed pipe flow at the jet exit (Wu et al., 1995). Instrumentation involved use of pulsed shadowgraphy, photography

and high speed imaging. Present experimental methods were similar to past studies of nonturbulent primary liquid jet in crossflow (Sallam et al., 2004).

1.2 Previous Related Studies

1.2.1 Turbulent Liquid Jets in Still Gases

The breakup of turbulent liquid jets in still gases, termed primary breakup, have been studied extensively, see Wu et al. (1992) and references cited therein. The onset of turbulent primary breakup occurred at a distance from the jet exit but approached the exit at large liquid Weber numbers and the scales of liquid surface distortions increased with increasing distance from the jet exit. Ligament-like structures protruding from the liquid surface experienced little effect of drag from the gas phase implying weak aerodynamic effects on turbulent primary breakup. Investigation on the aerodynamic effects on the primary breakup of turbulent liquid jets (Wu and Faeth, 1993) showed aerodynamic enhancement on onset of breakup, and effects on drop sizes and velocities, when the liquid/gas density ratio was less than 500. It was further found that initial flow conditions affected the breakup of liquid jets (Wu et al. 1995). The removal of the boundary layer from the flow contraction regions lead to nonturbulent jets with no initiation of atomization. Transition from nonturbulent jets to turbulent jets occurred by increasing the nozzle L/d ratios.

Recent studies of plane and round turbulent liquid jets in still gases at large liquid/gas density ratios (Sallam et al., 1999, 2002) provided surface breakup properties including flow visualizations, liquid surface velocities, onset of breakup, drop and ligament size distributions, drop and ligament velocities, and the rates of drop formation.

It was concluded that the formation of ligaments and irregularities on the surface are due to turbulence developed in the injector passage and not due to the aerodynamic effects.

Another area of interest is the breakup of the liquid column as a whole. The liquid column breakup length [Chen and Davis (1964) & Grant and Middleman (1966)] is important because it defines the start of fully dispersed multiphase flow region. Breakup regimes of turbulent liquid jets in still gases were defined by Wu and Faeth (1995) as column breakup (1^{st} wind induced breakup) and surface breakup (2^{nd} wind induced breakup). Recently, Sallam et al. (2002) defined three different breakup modes, within the column and surface breakup regimes, namely Rayleigh-type breakup, turbulent breakup and the turbulent bag/shear type breakup.

1.2.2 Non-Turbulent Liquid Jets in Crossflow

Initial studies focused on liquid column penetration and breakup length, (Geary and Margettes, 1969; Reichenbach and Horn (1971); Schetz and Padhye, 1977;) of liquid jets in subsonic air streams and indicated that the drag coefficient remained a constant for a given freestream conditions and injector geometry. Experimental results for the spray penetration (defined as the largest transverse distance attained by a given spray plume) by Wu et al. (1998) showed an increase in the spray penetration with increased liquid/gas momentum ratio and the cross stream distances. This fact was supported by (Birouk et al., 2002) who found out that the transverse penetration is a linear function of the square root of the liquid/gas momentum ratio. A later investigation of breakup of liquid jets in subsonic crossflow by Wu et al. (1997) classified liquid breakup into surface breakup regime and column breakup regime based on the liquid/gas momentum ratio and the

crossflow Weber number. Moreover, when the liquid/gas momentum ratio was large, the liquid jet undergoes surface breakup before the development of large scale surface waves. Also for more viscous liquids these waves were more prominent. A correlation for the drag coefficient based on the phenomenological analyses for the liquid jet trajectories was also developed. Though no measurements regarding the surface breakup properties or the drop and ligament sizes were made, this work provided a foundation for the investigation of liquid core breakup for future works. Mazallon et al. (1999) conducted experimental investigation of primary breakup of nonturbulent liquid jets in gaseous crossflow. The measurements included jet primary breakup regime transitions, jet deformation properties, time at the onset of primary breakup, and liquid and column surface waves. For small Ohnesorge number ($Oh_{Ld} < 0.1$), the breakup regime transitions were entirely controlled by the crossflow Weber number. It was found that primary breakup of round nonturbulent liquid jets in crossflow is analogous to the secondary breakup of the individual drops. Liquid column deformation before the onset of breakup was observed for various breakup regimes with the liquid column attaining the frontal diameter roughly twice the jet exit diameter. This result was later revisited by Sallam et al. (2004) where it was shown that the liquid jet deformation was limited to the bag breakup regime whereas in the shear breakup regime, there was no such deformation associated with the onset of breakup. Moreover, the crossover of the deformation to the no-deformation region occurred at the multimode breakup regime. Experimental work of Sallam et al. (2004) also investigated drop and ligament properties and showed that drop formation follows the Rayleigh breakup mechanism. The ligament formation was categorized into (1) a transient regime where the thickness of the viscous shear layer

within the liquid jet is growing as a function of time and (2) a quasi-steady regime where the growth of viscous shear layer within the liquid jet becomes limited by the liquid jet diameter. Experimental study of liquid jets in crossflow (Birouk et al., 2003) with lubricating oil as the test liquid with different range of liquid viscosities observed two major breakup regimes for low range of liquid jet Reynolds number, namely arcade (column) breakup and bag breakup. Their main conclusions were that liquid jet viscosities had no effects on the breakup mechanisms of liquid jets in crossflow, but plays an important role on the regime transition boundaries.

1.2.3 Turbulent Liquid Jets in Crossflow

Fuller et al. (2000) employed pulsed photography to ascertain column trajectories and the turbulent liquid column fracture locations, column waves and near spray characteristics for various injection angles. Their results showed two major breakup regimes for the column breakup processes known as the aerodynamic breakup regime and the non-aerodynamic breakup regime based on a breakup regime parameter (T_b). Their results showed that a reduction in the injection angle for a constant value of subsonic crossflow Mach number and liquid/gas momentum ratio caused a decrease in the overall penetration causing the inhibition of atomization process and thereby making the spray less uniform. The analysis of liquid column trajectories were performed in the same manner as Wu et al. (1997) and the results showed a much higher value of the drag co-efficient which were also much larger than that for a flow over a solid cylinder. Though no specific reasoning could explain such a difference, the results were attributed to the thinning of the boundary layer, which may be due to the nozzle design. Results for

column fracture revealed different correlations for both aerodynamic breakup and non-aerodynamic breakup. The crossover between aerodynamic and non-aerodynamic breakup was found to occur at a value of the breakup regime parameter equal to unity.

Experimental studies by Aalburg et al. (2005) employed round injectors with L/d ratios greater than 100 to provide fully developed turbulent pipe flow at the jet exit. Test conditions were limited to liquid/gas density ratios greater than 500 and provided various surface breakup properties and measurements. The results for the onset of turbulent primary breakup and the drop size measurements for jets in still air and crossflow agreed with the results for turbulent jets in still air by Wu et al. (1992). These results confirm the dominance of turbulent primary breakup over the aerodynamic effects. Measurements of ligament sizes along the streamwise distances, drop velocities after primary breakup, and liquid breakup rates were also included.

1.2.4 Breakup Outcomes

In addition to the primary breakup of liquid jets, the secondary breakup of drops could affect the breakup outcomes. Shock wave disturbances (Hsiang and Faeth 1992, 1993, 1995) were considered to provide a step change in the ambient environment of the drop simulating the conditions experienced by drops at the end of primary breakup. Experimental and analytical results of (Ranger and Nicholls, 1969) for the problem of liquid drop shattering indicated that breakup was observed to occur as a result of the interaction between drop and convective flow field established by the passage of shock over it. The collision of the incident shock on the drop has insignificant effect on the breakup of the drop and thus the problem reduces to a droplet in high speed flow.

Experimental results of Schetz and Padhye, (1977); who employed streak photography and spark shadowgraphy; on penetration and breakup of liquids in subsonic flows showed that for a given injector and freestream condition the droplet size was not affected greatly by the mass flow rate but was greatly affected by the injector geometry. Hsiang and Faeth (1992, 1993, 1995) found the conditions required for the initiation of deformation and breakup regimes, the times required for the onset and end of breakup, the drag properties of deformed drops, and the drop size and velocity distributions at the end of breakup process.

The size distributions of drops produced by breakup of both turbulent liquid jets in still air (Wu et al., 1992, Wu and Faeth, 1993, 1995) and nonturbulent slug flow (Wu et al., 1991) satisfied Simmons' (1977) universal root normal distribution function at each instance of time. Drop size distribution after primary breakup implied that most drops are subjected to secondary breakup (Wu et al., 1991). For nonturbulent liquid jets in crossflow the drop sizes after primary breakup tended to vary with increasing distance from the jet exit and then approached a constant value. The drop sizes for fully turbulent liquid jet breakup in crossflow (Aalburg et al., 2005) correlated well with the viscous layer thickness generated by the crossflow. The drop sizes increased with increasing streamwise distances similar to the results obtained for fully turbulent jets in still air.

From the above literature review, it is evident that there is little information on the effects of partial level of liquid turbulence on the breakup properties. The missing information includes conditions for onset of breakup, ligament and drop properties along the liquid surface, drop sizes after breakup, liquid column breakup lengths and column

trajectories. This is unfortunate because the missing informations are important to understand the effects of crossflow on primary breakup of turbulent jets and to provide a basis for modeling multiphase flows in most practical fuel injectors.

1.3 Specific Objectives

In view of the current status of understanding of breakup of round turbulent liquid jets in gaseous crossflow, the specific objectives of the present study are as follows:

1. Undertake an experimental investigation of breakup of partially and fully turbulent round liquid jets in uniform crossflow. This includes developing a breakup regime map, identifying conditions at the onset of breakup, measuring drop properties at onset of breakup and along the liquid surface.
2. Study the properties of ligaments along the liquid surface jets and investigate earlier theories of Rayleigh breakup mechanism (Wu et al., 1992) in the formation of drops from the ligaments.
3. Study the breakup lengths of turbulent round liquid jets in crossflow, within column, bag, multimode and shear breakup regimes.
4. Study liquid column trajectories for bag, multimode and shear breakup regimes.
5. Use phenomenological analyses to interpret and correlate new measurements, and to provide more understanding of the interaction of the liquid turbulence and the gaseous crossflow.

1.4 Organization of the thesis

The thesis is organized into four chapters and two appendices. The statement of the problem and specific objectives of the present investigation have been presented in this chapter. The second chapter describes the experimental methods used during the present study. The results concerning liquid surface breakup are discussed in the third chapter. The summary and main conclusions of the present investigation, including recommendations for future study, are presented in the fourth and final chapter. The appendices provides tabulations of experimental data and experimental uncertainties.

CHAPTER II

EXPERIMENTAL METHODS

2.1 Test Apparatus

The test apparatus employed during the present study was a round jet apparatus. It was designed to investigate the properties of primary breakup of turbulent liquid jets. This test apparatus will be described in the next two sections.

2.1.1 Liquid Jet Apparatus

A sketch of the round jet apparatus installed over the wind tunnel test section is shown in Fig. 2.1. The test liquids were fed from the cylindrical storage test chamber using pressurized air, into a round nozzle vertically downward into the air crossflow flowing from left to right, generated by a wind tunnel.

The storage chamber (shown in Fig. 2.2) had an inside diameter and length of 76.2 and 165.1 mm, respectively. The top part of the storage chamber was fitted with a top flange (shown in Fig. 2.3) that was secured with 8 screws to the cylindrical storage chamber. The lower part of top flange was connected with a baffle. The top flange had two ports for the air lines and one port for the liquid fill line. The liquid fill line was connected to a ball valve that could be opened or closed after filling in the test liquid into the cylindrical chamber. The bottom part of the cylindrical chamber was fitted with a flange that contained the nozzle. The nozzle (shown in Fig. 2.4) had a smooth rounded

entrance (radius of curvature equal to the nozzle passage diameter) followed by round constant area passage having length-to-diameter ratio greater than 40:1 to help insure fully-developed pipe flow at the jet exit.

The nozzle used in the present investigation was a 2 mm round nozzle made of 304 Stainless Steel. The nozzle was calibrated in order to find a relationship between the liquid jet exit velocity and the operating pressure. This was important because to achieve a particular liquid jet Reynolds number, the liquid jet velocity had to be known and for this the air tank had to be pressurized accordingly using the air compressor. To calibrate the nozzle the air tank was pressurized to a certain value of pressure that could be read from the dial gage (Heise, Model CM), connected to the air tank. The liquid jet was injected by opening the solenoid valve using a pulse generator to admit high pressure air into the test chamber. The volumetric flow rate was measured using a stop watch and a laboratory grade graduated cylinder made of polypropylene of capacity 1000 ml with a subdivision of 1 ml. The nozzle jet exit velocity was found as follows:

$$v_j\ (\text{m/s}) = \frac{\Delta V}{A_j \text{ x } t} \tag{2.1}$$

where, ΔV = volume of the fluid collected (m^3)

A_j = exit area of the nozzle (m^2)

t = time taken for collecting the fluid (s)

The calibration was completed by repeating the same procedure for different settings of air tank pressure and a plot as shown in Fig. 2.5 is obtained. Also shown in the plot is the fit for the theoretical velocity (ignoring any losses) determined using the following:

$$v_j\,(\text{m/s}) = \sqrt{\frac{2\Delta P}{\rho_L}} \tag{2.2}$$

where, ΔP = the pressure of injection of the liquid (psi)

ρ_L = the density of the injecting liquid (kg/m^3)

Using this calibration plot for any value of the air tank pressure, the jet exit velocity could be determined and therefore the jet exit Reynolds number (Re_{Ld}) can be calculated.

2.1.2 Crossflow Generation

The crossflow was generated using a subsonic wind tunnel manufactured by Engineering Laboratory Design Inc. The wind tunnel had a 16:1 contraction ratio and a test section cross sectional area of 0.3 x 0.3 m^2. The test section velocity at normal temperature and pressure ranged from 3 m/s to 62.5 m/s with less than $\pm$ 1% variation from the mean free stream velocity, and the turbulence level in the test section was estimated to be less than 0.25%. Variation in the test section velocity is responsible for achieving the wide range of crossflow Weber number mentioned later under test conditions. Test section side-walls and floor were removable and made of float glass for optical accessibility. The ceiling had a provision for mounting the test chamber and nozzle assembly supported by unistrut frames built around the test section. The side elevation of the wind tunnel is shown in Fig. 2.6. A pitot static tube (United Sensors Model PDC-18-G-16-KL) was fitted to the end of the test section at the centerline. The pitot static tube was connected to an inclined tube 0 – 10" H_2O manometer (Dwyer Model No. 400-10-Kit) though two clear plastic tubes.

The 12” x 12” subsonic wind tunnel used in the present study was calibrated in order to confirm the factory calibration in terms of a relationship between the operating frequency and the mean test section velocity (u_∞). The calibration was performed using the pitot static tube and the inclined tube manometer. The wind tunnel was turned on and the frequency was set on the control panel. The pitot static tube was positioned in the center of the test section facing the flow direction. The deflection on the manometer was recorded in terms of inches of water (Δh_w) and then using the Eqn. (2.3) the mean velocity in the test section was calculated.

$$u_\infty = \sqrt{\frac{2 \text{ x } (\Delta h_w \, \rho_w \, g)}{\rho_\infty}} \tag{2.3}$$

where, ρ_w = density of water (kg/m^3)

ρ_∞ = density of air (kg/m^3)

g = acceleration due to gravity (9.81 m/s^2)

The mean test section velocity was used to find the crossflow Weber number, We_∞. The same procedure was repeated for different settings of wind tunnel frequencies and the calibration was completed. The velocity was found to range between 3 m/s – 65 m/s for an operating frequency range of 3.1 Hz to 61 Hz. The relationship between the wind tunnel operating frequency and the mean test section velocity is shown in Fig. 2.7. For any specific value of the test section velocity, the corresponding frequency can be determined by the following:

$$\text{Frequency} = 0.67 + 0.80 \, u_\infty - 6.69 \text{ x } 10^{-5} \, u_\infty^2 \tag{2.4}$$

The above calibration procedure was carried out at a room temperature of 19.5 °C and an atmospheric pressure of 29.9 inches of mercury. A temperature variation of ± 5 °C and a pressure variation of ± 0.2 inches of mercury would result in the air density variation of < 1% from the present test conditions.

2.2 Instrumentation

Instrumentation consisted of performing single-pulse and double-pulse shadowgraphy, photography, digital shadowgraphy and high speed imaging. Table 2.1 summarizes the shadowgraphic recording/instrumentations. The light sources for these optical techniques were two frequency-doubled Nd:YAG lasers (Spectra Physics model LAB SERIES 150-10, 532 nm wavelength, 8-10 ns pulse width, and up to 300 mJ per pulse) that could be controlled to provide pulse separations as small as 100 ns. The lasers, camera, the timing of the firing of the liquid jet and the firing of the optical system were controlled by a 8-channel pulse generator (Quantum Composers, Model 9518) that has a 10 ns resolution and a control of delay ranging from 0 – 5000 sec. The capture of shadowgraph images were done with an open shutter camera under complete darkroom conditions so that the laser pulse width controlled the exposure time of the camera and was short enough to freeze the liquid surface and drop motion. These techniques are discussed in the following sections.

2.2.1 Single-Pulse and Double-Pulse Shadowgraphy

Pulsed shadowgraphy technique was used to visualize the flow regimes, find the locations of the onset breakup, measure ligament and drop sizes, mean liquid column

breakup lengths, and mean streamwise liquid surface velocities among others. The arrangement for single and double-pulse shadowgraphy is shown in Fig. 2.8. The laser beams after passing through a series of mirrors were expanded and passed through a pinhole to provide beam diameters equal to that of the diameter of the collimating lens, that passed through the region being observed. This collimated beam after passing through the relay lens forms a real and inverted image of the object lying in the region of observation. The region of observation in the present study was the jet exit plane. The shadowgraphs were recorded using a Polaroid black and white film (Type-55) of dimensions 100 mm x 125 mm at magnifications up to 3:1. A typical single-pulse shadowgraph is shown in Fig. 2.9 (a).

For a double-pulse shadowgraphy, two laser light sources having different pulse strengths were used to resolve the directional ambiguity. The laser output beam strength was controlled using a quarter wave plate. An image taken from a double pulse shadowgraphy technique is shown in Fig. 2.9 (b). Data obtained from the shadowgraphs were digitally scanned and analyzed using the Sigmascan software developed by Systat software Inc. and the Tracker software developed by NASA. This software allowed drops as small as 8 μm diameter to be observed and as small as 35 μm diameter to be measured with 10% accuracy.

The measurements involved averaging of several pulsed shadowgraph images in order to minimize the uncertainties in measurements. Measurements of onset of breakup involved identifying the first ligament formed at the liquid surface along the streamwise direction that has at least a length to diameter ratio equal to two. Measurements of drop sizes at onset were based on locating the first drop being formed and then calculating the

diameter assuming that the drop being formed is spherical. Ligament sizes were measured by averaging the diameters at 4 different points on a ligament and then averaging over same test conditions. In all test cases, sampling limitations dominated the experimental uncertainties.

2.2.2 Photography

To measure the large breakup lengths, the laser beam was expanded into a large volume and by employing suitable technique, the beam was scattered immediately before lighting the portion of the jet being observed. The portion of the jet was captured using a pco.2000 CCD camera manufactured by Cooke corporation, having a resolution of 2048 x 2048 pixel array and running at 15 fps at full resolution to obtain a conventional photograph. These photographs were then digitally scanned for further measurements. Again the imaging was done in a completely dark room so that the laser pulse duration controlled the exposure time and was short enough to freeze the liquid surface motion.

High speed imaging was performed using a CMOS camera (IDT's XS-4) at a maximum frame rate of 5180 fps at a 512 x 512 pixels resolution. A halogen lamp was used as a light source to illuminate the target while recording the images.

2.2.3 Digital Shadowgraphy

Digital shadowgraphy is very similar to the aforementioned pulse-shadowgraphy technique, the difference lies in the image capturing unit. Unlike in conventional pulsed shadowgraphy technique where the image is captured on a Polaroid film, in digital shadowgraphy a CCD camera is used to focus on the plane of image formation and

capture the image formed therein. The CCD camera is synchronized with the laser firing and the pressurized liquid jet injection using a pulse generator. As in the aforementioned imaging techniques, digital shadowgraphy is also performed in a completely dark room so that the laser pulse duration controls the exposure time of the CCD camera thereby freezing the liquid surface motion.

2.3 Experimental Procedure

The experimental procedure consisted of the following steps: filling the storage chamber with the test liquid, generating the crossflow, injecting the test liquid, and firing the optical system. The test liquid was filled in the storage chamber through the liquid fill line valve. Crossflow was generated by turning on the wind tunnel and setting the frequency on the control panel to achieve the desired test section velocity. The liquid was injected through the nozzle by admitting high-pressure air actuated by a solenoid valve (ASCO Red Hat, 3/4", 25-750 psig), through the two air line ports as mentioned earlier. The baffle positioned close to the air inlet prevented undesirable mixing between the air and the test liquid. The high-pressure air was stored in a horizontal cylindrical air tank (Niles Steel tank) made of carbon steel having a volume of 0.18 m^3 and placed on the upstream side of the solenoid valve with provision for the tank air pressure up to 10 MPa. Air is filled in the air tank using an oil-free breathing air compressor (RIX Industries, Model SA-3E) with a rating of 3300 psig.

The nozzle assembly was mounted on the top of the wind tunnel test section in such a way that it is flush mounted with the ceiling of the test section.

The test liquid was injected for 100-1500 ms, that were long compared to flow development times of 2-10 ms. Present optical measurements required less than 0.1 ms for triggering and data acquisition and were comparatively smaller than the flow development times.

2.4 Test Conditions

Present experimental study involved measurements of properties for round partially- and fully-developed turbulent jets in uniform gaseous crossflow. Present investigations employed water, ethyl alcohol (190 proof) and glycerol (44% glycerin by mass) injected into still air and crossflow.

Past studies have shown that any effect of variations of liquid and gas properties on the test results can be represented by the dimensionless parameters (Wu et al., 1992; Wu and Faeth, 1993, 1995; Sallam et al., 2004).

Table 2.2. gives the summary of test conditions for round jet. The test liquids as mentioned before were used with jet exit diameters of d_j = 2.01 mm, jet exit velocities of v_j = 8 – 60 m/s and cross stream Weber numbers of We_∞ = 0 – 180. Liquid properties were measured as follows: liquid densities using a set of precision hygrometers (Fisher Model 11-582, 0.1% accuracy), liquid viscosity using a Cannon-Fenske viscometer (Fisher Model 13-617, 1% accuracy), and surface tension using a ring tensiometer (Fisher Model 20, 1% accuracy). Denoting liquid and gas properties with subscripts L and ∞, the liquid/gas density ratios were ρ_L/ρ_∞ = 820, 665 and 938 for water, ethyl alcohol and glycerol respectively. Other physical properties, e.g., absolute viscosity (μ_L) and surface tension (σ), are also summarized in Table 2.2 for air, water, ethyl alcohol and glycerol.

The jet exit dimensionless parameters, defined in Table 2.2, are as follows: Reynolds numbers, Re_{Ld} = 2,200 – 140,000; Weber numbers, We_{Ld} = 1000 – 105,000; and Ohnesorge numbers, Oh_{Ld} = 0.0020 – 0.014. The jet exit Reynolds number range covers partially and fully turbulent primary breakup regimes and also the transitional range. The small jet exit Ohnesorge numbers, which is defined as the ratio of viscous forces to the surface tension forces, imply that effects of viscous forces on liquid breakup were small (see Hsiang and Faeth (1992, 1995), Faeth (1996)). Present investigations of round turbulent liquid jets were compared with the results of nonturbulent liquid jets in crossflow by Sallam et al. (2004). Experimental methods and measurement techniques used in them were similar to those used in the present investigations.

2.5 Repeatability of Experiments

To validate the present instrumentation and measurement techniques, the liquid jet surface velocities were measured and compared with the experimental results available in the literature for liquid jets injected in still air as well as in crossflow (Sallam et al., 2004, Aalburg et al., 2005). Double pulse shadowgraphy technique was employed to capture two images with very short time interval (t = 12 μs – 15 μs). Measurements of liquid surface velocities were based on motion of particular points on the base of the ligaments formed on the liquid jet surface. The variation of mean liquid surface streamwise velocities is plotted against streamwise distance from the jet exit as shown in Fig. 2.10. The measured velocities shown in the plot are time averaged streamwise liquid surface velocities normalized by the jet exit mean velocity. It was found that for present

test conditions, the ratio of $\overline{v}_{surf}/v_j$ was independent of the streamwise distances from the jet exit and was found to be:

$$\overline{v}_{surf}/v_j = 1.0 \tag{2.5}$$

Thus, the mean streamwise liquid surface velocity is equal to the mean liquid streamwise jet velocity at the jet exit. Within experimental uncertainties, this result is in good agreement with the results for nonturbulent liquid jets in crossflow (Sallam et al., 2004) and fully turbulent liquid jets in crossflow (Aalburg et al., 2005).

Table 2.1 Shadowgraphic Recording Equipment/Instrumentation

Component	Manufacturer/Seller	Model	Description
Nd-YAG laser	Spectra Physics	LAB 150-10	532 nm wavelength
Polarized Cube beam splitter	Newport Corp	10BC16PC.3	532 nm, 25.4 mm
Objective lens	Newport Corp	M-20x	20x beam expander
Pin hole	Newport Corp	910PH-25	25 micron, high energy pinhole
Object beam collimating lens	Newport Corp Edmund Optics	KPX226 AR.14 NT32-973	76.2 mm dia, 150 mm focal length 50.8 mm dia, 100 mm focal length
Object beam relay lens	Newport Corp Edmund Optics	KPX232 AR.14 NT32-975	76.2 mm dia, 300 mm focal length 50.8 mm dia, 50 mm focal length
Polaroid Camera Bellows	Henrys.com	—	For 100 mm x 125 mm Polaroid film holders.
Polaroid sheet film holder	Polaroid	545 Pro	100 mm x 125 mm Black
Film	Polaroid	Type-55	Black & White, 100 mm x 120 mm sheet film
Camera lens	Nikon	NI501 4DAF NI1052 8DMAF	50 mm f/1.4D 105 mm f/2.8D
Bellows	Nikon	NIPB6 PB-6	48-208 mm extension range
CCD Camera	Cooke Corp	PCO.2000	2048 x 2048 pixels, 15 fps, double shot with 400 ns interframe time
CMOS Camera	IDT Inc.	XS – 4	512 x 512 pixels, 5180 fps
Optical Table	Newport Corp	RS 2000	—
Computer	Intel	Pentium 4	3.6 GHz, 3.25 GB RAM
Image processing software	Systat Inc	Sigmascan Pro 5	—

Table 2.2 Summary of Test Conditions[a]

Liquid	Water	Ethyl Alcohol	Glycerol (44%)[b]
ρ_L (kg/m^3)	997	806	1140
ρ_L/ρ_∞	820	690	938
μ_L x 10^4(kg/ms)	8.94	12.3	57.5
σ x 10^3(N/m)	70.8	27.0	67
d_j (mm)	2.01	2.01	2.01
v_j (m/s)	5-60	8-29	5-15
Re_{Ld} x 10^{-3}	11-140	11-40	2-6
We_{Ld} x 10^{-2}	6-1050	38-532	10-74
Oh_{Ld} x 10^4	23	57	143
We_∞	0-180	0-161	0-161

[a]Pressurized injection of round liquid jets vertically downward in horizontal crossflow at 99±0.5 kPa and 297±1 K (ρ_g = 1.215 kg/m^3 and ν_g = 15.2 mm^2/s). Round injector with a rounded entry and a length-to-diameter ratio of greater than 40:1.

[b]Percentage of glycerin by mass in parenthesis.

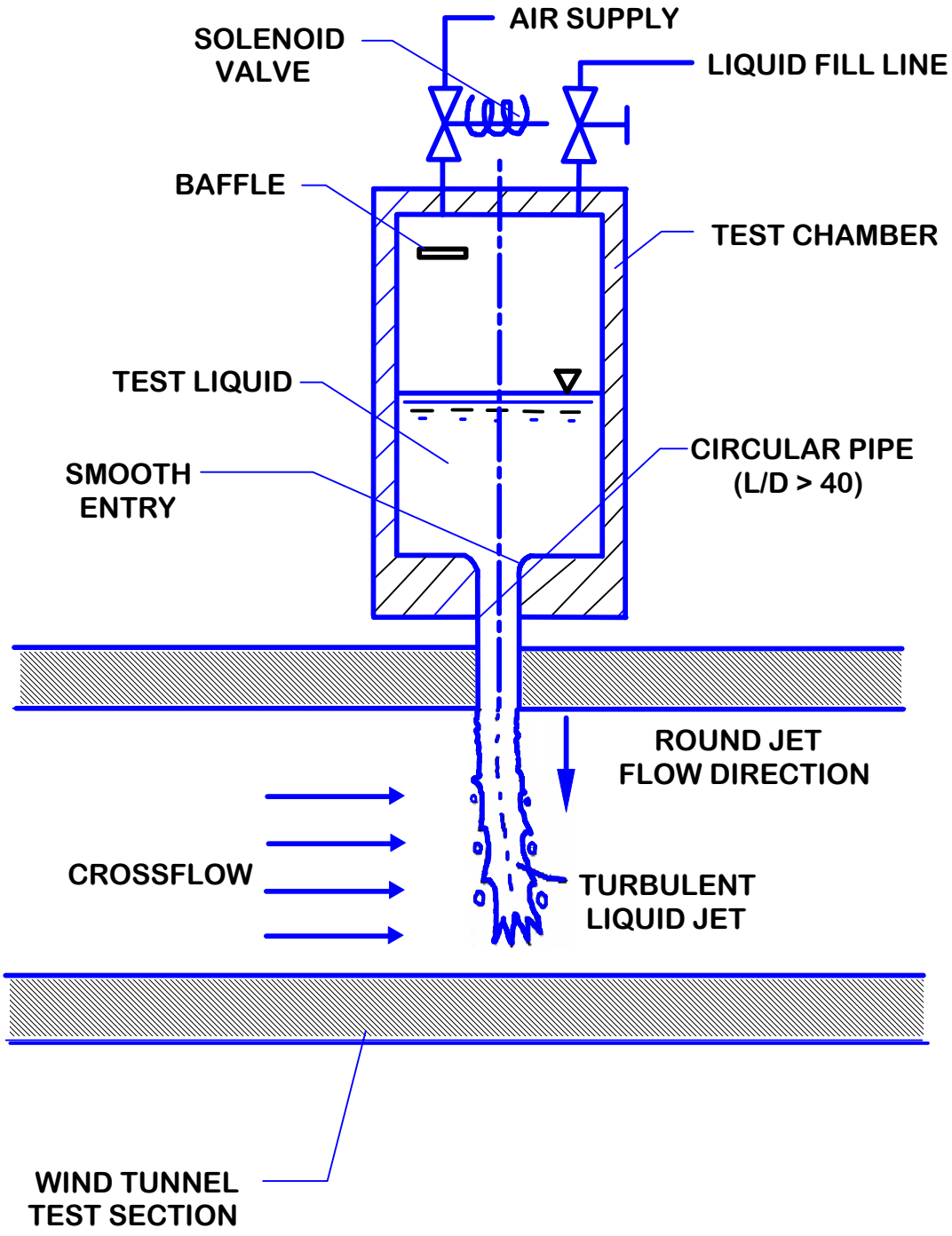

Fgure 2.1 Sketch of the turbulent liquid jet in crossflow.

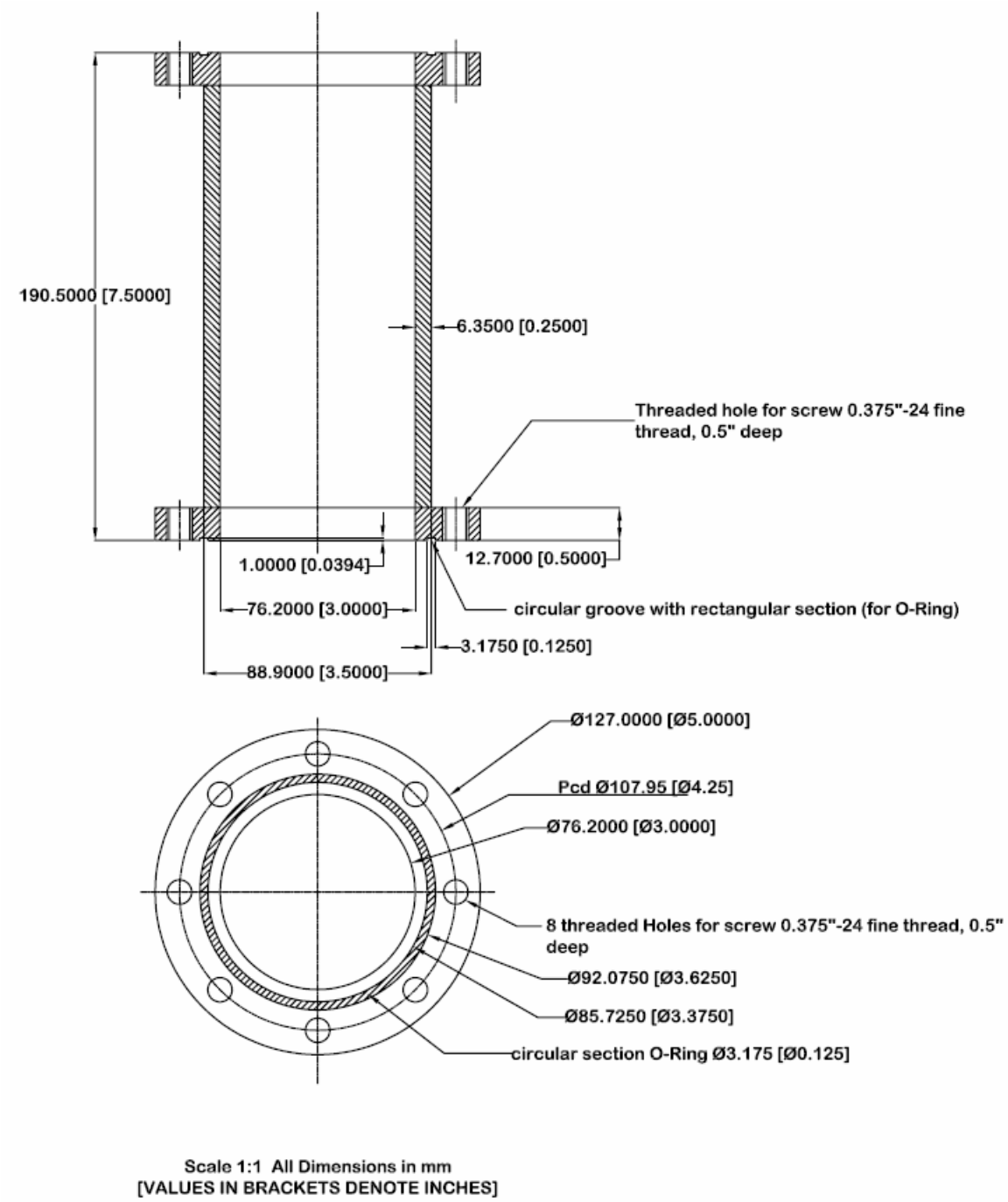

Figure 2.2 Sketch of the cylindrical storage test chamber.

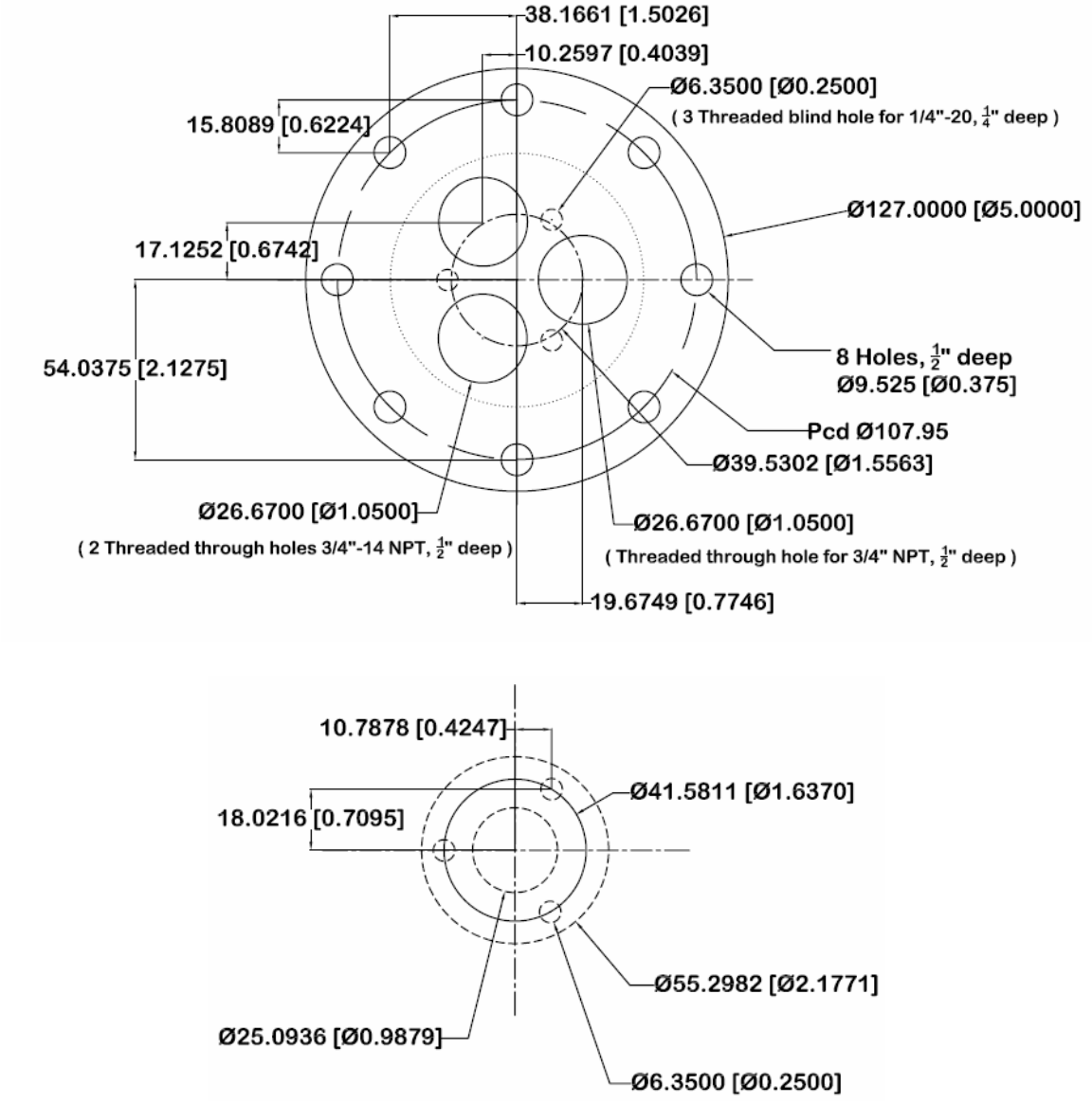

Figure 2.3 Sketch of the top flange and baffle.

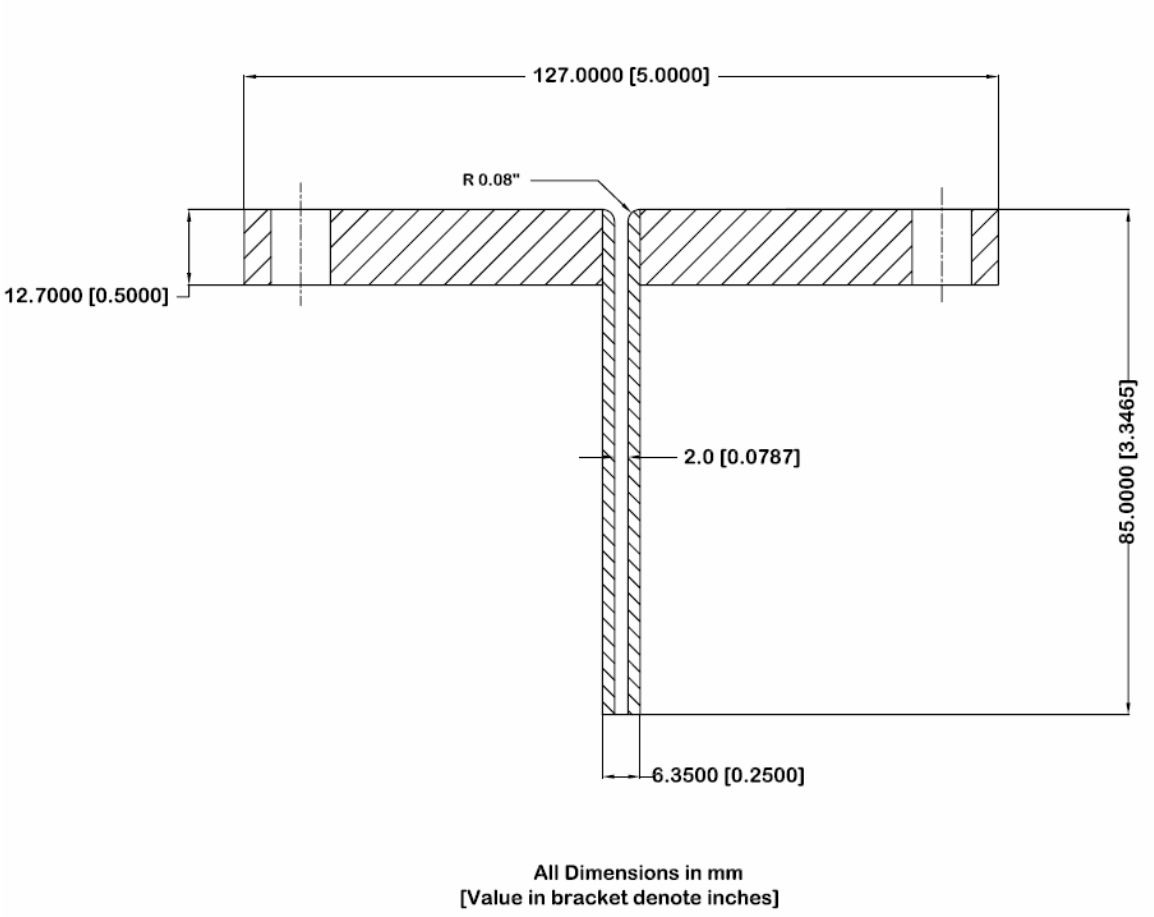

Figure 2.4 Sketch of the 2 mm nozzle.

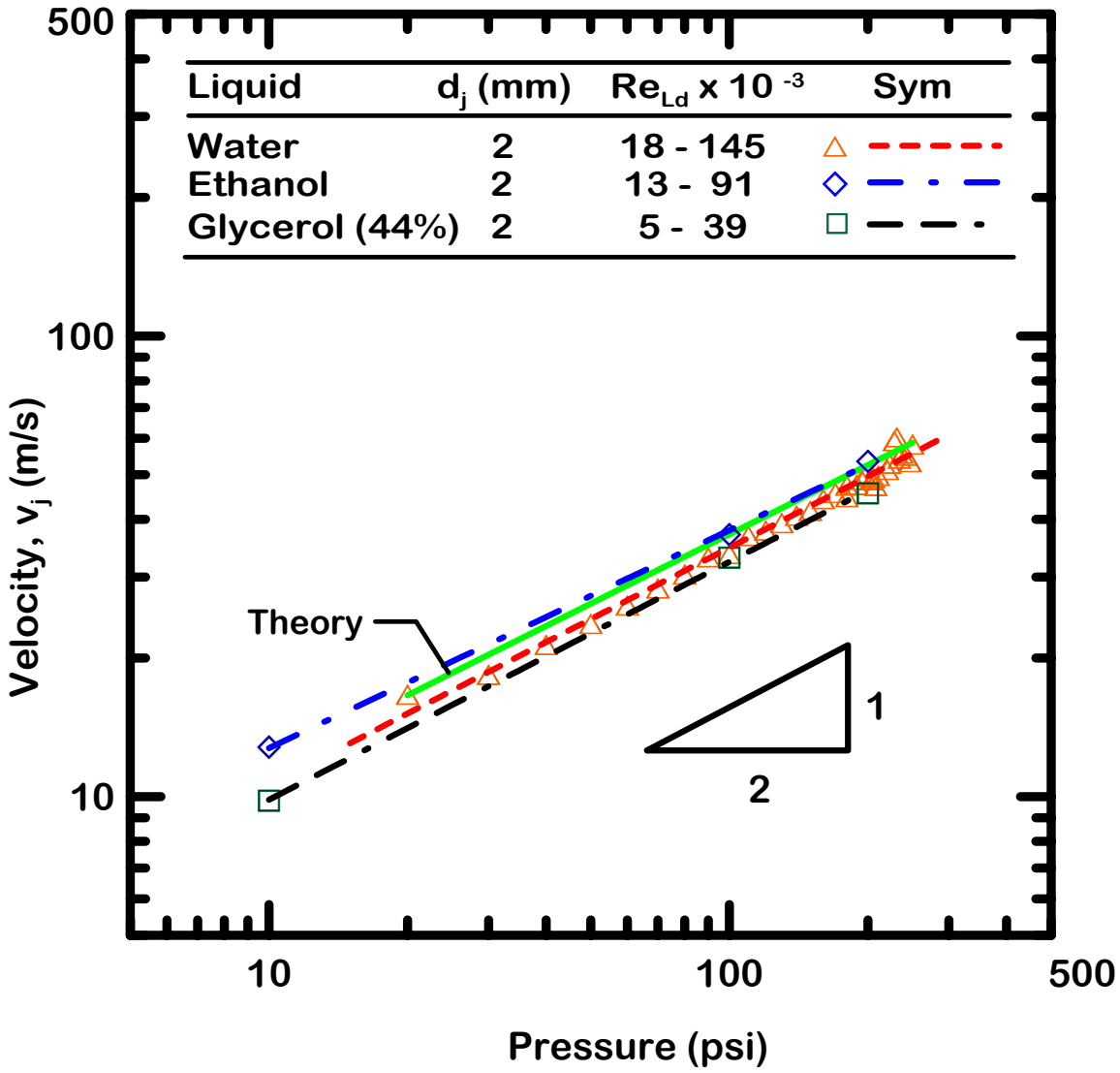

Figure 2.5 Round jet nozzle calibration. Plot showing the variation of the jet exit velocity, v_j with the corresponding injection pressure.

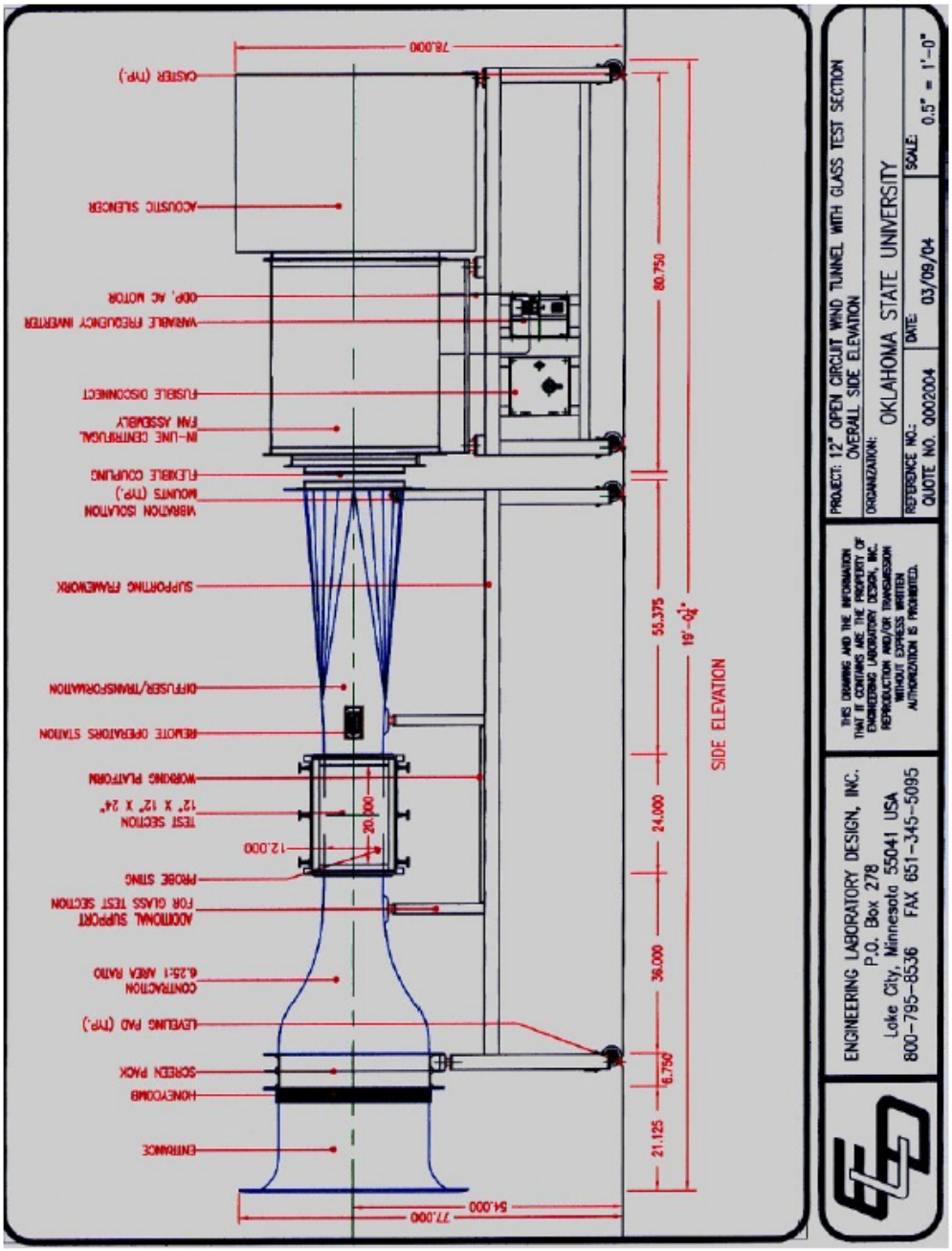

Figure 2.6 Side elevation of the subsonic wind tunnel.

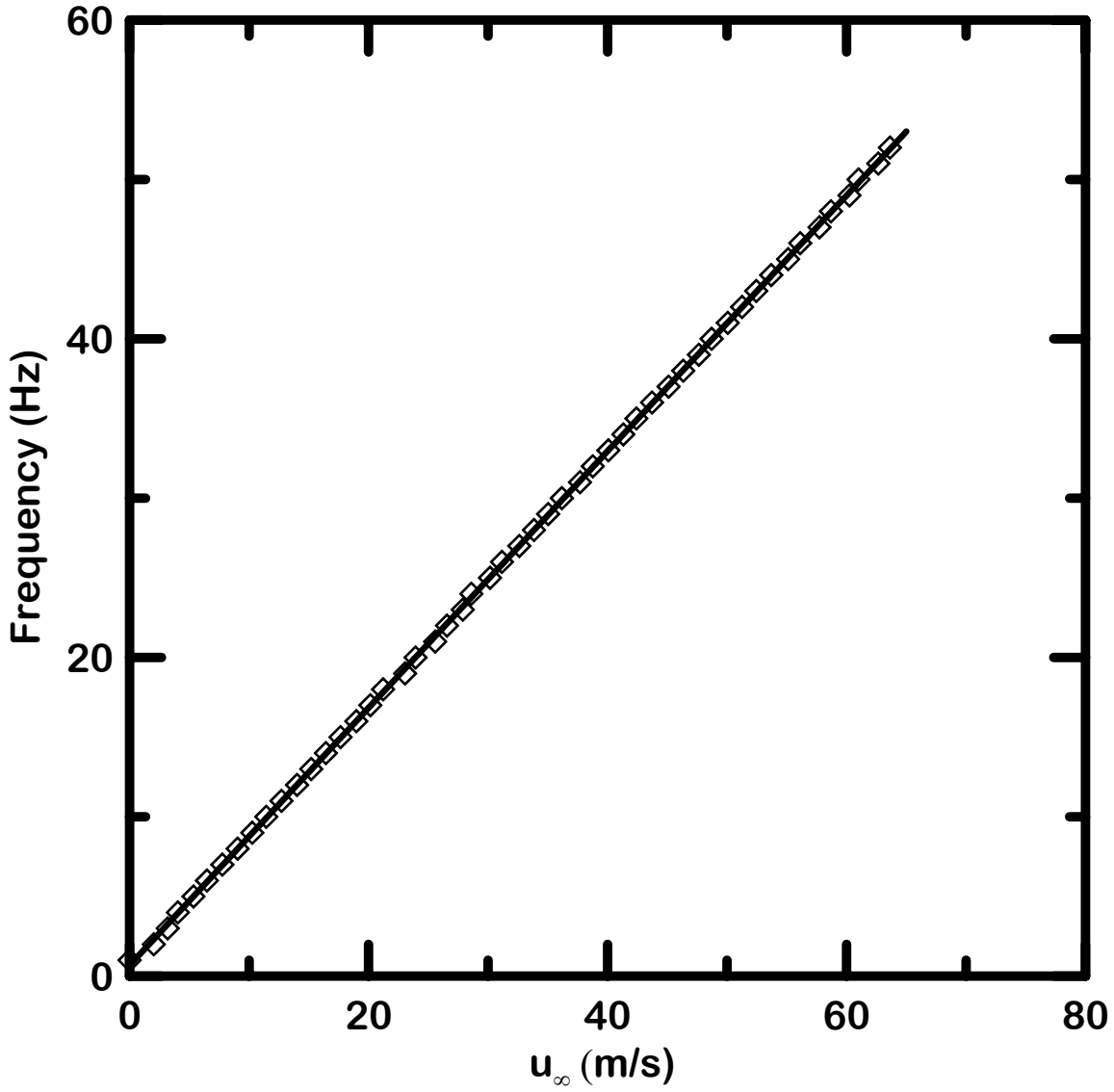

Figure 2.7 Wind Tunnel calibration. Plot showing the variation of the mean test section velocity, u_∞, with the corresponding operating frequency.

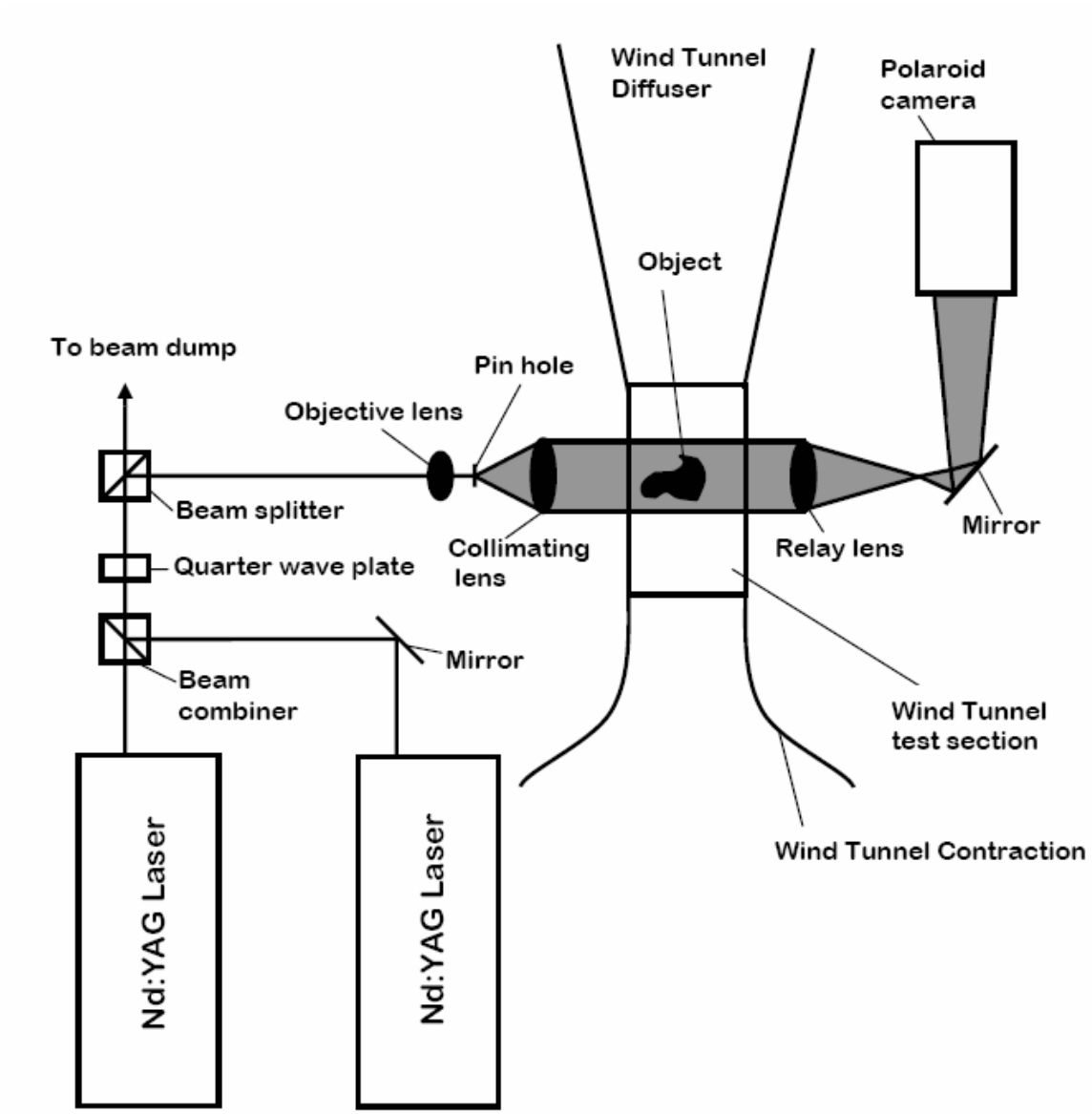

Figure 2.8 Pulsed-shadowgraphy technique arrangement.

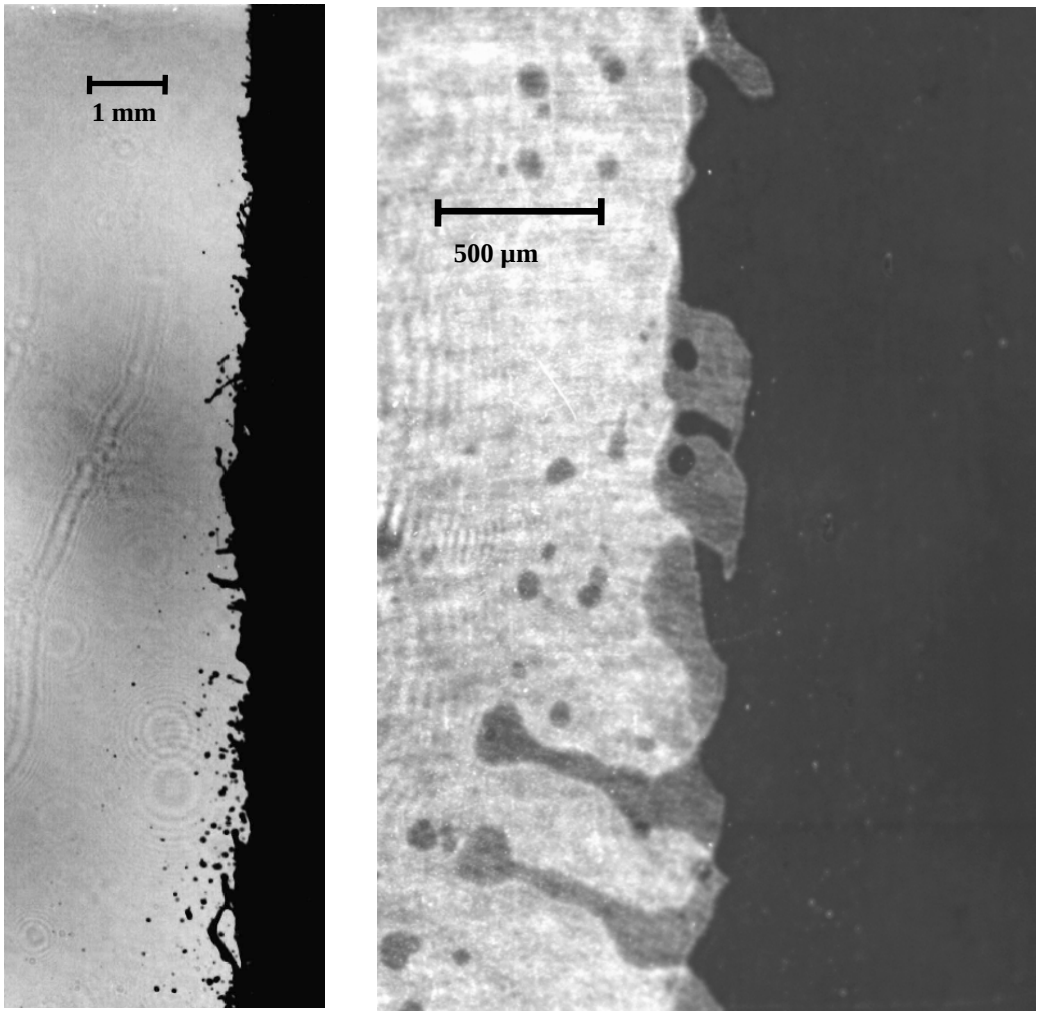

(a) (b)

Figure 2.9 (a) Single-pulse shadowgraph along the surface of a round turbulent jet. (d_j = 2.0 mm, v_j = 29.0 m/s, Re_{Ld} = 40,200, We_∞ = 0) (b) Double-pulse shadowgraph along the liquid surface of a round turbulent jet. (d_j = 2.0 mm, v_j = 29.93 m/s, Re_{Ld} = 70,400, u_∞ = 20.36 m/s, We_∞ = 15).

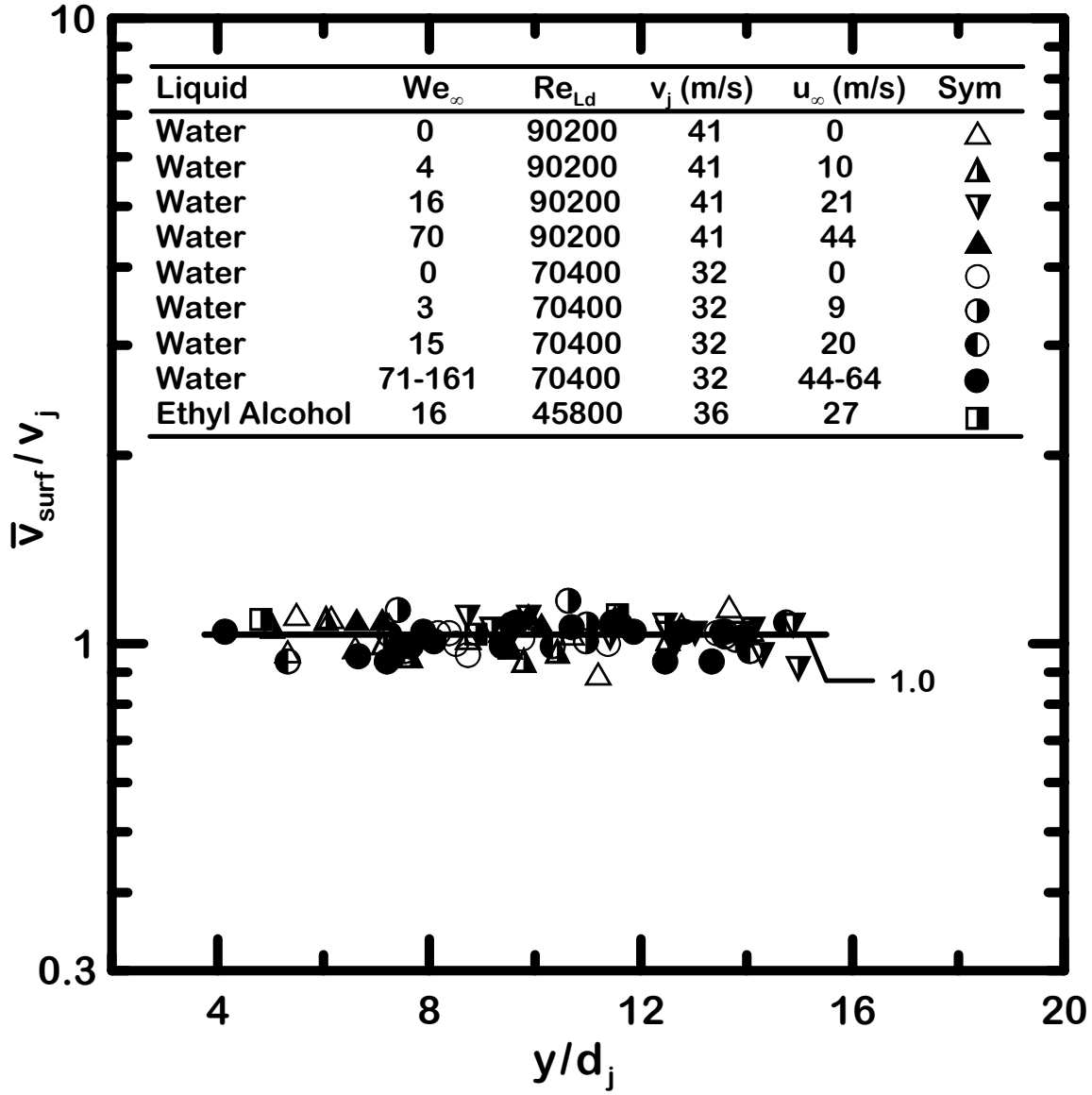

Figure 2.10 Mean liquid surface velocities as a function of streamwise distance from the jet exit.

CHAPTER III

RESULTS AND DISCUSSION

3.1 Introduction

Pulsed shadowgraphy and photography are used in this chapter to measure the surface breakup properties of round turbulent liquid jets in uniform gaseous crossflow. The properties of interest are flow visualization, breakup regime transitions, location of onset of primary breakup, drop and ligament sizes along the liquid surface, mean liquid surface velocities, liquid column trajectories and the breakup of liquid column as a whole.

3.2 Flow visualization

3.2.1 Effect of Crossflow Weber Number on Breakup Processes

A sketch showing the different breakup processes for partially turbulent round liquid jets in uniform gaseous crossflow is shown in Fig. 3.1. Visualizations of a turbulent liquid jet at various crossflow Weber number, We_∞ are illustrated in Fig. 3.2. Image (a) is a CCD camera photography and images (b) – (d) are pulsed shadowgraphy. Images (a) – (c) are for a water jet with a diameter of 2 mm and image (d) is for ethanol jet with a diameter of 2 mm. The corresponding jet velocities are 8.2 m/s and 13.9 m/s for water and ethanol respectively. The corresponding crossflow velocities for images (a) – (d) are 10.1 m/s, 21.5 m/s, 44.1 m/s and 41.3 m/s, respectively. The direction of motion

of liquid jets in all the cases is from top to bottom (the nozzle exit is visible at the top of image (a)). The crossflow direction is from left to right. The effect of gravity on present results is negligible.

Image 3.2 (a) shows a typical column breakup for a crossflow Weber number, We_∞, of 3, where the liquid jet undergoes a fracture in the liquid column without undergoing any surface breakup. This behavior is very similar to the column breakup of nonturbulent liquid jets in gaseous crossflow (Sallam et al., 2004). Image 3.2 (b) shows the bag breakup process for a crossflow Weber number of 16. During the bag breakup, nodes are formed with the spacing between them comparable to the liquid jet diameter. Between these nodes the liquid jet tends to flatten itself forming bag-like structures between the nodes. These bags grow bigger and break up into drops. This behavior is similar to the bag breakup of nonturbulent liquid jets in gaseous crossflow (Sallam et al., 2004). As the crossflow Weber number is further increased, the ligaments are stripped from the liquid jet sides as seen in image 3.2 (d). This is a typical shear breakup, occurring at a crossflow Weber number, We_∞, > 110. Intermediate to the bag and the shear breakup is the multimode breakup as shown in image 3.2 (c) that has characteristics of both bag and shear breakup processes. Multimode breakup occurs at a crossflow Weber number range of 30 – 110.

From the above description of different breakup processes, it can be concluded that partially turbulent jets in crossflow undergo similar breakup mechanisms as nonturbulent jets in crossflow.

3.2.2 Effect of Liquid Jet Reynolds Number on the Breakup Processes

The effect of liquid jet turbulence on the breakup regimes is illustrated in Fig. 3.3. The images (a) – (e) are for turbulent liquid jets at a crossflow Weber number of 16 and a jet Reynolds number of 3,420, 19,000, 40,000, 90,000 and 140,000 respectively. Test liquid in image (a) is glycerol (44 % glycerin by mass). Test liquid in images (b), (d), and (e) is water and the test liquid in image (c) is ethanol. The liquid jet velocities for images (a) – (e) are 8.2 m/s, 8.2 m/s, 29.0 m/s, 38.4 m/s and 59.5 m/s respectively. The crossflow velocities are 21.5 m/s for water, 20.9 m/s for glycerol and 13.3 m/s for ethanol.

As seen in the images (a) and (b), bags are formed at crossflow Weber number of 16 and the liquid jet Reynolds number ranges from 3420 to 19200. This is typical of partially turbulent liquid jets, that exhibit similar breakup regimes as nonturbulent liquid jets in crossflow. In images (c), (d) and (e) the liquid jet Reynolds number is increased whereas the crossflow Weber number is kept a constant. These images show no bag formation but rather the liquid jet surface becomes irregular and these irregularities increase with increasing distance from the jet exit and finally form ligaments. This is typical of turbulent primary breakup mechanism. Another difference is that in images (a) and (b), the liquid column diameter starts to decrease slightly with increasing distance from the jet exit whereas in images (c), (d), and (e) the liquid jet spreads radially causing an increase in the jet column diameter, typical of turbulent jets at high Reynolds number (Wu et al., 1992). Another important feature is that no ligaments are formed on the upwind side for the turbulent jets in images (a) and (b), unlike the turbulent liquid jets in images (c), (d) and (e). These features are attributed to the interaction of the turbulent eddies within the free surface of the liquid jet. At high liquid jet Reynolds numbers, these

turbulent eddies would have enough kinetic energy to cause surface breakup not only at the downwind side, but also at the upwind side, despite the presence of the gaseous crossflow. In the following section, the liquid jet breakup mechanism will be classified based on the presence of surface breakup at the upwind side.

3.3 Primary Breakup Regimes

It is shown that turbulent liquid jets in crossflow undergo upwind surface breakup (refer to Fig. 3.3), when the energy of the turbulent eddies in the liquid jet is large enough to overcome the liquid surface tension forces. The eddies form protrusions on the liquid surface, which are seen as ligaments. This breakup regime will be termed as turbulent breakup. An increase in the crossflow velocity, however, expressed as a decrease in the liquid/gas momentum ratio, would suppress the upwind surface breakup. This occurs because the energy of turbulent eddies in the liquid jet is not large enough to overcome the combination of liquid surface tension forces and the pressure forces exerted by the gaseous crossflow. This type of breakup, where drops are formed only on the downwind side will be termed as aerodynamic breakup. The breakup regime map for turbulent jets in crossflow is shown in Fig. 3.4. In this map, liquid jet Weber number, $We_{L\Lambda}$ is plotted on the x-axis and the dimensionless quantity $We_{L\Lambda}q^{1/3}$ is plotted on the y-axis.

For a fixed $We_{L\Lambda}$, the momentum ratio q controls the breakup regime transition from an aerodynamic breakup to a turbulent breakup. At lower values of q, the crossflow velocity is high and so even when the turbulence in the liquid jet is high, the high crossflow velocity would suppress the formation of ligaments on the upwind side. The upwind surface, however, will be deformed due to column and surface waves associated

with column, bag, multimode or shear breakup similar to the breakup of nonturbulent liquid jets in crossflow. These types of breakup are termed collectively as aerodynamic breakup on the present breakup regime map. As q is increased, the crossflow velocity decreases, and the turbulence in the liquid jet dominates the surface breakup on the upwind side forming ligaments.

The correlation that best describes the transition from aerodynamic breakup to turbulent breakup is as follows:

$$We_{L\Lambda}q^{1/3}= 17{,}000 \tag{3.1}$$

Also shown in Fig. 3.4, is the correlation by Wu and Faeth, 1995, for turbulent jet in still gases. Present results for breakup regime transition of turbulent liquid jets in crossflow at large liquid/gas momentum ratios agree well with the results of Wu & Faeth, (1995) for the surface breakup of turbulent jets in still gases.

The breakup regime map where $We_{L\Lambda}q^{1/3}$ on the y-axis is plotted against the liquid jet Reynolds number, Re_{Ld} on the x-axis is shown in Fig. 3.5. It is observed that both turbulent and aerodynamic breakup occurs for the range of Reynolds numbers, Re_{Ld} = 6,000 – 60,000, with the transition controlled mainly by $We_{L\Lambda}q^{1/3}$.

3.4 Onset of Breakup

The properties at the onset of primary breakup for turbulent liquid jets in gaseous crossflow were analyzed in the same manner as earlier studies of nonturbulent liquid jets in crossflow (Sallam et al., 2004). Onset of breakup refers to the first appearance of ligaments along the streamwise distance from the jet exit. The properties of interest are:

time of the onset of breakup, locations of the onset of breakup, and ligaments and drop sizes at the onset. These will be described in detail in the following sections.

3.4.1 Time of Onset of Breakup – Multimode and Shear Breakup Regime

The time of the onset of breakup refers to the time taken for the first ligament to appear along the liquid surface. Within the shear and multimode breakup regimes, the appearance of drops was always preceded by the appearance of ligaments protruding downstream from the region near the sides of the liquid jet toward the wake of the jet. Analogous to earlier findings for the onset of ligament and drop formation during turbulent primary breakup of round liquid jets in still gases (Sallam et al., 2002), ligament diameters at the onset of ligament formation were found by equating the momentum (relative to bulk liquid in the jet) of a ligament of given size, d_l, to the maximum surface tension force required to form a drop of the same size. Treatment of the momentum of the present liquid jet in crossflow, however, had to be modified from its treatment for a turbulent liquid in still gases (Sallam et al., 2002). In the present case, it was assumed that liquid motion required to form a ligament originated from the viscous shear layer growing at the periphery of the liquid jet due to the motion of the gaseous crossflow. This approach was similar to the approach taken for the nonturbulent liquid jets in crossflow (Sallam et al., 2004). The characteristic liquid phase velocity of this shear layer, due to viscous effects, is:

$$u_L \sim u_\infty/[1+(\mu_L\rho_L/(\mu_\infty\rho_\infty))^{1/2}] \qquad (3.2)$$

Equating the momentum of the liquid shear layer near the surface, to the surface tension force required by the hemispherical distortion of the liquid surface that must be overcome to form a ligament having a diameter, d_l, there results:

$$\rho_L u_L^2 d_l^2 \sim \sigma\, d_l \tag{3.3}$$

Combining Eqns. (3.2) and (3.3) and substituting for u_L^2 and noting that $\rho_\infty/\rho_L << \mu_L/\mu_\infty$, there results:

$$d_l/d_j = C\,(\mu_L/\mu_\infty)/We_\infty \tag{3.4}$$

where C is an empirical constant on the order of unity. Sallam et al. (2004) reported the following for nonturbulent liquid jet in uniform crossflow:

$$d_l/d_j = 0.07\,[(\mu_L/\mu_\infty)/We_\infty]^{1/2} \tag{3.5}$$

The reduction of the power in Eqn. (3.4) from 1 to 1/2 in Eqn. (3.5) is statistically significant. This discrepancy appears to be due to the limitations that the finite diameter of the liquid layer places on the growth of the shear layer, noting that the shear layer is eventually limited to a fixed fraction of the liquid jet diameter at conditions where this power must become zero.

Motion along the liquid jet is given as a function of time by the liquid jet convection velocity, based on present observations:

$$y = v_j\, t \tag{3.6}$$

then the diameter of the ligament at onset should be proportional to the thickness of the liquid shear layer, which is assumed to grow according to the well known viscous shear layer growth rate (Schlichting H., 1960) expression $(\nu_L t)^{1/2}$. This implies that

$$d_l \sim (\nu_L t_i)^{1/2} \tag{3.7}$$

Substituting for d_l from Eqn. (3.4) and rearranging then yields:

$$t_i / t_\nu^* = C_t C^2 (\mu_L/\mu_\infty)/We_\infty \tag{3.8}$$

where

$$t_\nu^* = d_j^2/\nu_L \tag{3.9}$$

and C_t is an empirical constant on the order of unity.

Values of t_i were found from present measurements of y_i using Eqn. (3.8). These measurements were plotted as a function of $(\mu_L/\mu_\infty)/We_\infty$, as suggested by Eqn. (3.8) in Fig. 3.6. The plot also shows the results for nonturbulent liquid jets in uniform crossflow (Sallam et al., 2004). For present measurements, low liquid jet Reynolds number ($Re_{Ld} <$ 20,000) correlate quite well according to the relationship of Eqn. (3.8) as follows:

$$t_i / t_\nu^* = 0.0004 [(\mu_L/\mu_\infty)/We_\infty] \tag{3.10}$$

The average uncertainty of the present measurements for the time of onset of breakup is 56% with respect to the mean measured value at 95% confidence level. This value is dominated by sampling limitations.

The time for the onset of breakup becomes independent of the crossflow at higher liquid jet Reynolds number suggesting that the turbulence in the jet dominates the surface breakup. For Re_{Ld} > 40,000 the onset of breakup data correlate well with those of turbulent round liquid jet in still air by Wu et al. (1992) suggesting weak aerodynamic effects.

The time of onset of breakup for turbulent liquid jets in uniform gaseous crossflow as a function of the dimensionless parameter $We_{L\Lambda}q^{1/3}$ is illustrated in Fig. 3.7. This dimensionless parameter was used to define the two breakup regimes namely the aerodynamic breakup regime and the turbulent breakup regime. From Fig. 3.7, the time of onset of ligament formation for turbulent liquid jets exhibiting aerodynamic breakup follows a correlation given by:

$$t_i / t_v^* = 1.09 \, (We_{L\Lambda}q^{1/3})^{2.1} \quad ; We_{L\Lambda}q^{1/3} < 17{,}000 \qquad (3.11)$$

For turbulent liquid jets exhibiting turbulent breakup, time of the onset of ligament formation is a constant value suggesting that turbulence in liquid jet dominates the surface breakup. Moreover, as the liquid jet Reynolds number increases from 40,000 to 140,000, the time of onset of breakup, t_i / t_v^*, decreases from approximately 4×10^{-5} to 4×10^{-6}. This shows that higher liquid jet Reynolds number causes faster development of surface irregularities and therefore quicker onset of ligaments.

Also included in the plot is the correlation, fitted to the transitional range at $We_{L\Lambda}q^{1/3}$ = 17,000. This agrees with the earlier results developed for classification of breakup regimes into aerodynamic breakup and turbulent breakup.

3.4.2 Time of Onset of Breakup – Bag Breakup Regime

Turbulent liquid jets with low Reynolds numbers exhibit bag breakup similar to nonturbulent liquid jets in crossflow. As mentioned earlier the mechanism of formation of bags for turbulent liquid jets is similar to that of nonturbulent liquid jets. But unlike the bags formed from nonturbulent jets, the bags of turbulent jets are formed with ligaments and drops appearing on the upwind side of the liquid jet. A series of images showing the illustrating bag formation, bag breakup, the ligament formation on upwind side and the drop pinching off from the ligament on upwind side are shown in Fig. 3.8. The test conditions included a water liquid jet with Reynolds number of Re_{Ld} = 19,200, a crossflow Weber number of We_{∞} = 10, and a liquid jet diameter of d_j = 2.0 mm.

Time of onset of bag formation, t_{bi}, as a function of crossflow Weber number is shown in Fig. 3.9. The plot also includes the data for the time of onset of breakup for nonturbulent liquid jets in crossflow (Sallam et al., 2004). It is seen that the time taken for the onset of bag formation, t_{bi} follows the same correlation as Eqn. (3.11) for turbulent liquid jets with low Reynolds number Re_{Ld} < 20,000. Bags were also observed at a liquid jet Reynolds number of 40,000.

The average uncertainties of the present measurements for the time of onset of bag formation is 58% with respect to the mean measured value at 95% confidence level. The high value of uncertainty is dominated by sampling limitations.

3.4.3 Location of Onset of Breakup

To determine the streamwise locations for the onset of breakup for turbulent jets in crossflow, the breakup time was converted into the location of onset of breakup based

on the assumption that ligaments are convected along the liquid surface with the velocity of liquid jet. For the present investigation, phenomenological analyses developed by Aalburg et al. (2005) were employed, that was originally based on the idea developed by Wu and Faeth, (1993). Based on this theory the location of the onset of turbulent primary breakup along the liquid surface is given by:

$$(y_i/\Lambda)[1+C_p(y_i/\Lambda)^{-4/9}We_{L\Lambda}^{2/9}(\rho_\infty/\rho_L)(u_\infty/v_j')^2]^{9/10} = C_{xi}\, We_{L\Lambda}^{-n} \qquad (3.12)$$

where, n = 4/10.

The plot for the streamwise location of onset of breakup as a function of the liquid jet Weber number, $We_{L\Lambda}$ is shown in Fig. 3.10. In completing this plot, the values, C_p = 0.3, C_{xi} = 26,190 and n = 0.85 are selected as the best fit values. Also in this plot the ratio of v_j'/v_j = 0.03 was used for fully developed turbulent pipe flow (Hinze, 1959). The best fit correlation for the present results is given as follows:

$$(y_i/\Lambda)[1+0.3(y_i/\Lambda)^{-4/9}We_{L\Lambda}^{2/9}(\rho_\infty/\rho_L)(u_\infty/v_j')^2]^{9/10} = 26{,}190\, We_{L\Lambda}^{-0.85} \qquad (3.13)$$

The average uncertainties of the present measurements for the location of onset of breakup is found to be 54% with respect to the mean measured value at 95% confidence level. This is dominated by sampling limitations.

Also shown in the plot are the results for Aalburg et al. (2005). It can be concluded that present correlation for turbulent jets in still air and crossflow are in good agreement with the results for Aalburg et al. (2005).

3.4.4 Ligament and Drop Sizes at the Onset of Breakup

Similar to past investigations of round and annular turbulent jets in still air (Sallam and Faeth, 2003), present investigation showed two types of ligament breakup mechanisms. The ligaments can undergo breakup forming drops by either tip breakup process where the ligaments themselves act as liquid jets in the Rayleigh breakup regime and form drops of comparable size, or by ligament base breakup where the whole ligament pinches off from the liquid surface and undergo a secondary breakup forming drops. A typical ligament tip breakup and a ligament base breakup is shown in Figs. 3.11 (a) and (b) respectively. Ligament base breakup was rare, however, and the phenomenological analyses for drop and ligament sizes will be based on the ligament tip breakup mechanism process.

The diameter of ligaments at the onset is given as follows (refer Eqn. (3.5)):

$$d_{li}/d_j = C_l \left[(\mu_L/\mu_\infty)/We_\infty\right]^{1/2} \tag{3.14}$$

where C_l is an empirical constant of the order of unity. For Rayleigh type breakup mechanism, the drop to ligament diameter ratio should be a constant value equal to 1.91 as proposed by Tyler in 1933. (see Teng et al., (1995) and references cited). Therefore the ratio of drop diameter to ligament diameter at onset is given as follows:

$$d_{pi}/d_{li} = C_i \tag{3.15}$$

where C_i is an empirical constant associated with the onset of drop formation.

Drop diameters and the ligament diameters at onset at the downwind side of the turbulent liquid jets is plotted in Fig. 3.12 as suggested by Eqns. (3.14) and (3.15). The

plot also includes the results for the nonturbulent liquid jets in crossflow (Sallam et al., 2004).

Downwind ligament diameters for the turbulent jet at onset are similar to those of nonturbulent liquid jets within experimental uncertainty. Drop diameters at onset for turbulent jets is lower than those for nonturbulent jets (Sallam et al., 2004). This is not surprising, however, because the presence of turbulent eddies in the liquid phase accelerate the onset of breakup, resulting in smaller drops from the same ligament sizes.

For the present measurements, the best fit correlation for the downwind drop sizes at onset is given as follows:

$$d_{pi}/d_{li} = 0.8 \tag{3.16}$$

The average uncertainty for the present measurements for the drop diameters and ligament diameters at onset on the downwind side was found to be 30% and 32% with respect to the mean measured values at 95% confidence level, dominated by sampling limitations.

An important result for the drop diameters and the ligament diameters at the onset of turbulent liquid jets is that, drops and ligaments exist even on the upwind side of the liquid jet for $We_{L\Lambda}q^{1/3} > 17{,}000$, unlike the case of nonturbulent liquid jets. The existence of drops and ligaments on the upwind side of the liquid jet confirms that turbulent primary breakup is the dominating mechanism and the effect of crossflow is negligible within the turbulent breakup regime ($We_{L\Lambda}q^{1/3} > 17{,}000$) of turbulent round liquid jets in gaseous crossflow.

The drop diameters and ligament diameters at onset at the upwind side is plotted in Fig. 3.13. The best fit correlation for the drop diameters and the ligament diameters are given as follows:

$$d_{pi}/d_{li} = 1.00 \tag{3.17}$$

$$d_{li}/d_j = 0.07 \tag{3.18}$$

The average uncertainty for the present measurements for the drop diameters and ligament diameters at onset on the upwind side was found to be 32% and 20% with respect to the mean measured values at 95% confidence level.

Drop sizes at onset for turbulent liquid jets in crossflow were compared with those of turbulent liquid jets in still gases in Fig. 3.14. Sallam and Faeth (2003) correlated the drop sizes at onset for turbulent round liquid jets by equating the kinetic energy of a characteristic eddy to the surface energy required to form a droplet of a corresponding size. Using the relationship between the eddy size and its velocity in the inertial range (Tennekes and Lumley, 1972), and associating the SMD resulting from the turbulent primary breakup with the characteristic eddy size the following expression for SMD at the onset was developed:

$$\frac{SMD_i}{\Lambda} = C_i \left(\frac{v_j}{\bar{v}'} \right)^{6/5} We_{L\Lambda}^{-3/5} \tag{3.19}$$

where, $\bar{v}'$ is the average cross stream velocity fluctuation at the jet exit, and C_i is an empirical constant on the order of unity. Using the fact that $\bar{v}' / v_j$ is a constant for fully developed turbulent pipe flow, SMD_i/Λ must be only a function of $We_{L\Lambda}$. Past work of

Wu et al. (1992), Wu and Faeth (1993, 1995), have shown good agreement between the universal root normal distribution function of Simmons (1977) and measured drop size distribution functions for a variety of primary breakup processes. The universal root normal distribution function is defined by MMD/SMD = 1.2, where MMD is the mass median drop diameter of the spray and SMD is the Sauter mean diameter of the spray, defined as the diameter of a drop having the same surface area/volume ratio as the spray as a whole. Therefore knowing one of these two parameters completely describes the drop size distributions.

Present measurements of SMD_i are plotted as suggested by Eqn. (3.19) in Fig. 3.14. As expected from the previous results plotted in Figs. 3.12 and 3.13, the SMD_i is a constant and is independent of the liquid jet Weber number unlike turbulent jets in still gases. The best-fit correlation for the current measurements for still air and in crossflow is given as follows:

$$\frac{SMD_i}{\Lambda} = 0.36 \tag{3.20}$$

The average uncertainty for the present measurements for the SMD at the onset was found to be 40% with respect to the mean measured value at 95% confidence level. The reason for the difference between the results of turbulent jets in crossflow and in still gases is an indication of the effect of the crossflow .

3.5 Drop Sizes along the Liquid Surface

Expressions for variation of SMD along the streamwise distance from the jet exit were developed using similar theories used for round turbulent liquid jets in still gases by

Wu et al. (1992). It was assumed that SMD was dominated by the largest drop that can be formed at a particular location and that the turbulent eddies in the jet will form drops of the same size as these eddies. An expression for variation of SMD with streamwise distance from the jet exit was developed (Wu et al., 1992) as follows:

$$\frac{SMD}{\Lambda} = C_y \left(\frac{y}{\Lambda We_{L\Lambda}^{1/2}} \right)^{2/3} \tag{3.21}$$

where C_y is a constant on the order of unity. Present measurements of SMD are plotted as suggested by Eqn. (3.19) in Fig. 3.15. Also shown in the plot are the correlation by Aalburg et al. (2005) for fully developed turbulent jets in crossflow and the correlation for turbulent jets in still air by Wu et al. (1995) for round jets. The best-fit correlation of the present measurements for turbulent liquid jets in crossflow is as follows:

$$\frac{SMD}{\Lambda} = 0.45 \left(\frac{y}{\Lambda We_{L\Lambda}^{1/2}} \right)^{0.32} \tag{3.22}$$

The power for the normalized streamwise distance is not equal to 0.67, as predicted by theory for turbulent jets in still air. This behavior indicates the effect of the crossflow.

3.6 Liquid Core Breakup

Liquid core breakup is important because it defines the start of fully dispersed multiphase flow region. For the current experimental investigations, locations of completion of the primary breakup processes for column, bag multimode and shear breakup regimes were analyzed similar to earlier treatment for nonturbulent liquid jets in crossflow by Wu et al. 1997. Using this approach, the time required for the breakup, t_b, is

given similar to the secondary breakup of drops subjected to shockwave disturbances by Hsiang and Faeth, 1995:

$$t_b/t^* = C_{yb} \tag{3.23}$$

where, t* is the characteristic liquid phase time from Ranger and Nicholls (1969) and is given by:

$$t^* = (\rho_L/\rho_\infty)^{1/2} dj/u_\infty \tag{3.24}$$

and C_{yb} is an empirical constant associated with the time of breakup of liquid column on the order of unity. Since the liquid jet moves with a velocity v_j in the streamwise direction, the expression for t_b becomes:

$$t_b = y_b/v_j \tag{3.25}$$

Substituting for t_b and t* into Eqn. (3.23) the streamwise location for the end of liquid column is given by:

$$y_b/d_j \sim [\rho_L v_j^2/(\rho_\infty u_\infty^2)]^{1/2} \sim q^{1/2} \tag{3.26}$$

Finally, considering the conservation of cross stream momentum, the cross stream location for the end of liquid column is given by (Wu et al., 1997):

$$x_b/d_j = C_{xb} \tag{3.27}$$

where, C_{xb} is an empirical constant associated with the cross stream penetration of liquid column on the order of unity.

Photographs of the location of liquid core breakup for column and bag breakup regimes are shown in Fig. 3.16. The liquid jet is injected vertically downward and the crossflow is from left to right in images (a) and (b).

Measurements of t_b and x_b for the present investigation of turbulent jets in crossflow for column, bag, multimode and shear breakup regime, (i.e. within aerodynamic breakup regime) as a function of the crossflow Weber number is shown in Fig. 3.17. Also shown in Fig. 3.17 are the results for the nonturbulent liquid jets (Sallam et al., 2004). The crossflow Weber number for breakup regime transitions are also plotted as dashed lines. The value of t_b/t^* for the present investigations correlate well with the previous results for nonturbulent jets in crossflow and yield a value of C_{yb} equal to 2.5. The average uncertainty for the present measurements for time of breakup of liquid core was found to be 9% with respect to the mean measured value at 95% confidence level.

The results for x_b/d_j for the present measurements agree well with the correlation for nonturbulent liquid jets in crossflow (Wu et al., 1997 and Sallam et al., 2004), and yield a of C_{xb} equal to 8. The average uncertainty for the present measurements for cross stream location of breakup of liquid core was found to be 20% with respect to the mean measured value at 95% confidence level. From the above results, it can be concluded that for turbulent and nonturbulent liquid jets in uniform crossflow, the time for the end of liquid core in streamwise direction and the location of the end of liquid core in cross stream directions remains the same.

3.7 Liquid Column Trajectories

Liquid column trajectories are important in consideration of modeling sprays and atomization processes because drops formed at the liquid jet surface emerge from locations in the x, y plane. Study of liquid column trajectories gives information about the amount of liquid jet penetration and defines the location of dispersion of drops formed due to atomization.

For present investigations, simplified analyses following Wu et al. (1997) were used for bag, multimode and shear breakup regimes (i.e. aerodynamic breakup regimes). Liquid column trajectories were analyzed by balancing liquid acceleration with the aerodynamic drag forces in the air crossflow direction. The change in the liquid velocities in the streamwise direction was due to aerodynamic drag forces. For modeling, the liquid column was assumed to be a cylindrical liquid element with a constant diameter equal to the liquid jet exit diameter d_j and having a length ℓ. Assumptions made during this derivation included neglecting the mass losses caused by the evaporation and droplet removal along the liquid column. The force diagram for the liquid jet in crossflow is shown in Fig. 3.18. The origin of the x and y co-ordinates was defined as the centre of the nozzle exit with the x direction pointing in the air cross stream direction and y direction pointing in the jet streamwise direction. The gravity force was small in comparison with the aerodynamic forces. It was also assumed that the transverse velocity of liquid jet remains a constant up to the column fracture location. Wu et al. (1997) introduced an average drag coefficient C_d and the x-momentum equation was given by:

$$\frac{\rho_L \pi d_j^{\,2} \ell}{4} \frac{du_L}{dt} = 0.5 C_d \rho_g (u_g - u_L)[(u_g - u_L)^2 + (v_g - v_L)^2]^{1/2} \ell d_j \qquad (3.28)$$

where, u and v are the velocities in the x and the y directions respectively and the subscripts L and g denote liquid and the gas phase.

The average drag co-efficient, C_d included the effects of liquid column deformation, flattening, droplet stripping and disintegration. Using the x-momentum equation, the fluid velocity in the cross stream direction was given by:

$$u_L = (2C_d/\pi)\ [(\rho_\infty u_\infty^2)/(\rho_L d_j)]t \tag{3.29}$$

The axial location of the liquid column was found out from Eqn. (3.30) using $u_L = dx/dt$ and yielded:

$$x = (2C_d/\pi)\ [(\rho_\infty u_\infty^2)/(\rho_L d_j)]t^2 \tag{3.30}$$

Since the transverse velocity of the liquid jet was assumed to be a constant and equal to the value of injection velocity v_j, the trajectory was obtained from Eqn. (3.31) (using $y = v_j t$):

$$y/d_j q = \sqrt{(\pi/C_d)}(x/d_j q) \tag{3.31}$$

The present results for the liquid column trajectories are shown in Fig. 3.19. The y location of the liquid column trajectory is plotted against the x location of the liquid column trajectory. The average uncertainty for the present measurements for liquid column trajectories was found to be 26% with respect to the mean measured value at 95% confidence level. The plot shows the data for the shear, multimode and bag breakup. A best fit correlation yielded the value of drag coefficient C_d to be 1.56, 1.95, and 2.51 for shear, multimode and bag breakup, respectively. Recalling the fact that C_d accounts for

the deformation of the liquid jet column, present values of the drag coefficient lie in between the corresponding values for a solid cylinder and a flat plate.

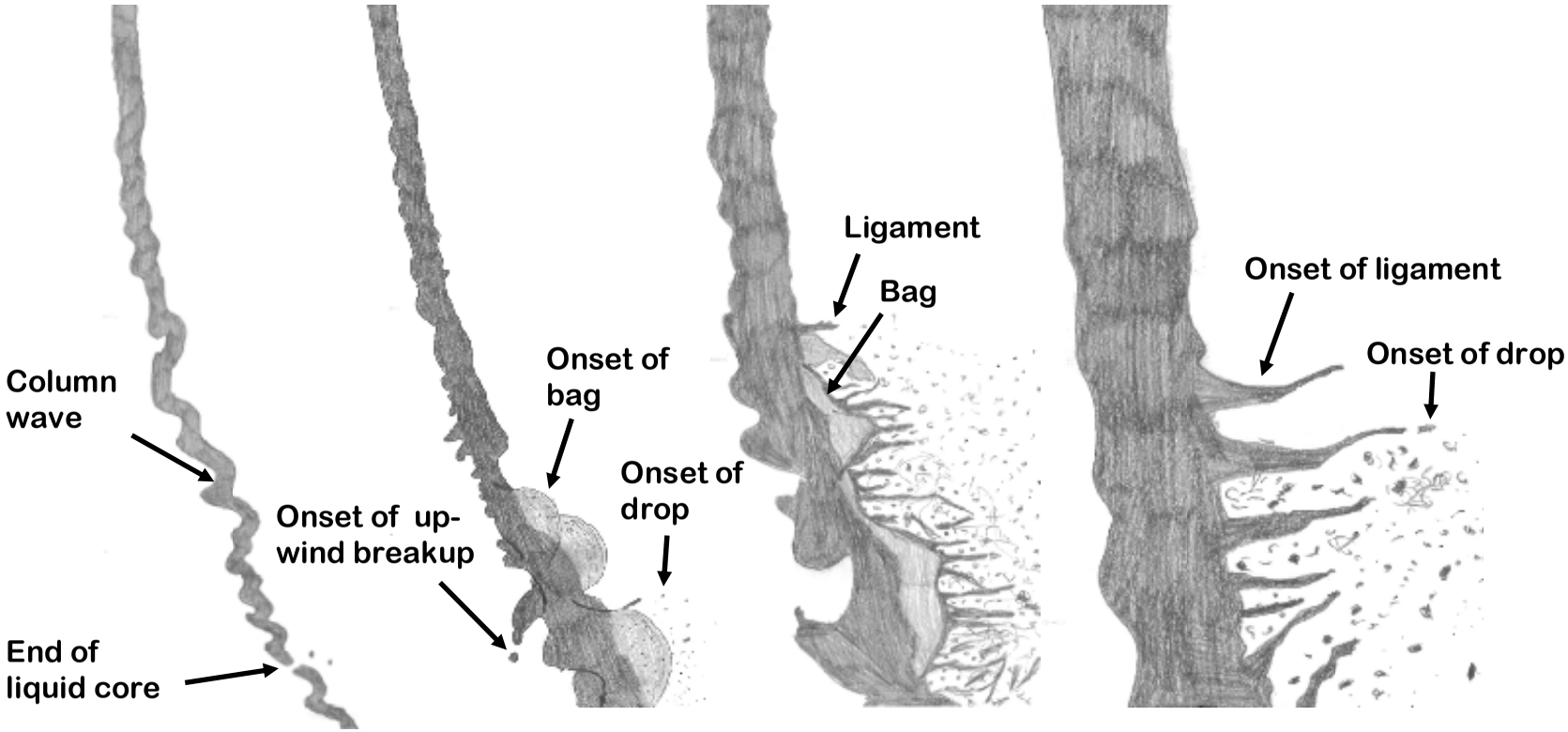

(a) Column breakup (b) Bag breakup (c) Multimode breakup (d) Shear breakup

Figure 3.1 Sketch showing different breakup mechanisms.

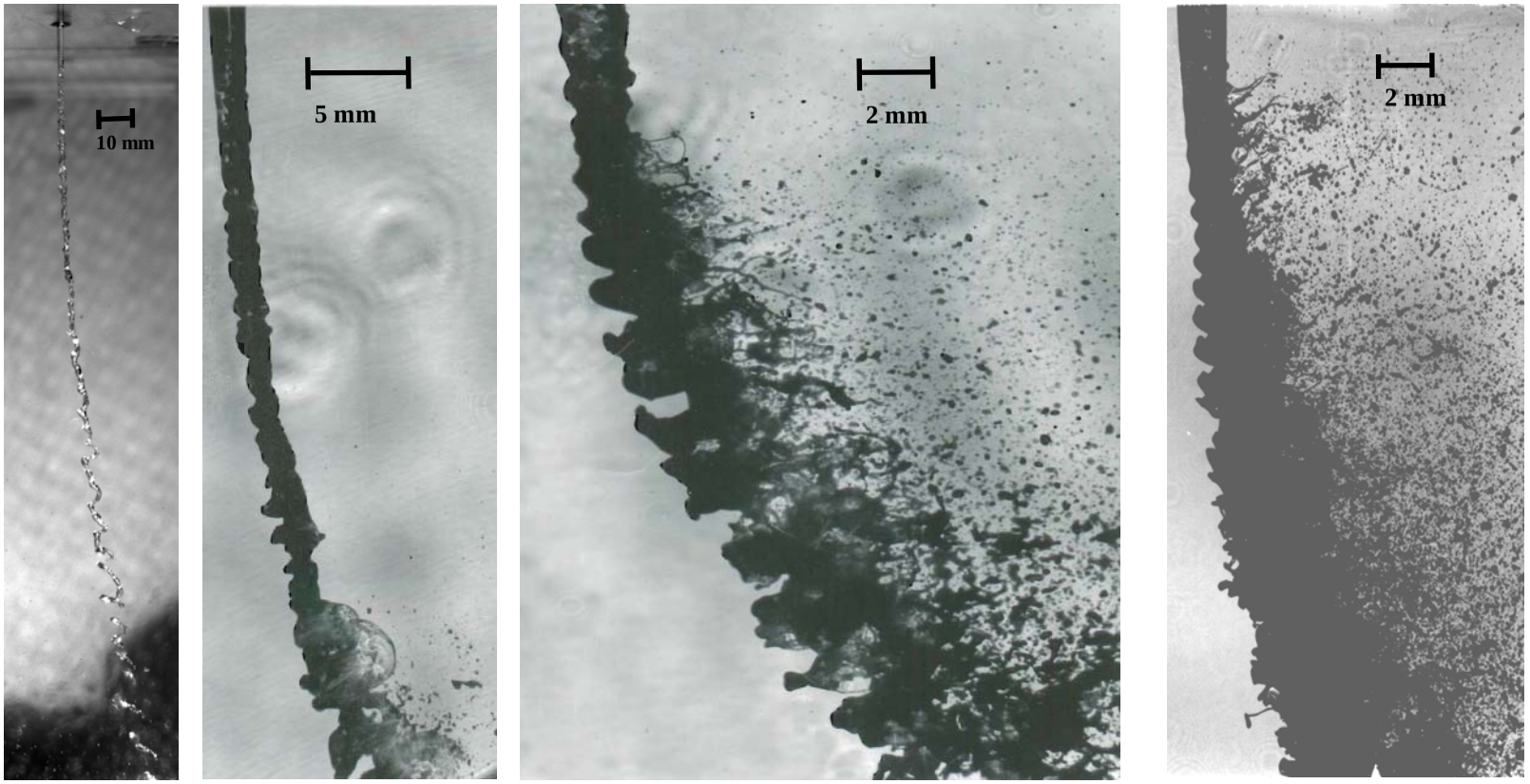

(a) Column breakup (b) Bag breakup (c) Multimode breakup (d) Shear breakup

Figure 3.2 Flow visualizations showing different breakup regimes. Re_{Ld} = 19,000, d_j = 2.0 mm. (a) Water, v_j = 8.2 m/s, u_∞ = 10.1 m/s, We_∞ = 3, (b) Water, v_j = 8.2 m/s, u_∞ = 21.5 m/s, We_∞ = 16, (c) Water, v_j = 8.2 m/s, u_∞ = 44.1 m/s, We_∞ = 70, (d) Ethanol, v_j = 13.9 m/s, u_∞ = 41.3 m/s, We_∞ = 161. The crossflow is from left to right in all images.

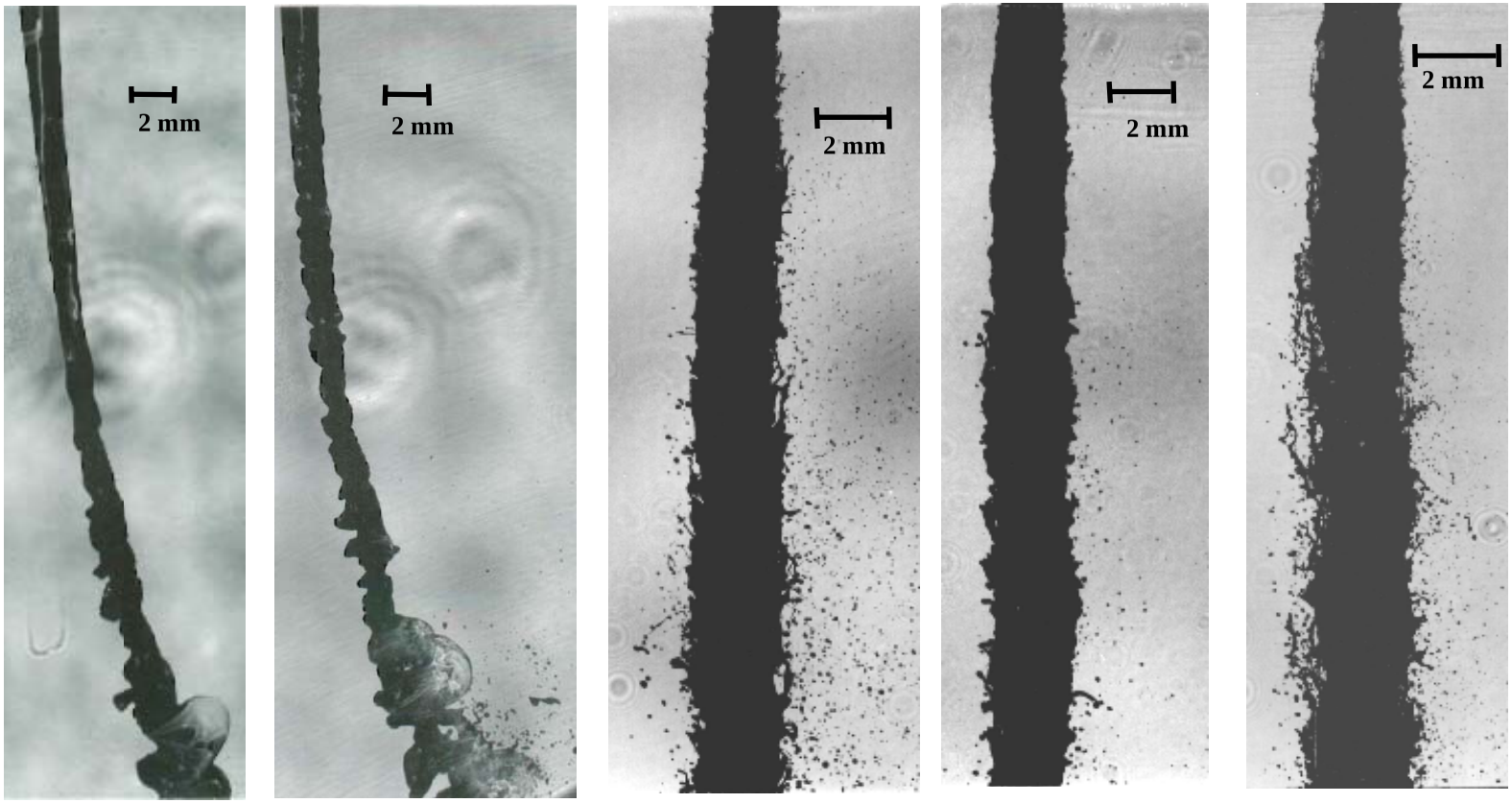

(a) Bag breakup (b) Bag breakup (c) Turbulent breakup (d) Turbulent breakup (e) Turbulent breakup

Figure 3.3 Flow visualizations showing effect of Reynolds number on bag breakup regimes. We_∞ = 16, d_j = 2.0 mm. (a) Glycerol, Re_{Ld} = 3,420, v_j = 8.2 m/s, u_∞ = 20.9 m/s, (b) Water, Re_{Ld} = 19,000, v_j = 8.2 m/s, u_∞ = 21.5 m/s (c) Ethanol, Re_{Ld} = 40,000, v_j = 29.0 m/s, u_∞ = 13.3 m/s (d) Water, Re_{Ld} = 90,000, v_j = 38.4 m/s, u_∞ = 21.5 m/s (e) Water, Re_{Ld} = 140,000, v_j = 59.5 m/s, u_∞ = 21.5 m/s. The crossflow is from left to right in all images.

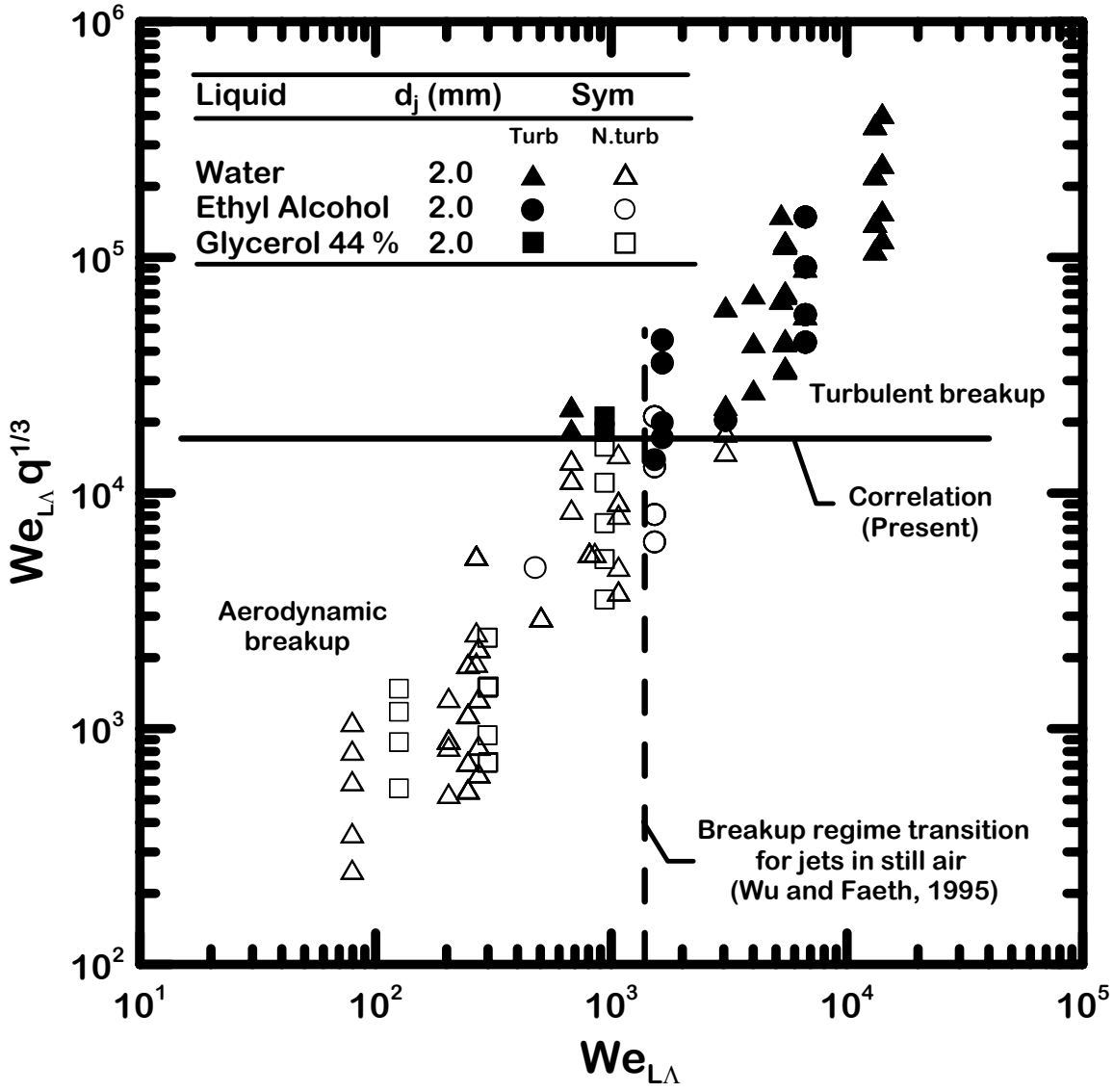

Figure 3.4 Breakup regime map showing transition between non-turbulent breakup and turbulent breakup. Plot shows the plot of the newly discovered number $We_{L\Lambda}q^{1/3}$ as a function of the $We_{L\Lambda}$.

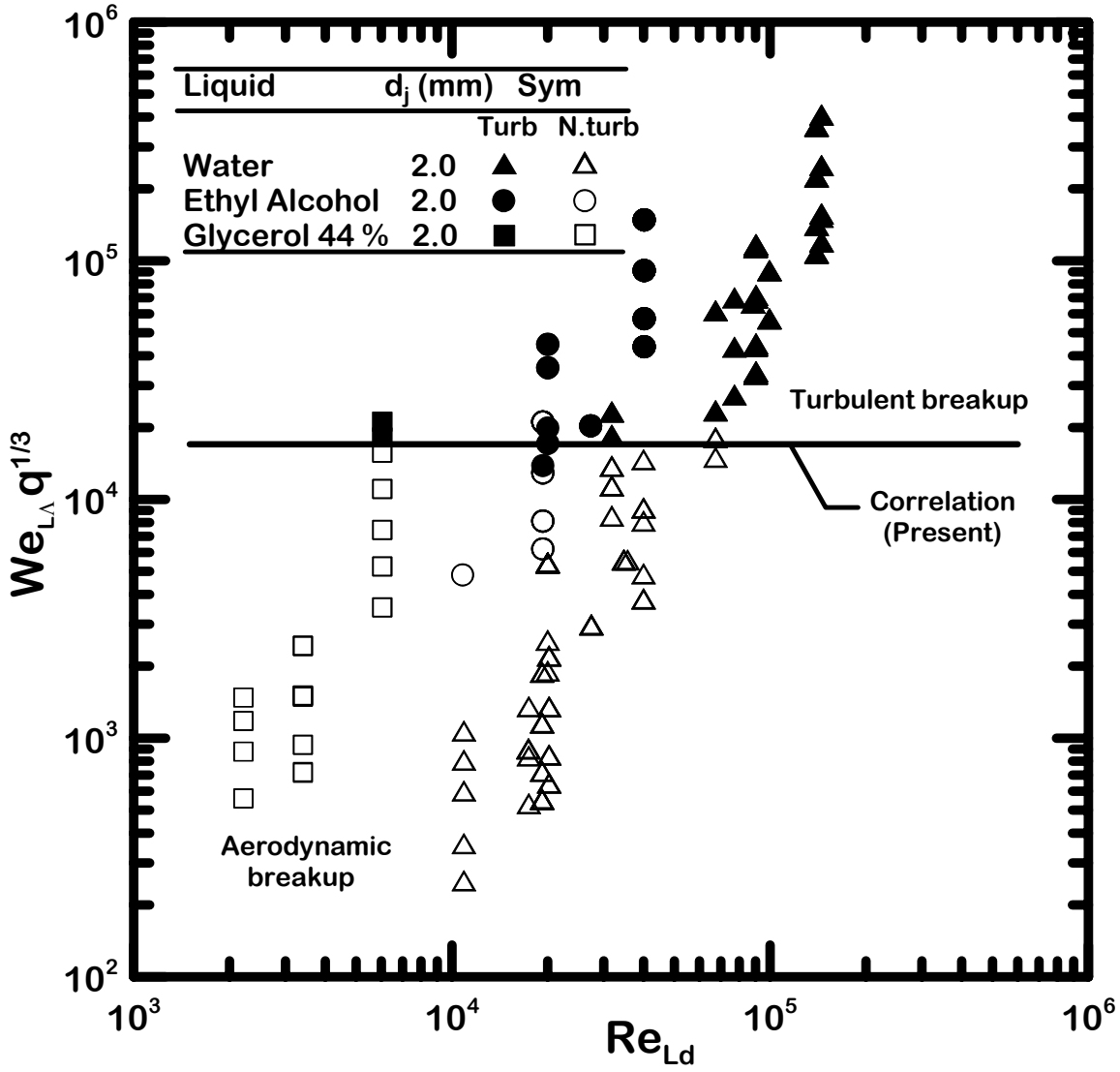

Figure 3.5 Breakup regime map showing transition between non-turbulent breakup and turbulent breakup. Plot shows the plot of the dimensionless number $We_{L\Lambda}q^{1/3}$ as a function of the liquid jet Reynolds number Re_{Ld}.

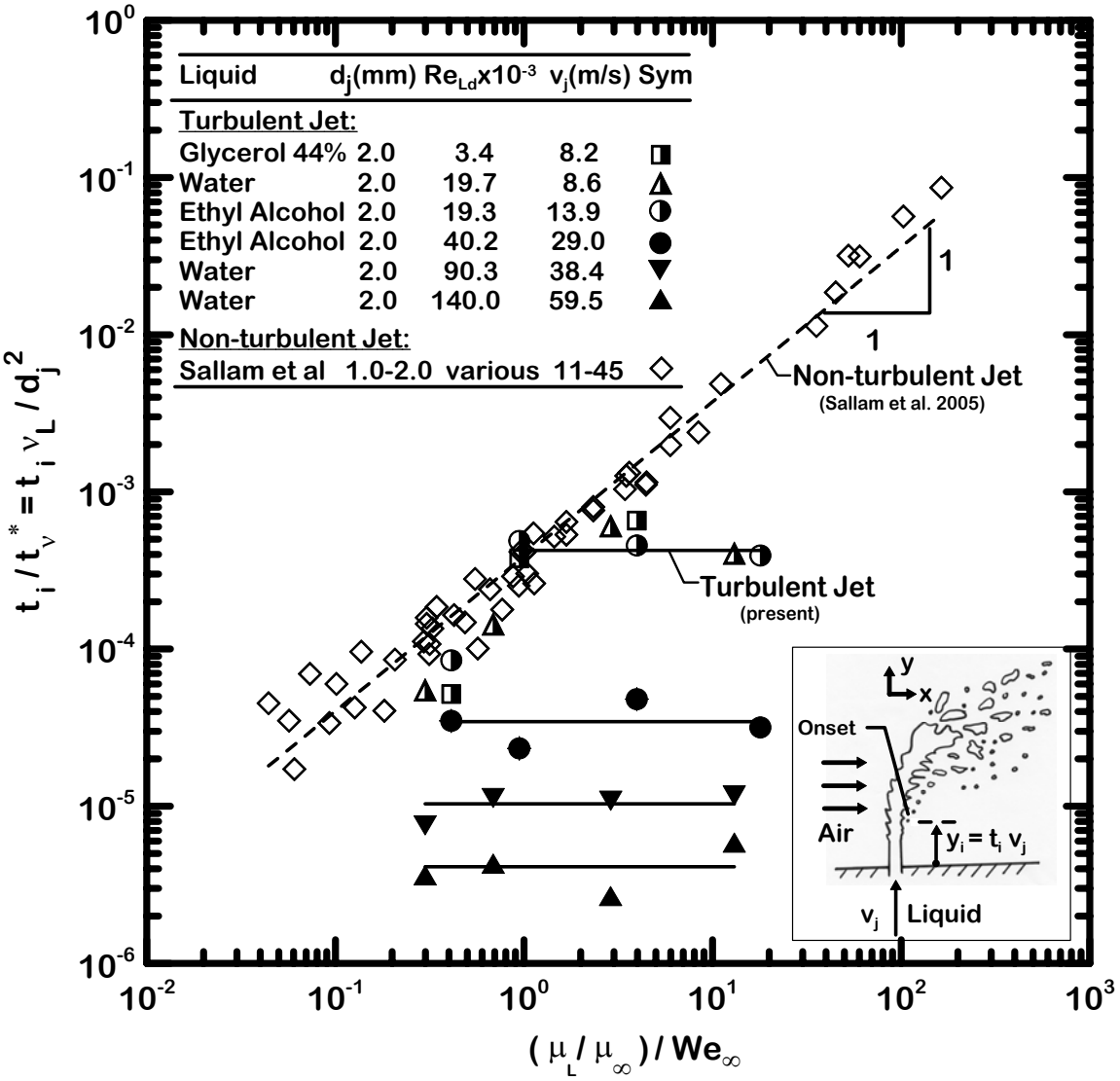

Figure 3.6 Time of onset of breakup showing the time of the onset of ligament formation as a function of $(\mu_L/\mu_\infty)/We_\infty$.

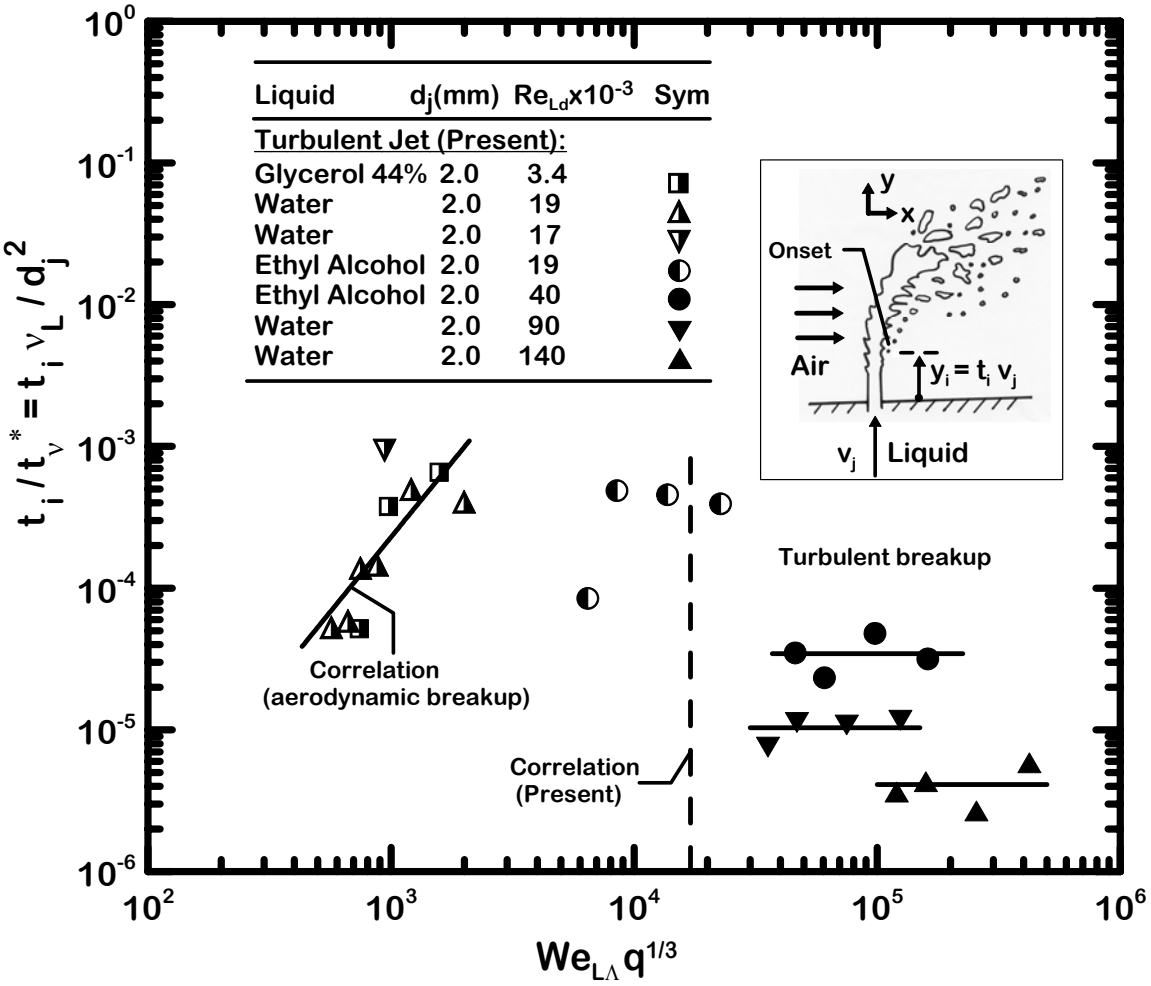

Figure 3.7 Time of onset of breakup showing the time of the onset of ligament formation as a function of the dimensionless parameter $We_{L\Lambda}q^{1/3}$.

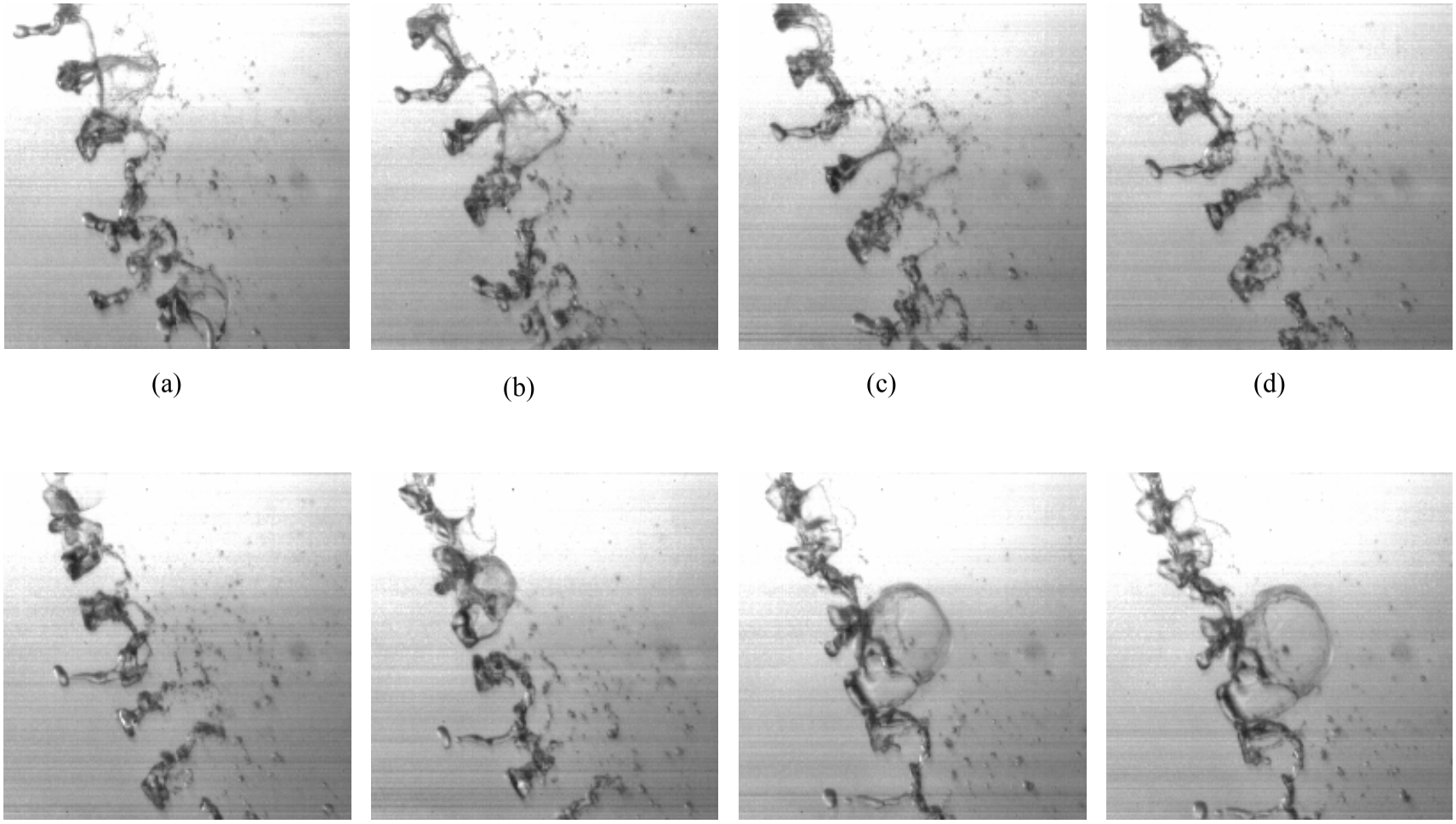

Figure 3.8 Flow visualizations showing formation of bags, growth of bags, breaking of bags, ligament formation and drop pinching off on the upwind side for water liquid jet. $We_\infty = 10$, $d_j = 2.0$ mm, $Re_{Ld} = 19{,}200$, $v_j = 8.2$ m/s, $u_\infty = 16.6$ m/s.

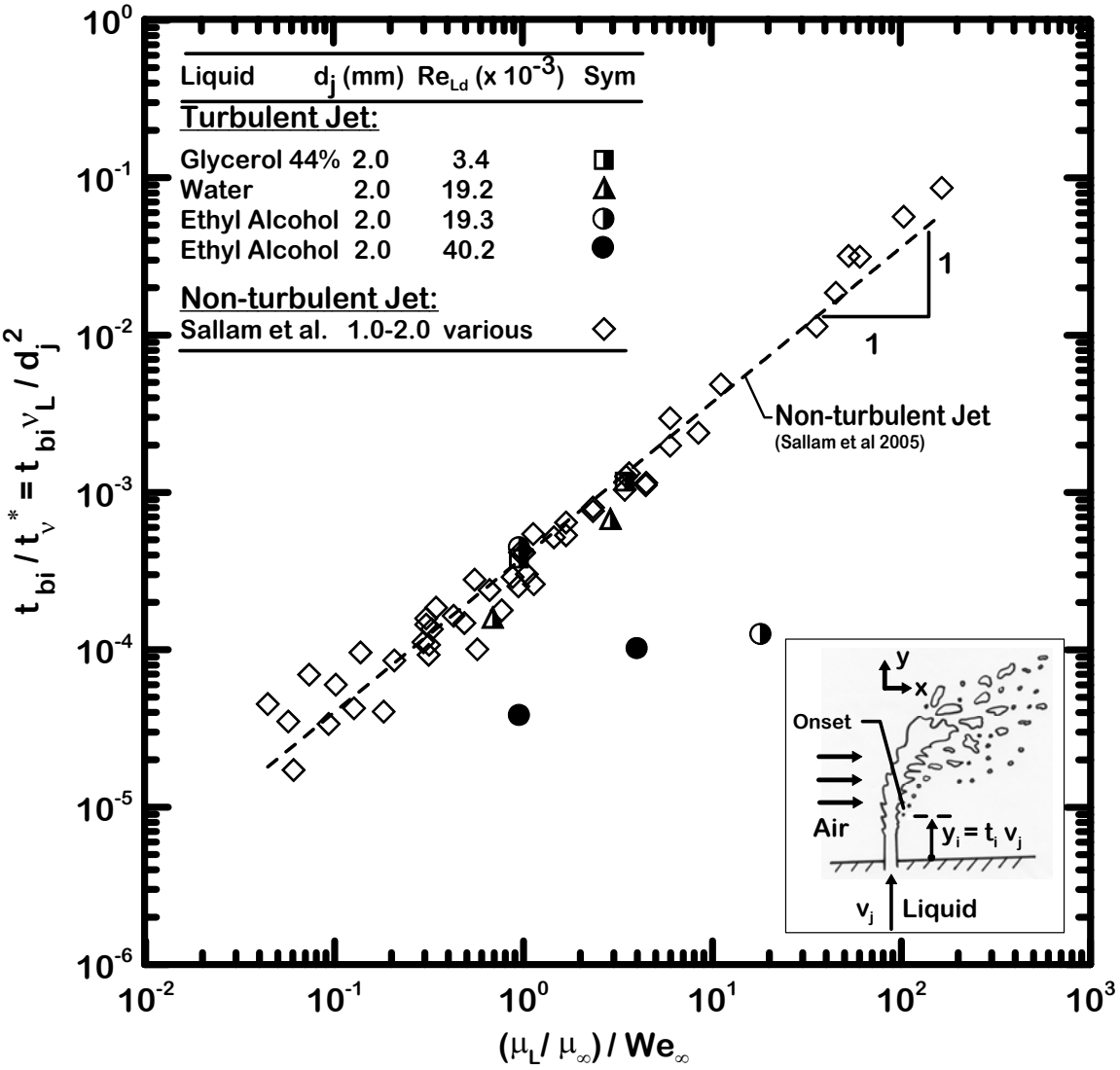

Figure 3.9 Time of onset of bag breakup showing the time of the onset of bag formation as a function of $(\mu_L/\mu_\infty)/We_\infty$.

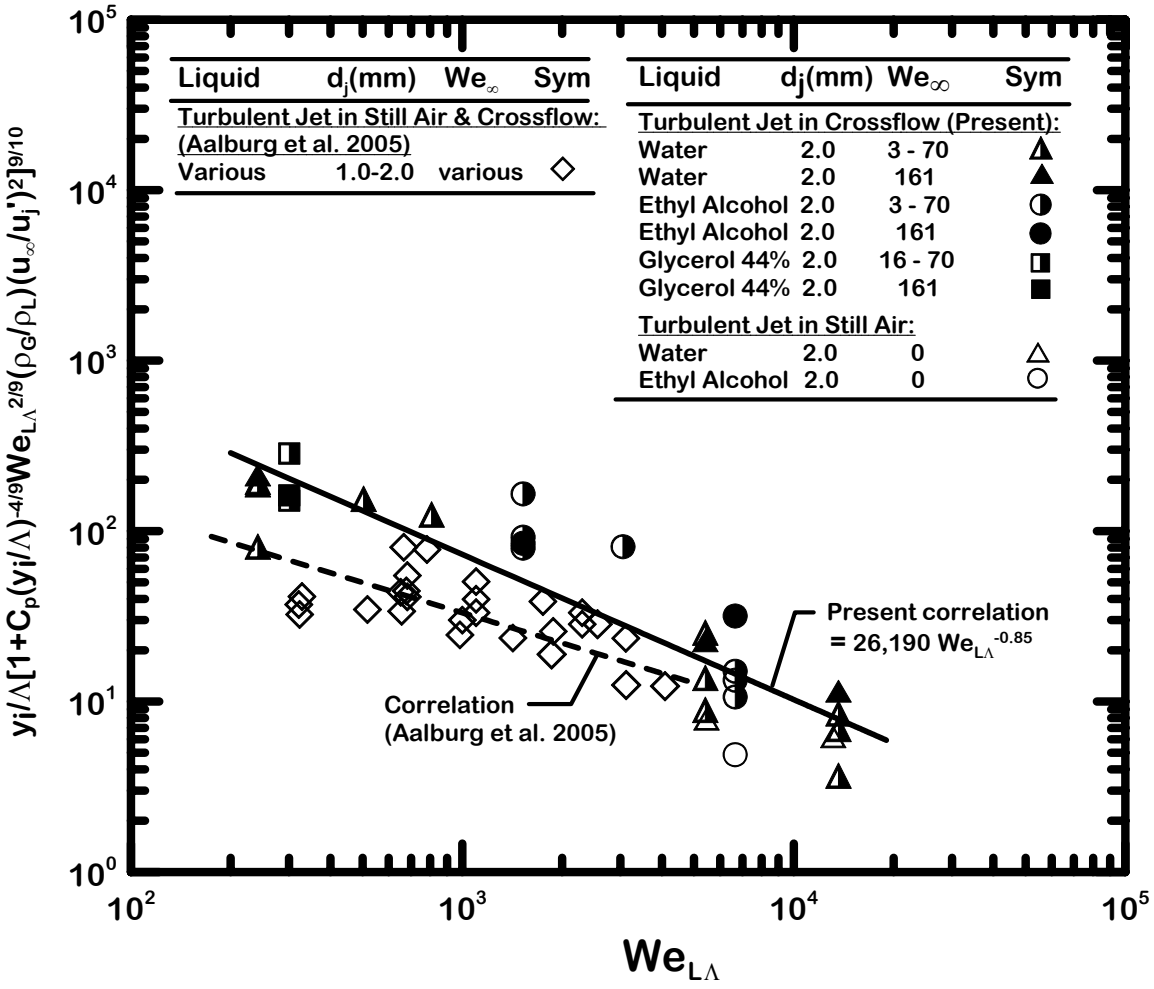

Figure 3.10 Streamwise location of onset of breakup normalized by the radial integral length scale as a function of the liquid jet Weber number based on the radial integral length scale. Also shown are the results of turbulent round liquid jets in still air and crossflow by Aalburg et al. (2005).

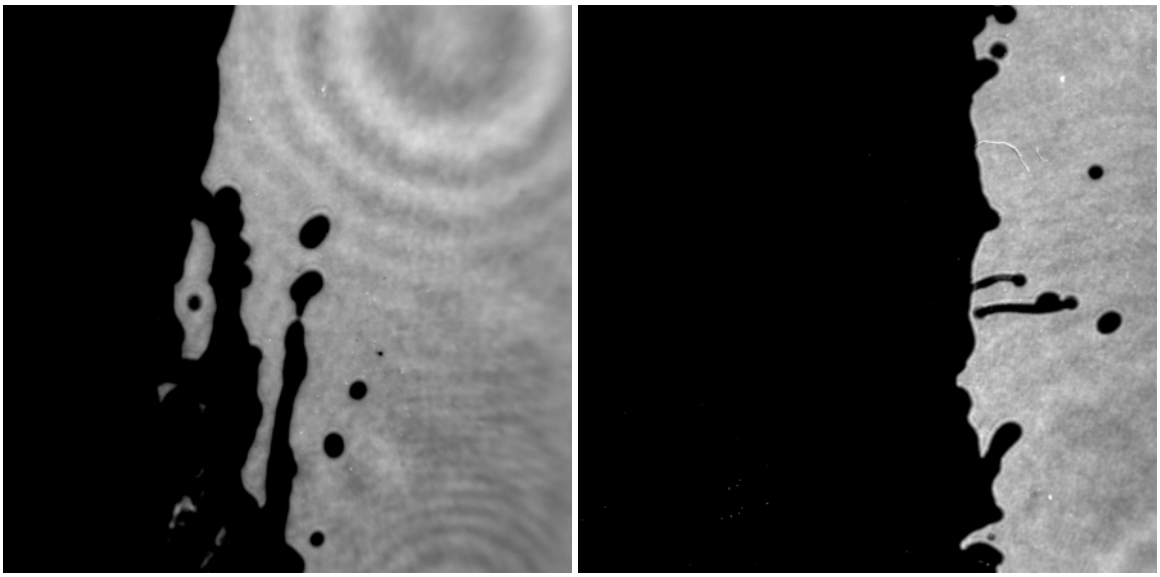

(a) Ligament tip breakup (a) Ligament base breakup

Figure 3.11 Pulsed shadowgraphs of (a) ligament tip (Rayleigh) breakup (d_j =2.0 mm ,We_∞ = 3.71 , Re_{Ld} = 140,000, v_j = 59.5 m/s, u_∞ = 10.1 m/s, ρ_L/ρ_∞ = 820) and (b) ligament base breakup (d_j =2.0 mm ,We_∞ = 16.8 , Re_{Ld} = 40,000, v_j = 29.0 m/s, u_∞ = 13.3 m/s, ρ_L/ρ_∞ = 665)at the surface of turbulent liquid jets.

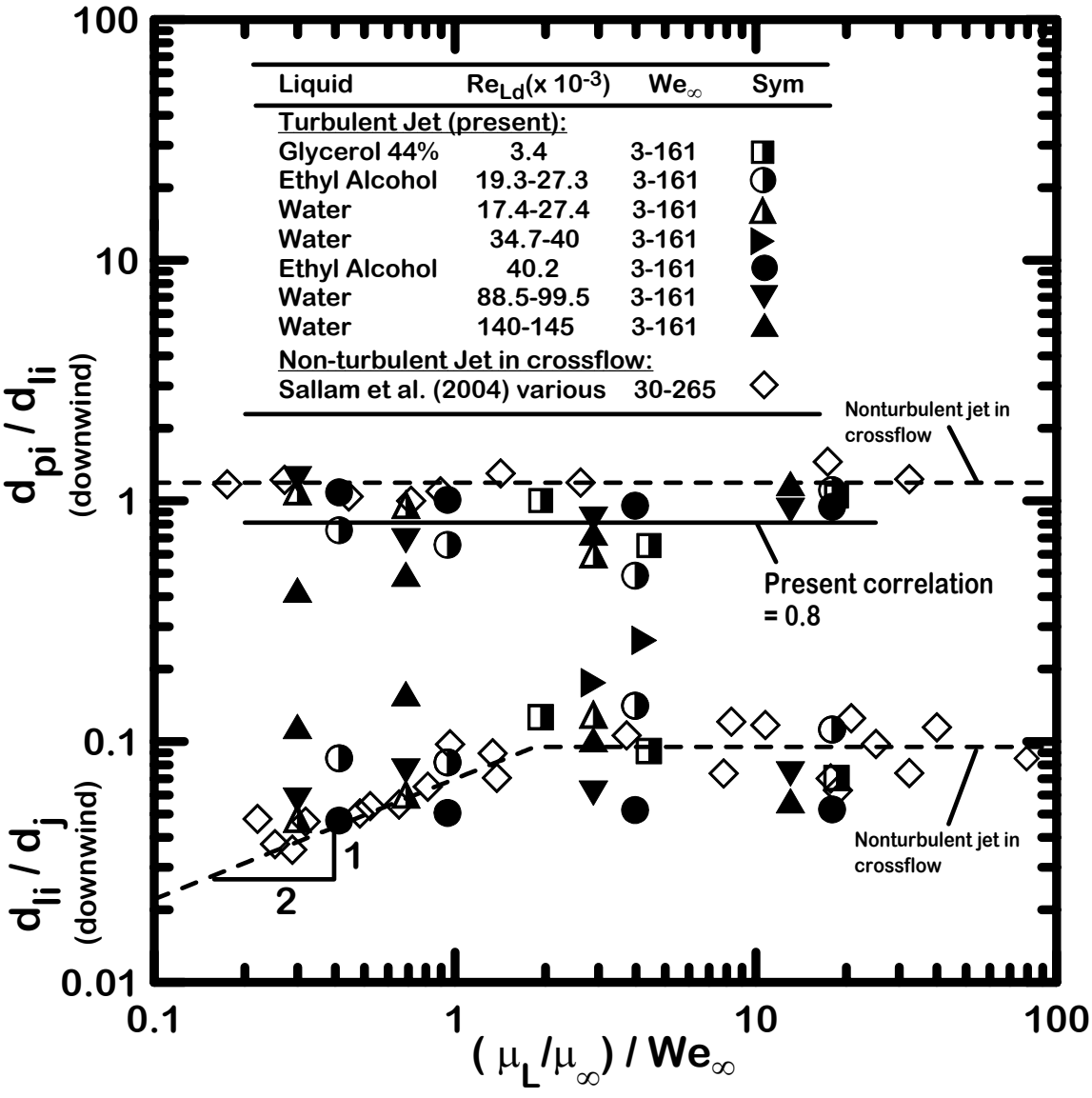

Figure 3.12 Plot showing the drop diameters and ligament diameters on the downwind side of the liquid jet. Also shown on the plot is the correlation of Sallam et al. (2004) for the nonturbulent liquid jets in crossflow.

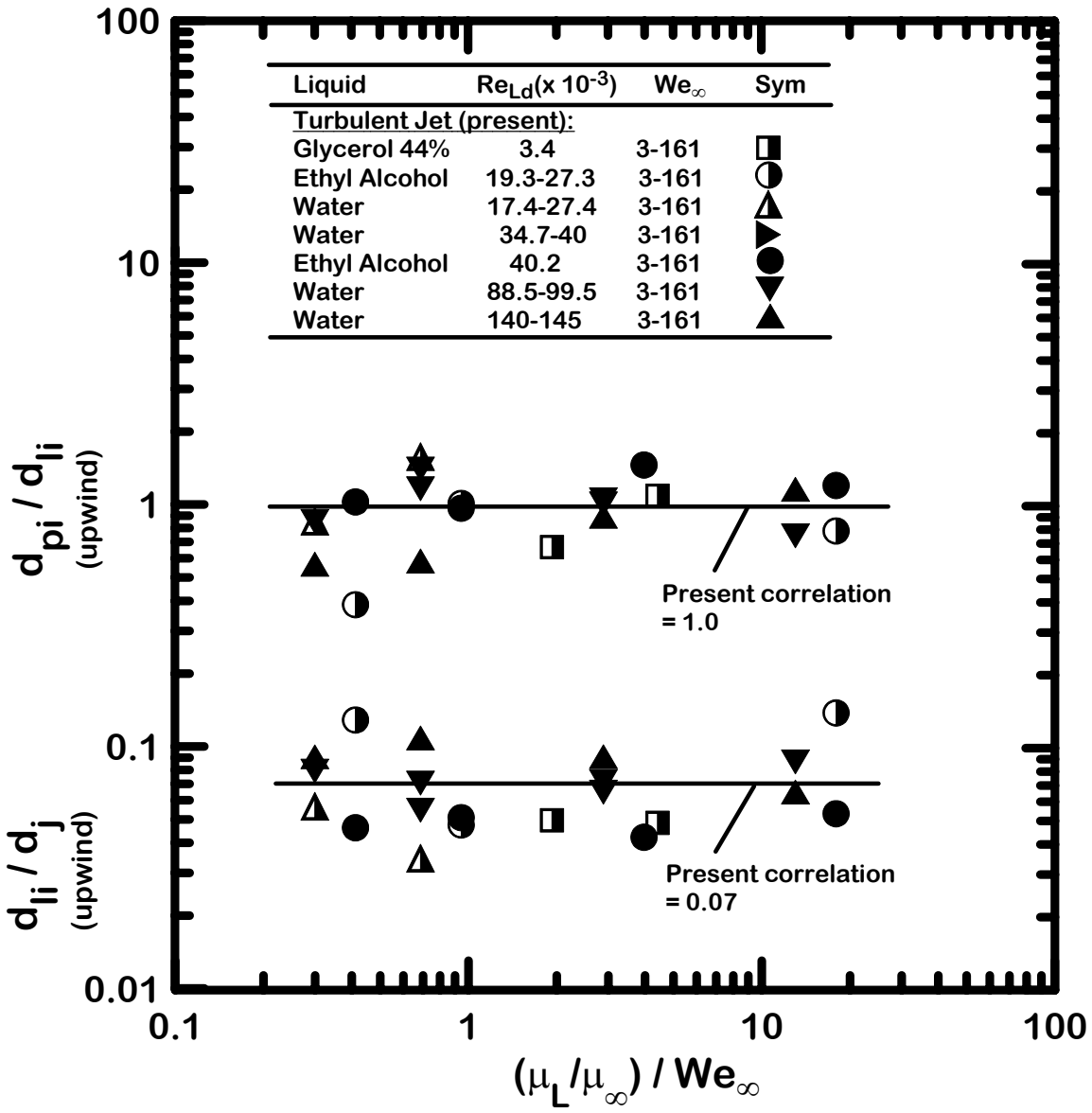

Figure 3.13 Plot showing the drop diameters and ligament diameters on the upwind side of the liquid jet. Absence of results for nonturbulent liquid jets in crossflow indicate turbulent primary breakup is the dominating mechanism for the surface breakup.

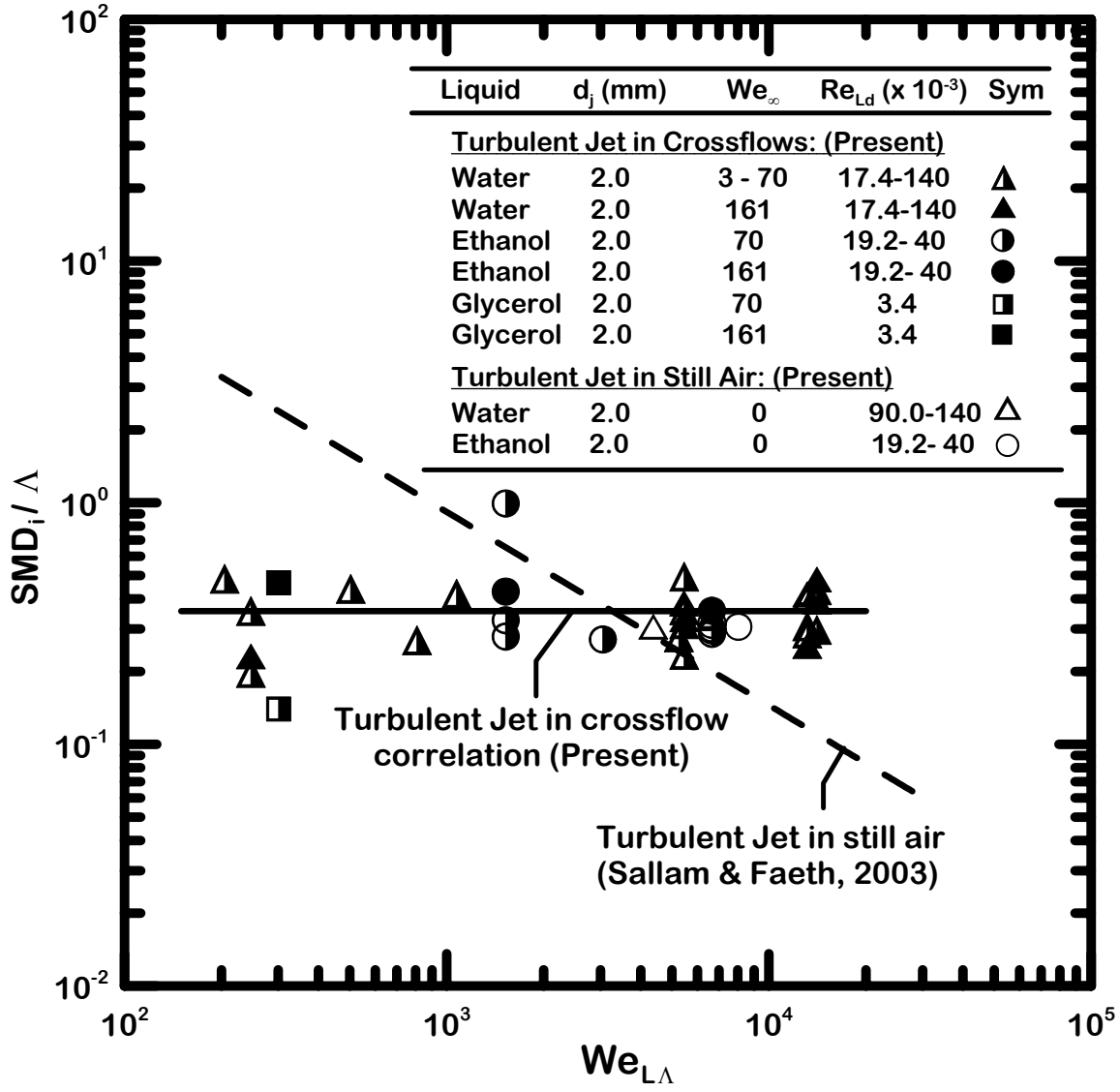

Figure 3.14 The SMD at the onset of turbulent primary breakup as a function of Weber number for turbulent jets in still air and crossflow. Also shown is the correlation for turbulent jets in still air by Sallam and Faeth, 2003.

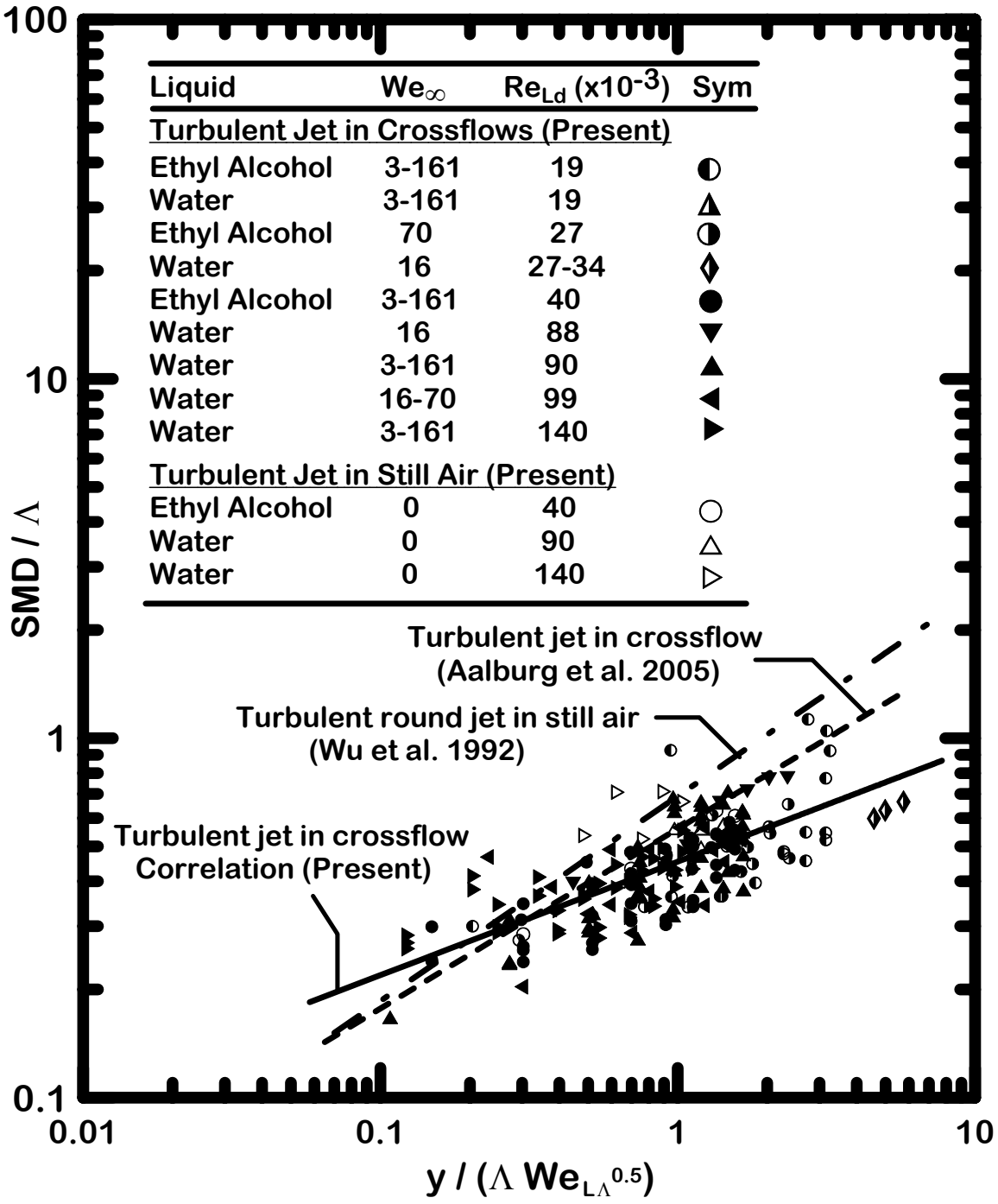

Figure 3.15 The SMD along the streamwise distance of turbulent primary breakup as a function of Weber number based on the radial integral length scale. Also shown are correlations for round jets in still air by Wu et al. (1992) and turbulent jets in crossflow by Aalburg et al. (2005).

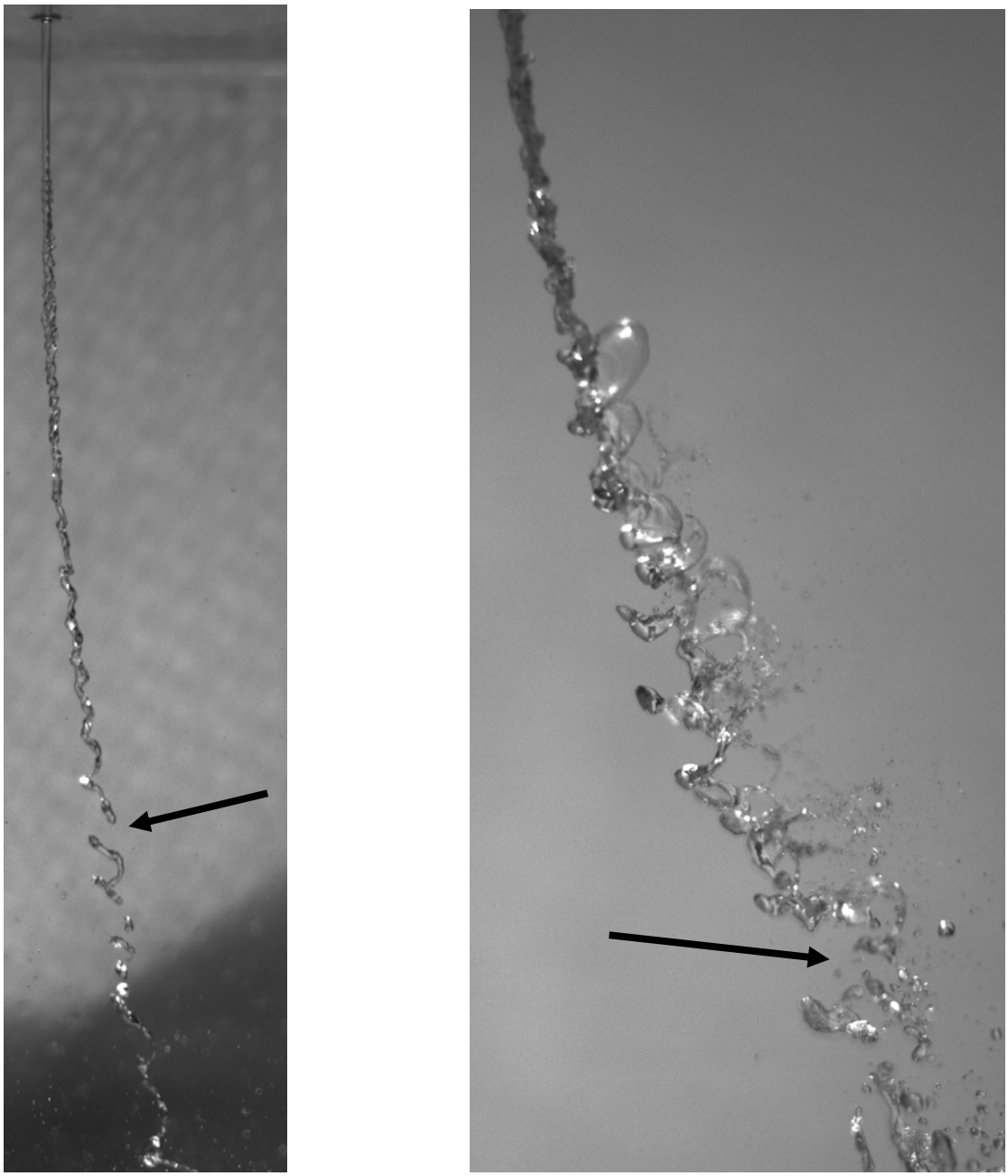

(a) Column breakup (b) Bag breakup

Figure 3.16 Photographs of locations of breakup of liquid core for: (a) Column breakup regime, Liquid: Water, Re_{Ld} = 19,200, We_{∞} = 3, d_j = 2 mm, v_j = 8.15 m/s, u_{∞} = 10.13 m/s; (b) Bag breakup regime, Liquid: Water, Re_{Ld} = 19,200, We_{∞} = 10, d_j = 2 mm, v_j = 8.15 m/s, u_{∞} = 16.63 m/s.

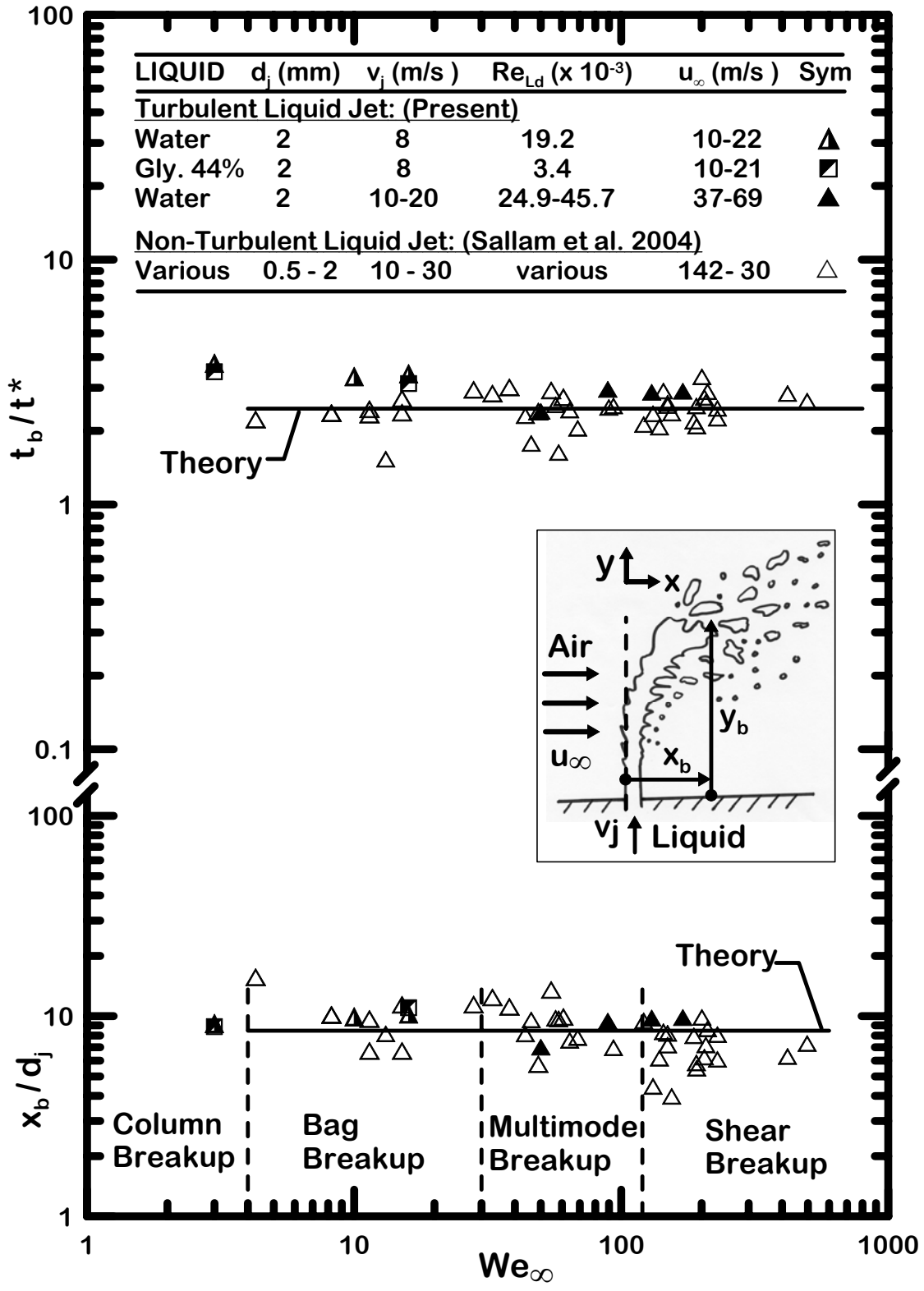

Figure 3.17 Plot showing the breakup time t_b for the end of liquid core in the jet streamwise direction and the location of the end of liquid core x_b in cross stream direction as a function of crossflow Weber number We_∞.

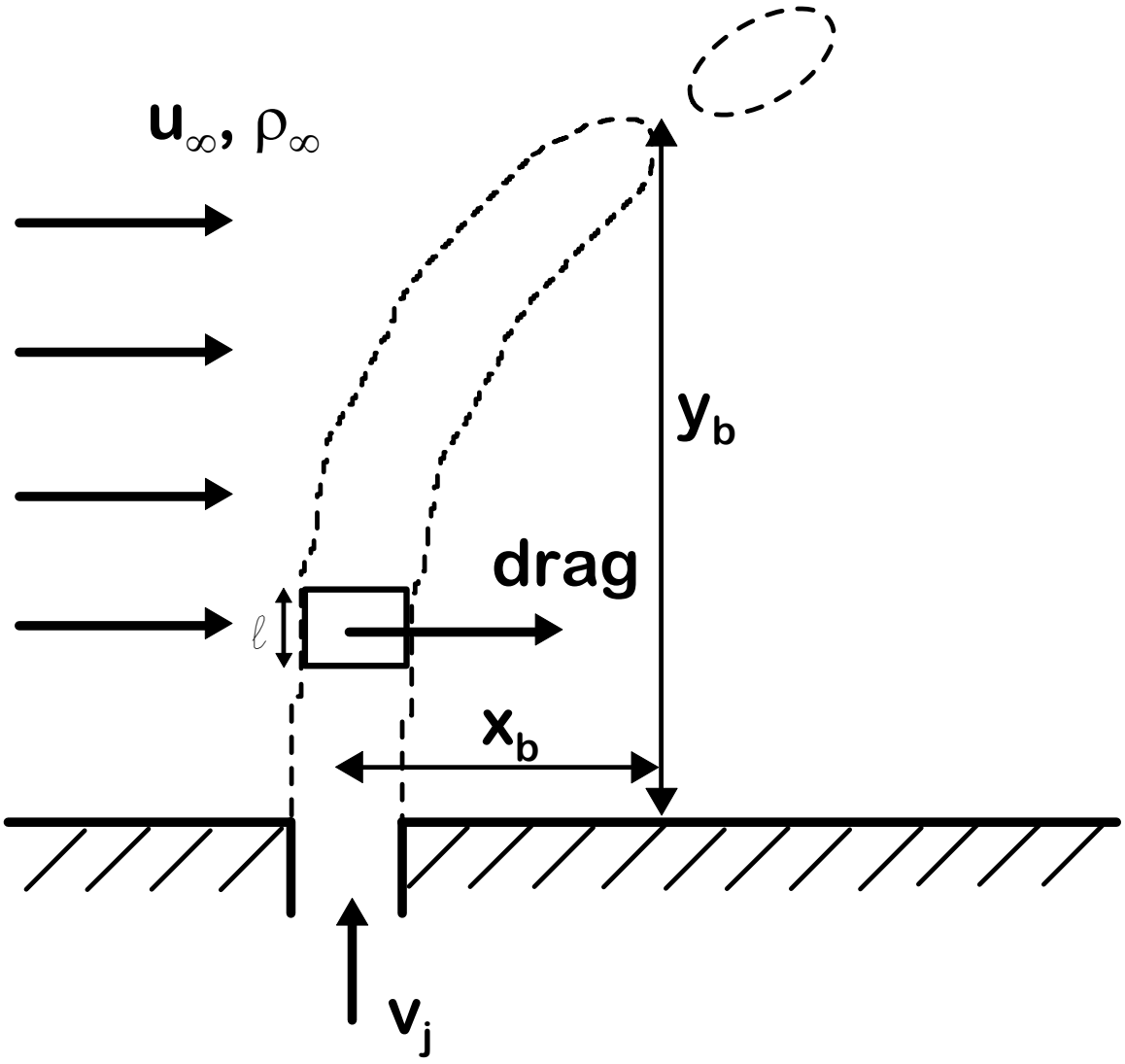

Figure 3.18 Sketch of the force diagram for phenomenological analyses of the liquid column trajectories taken from Wu et al. (1997).

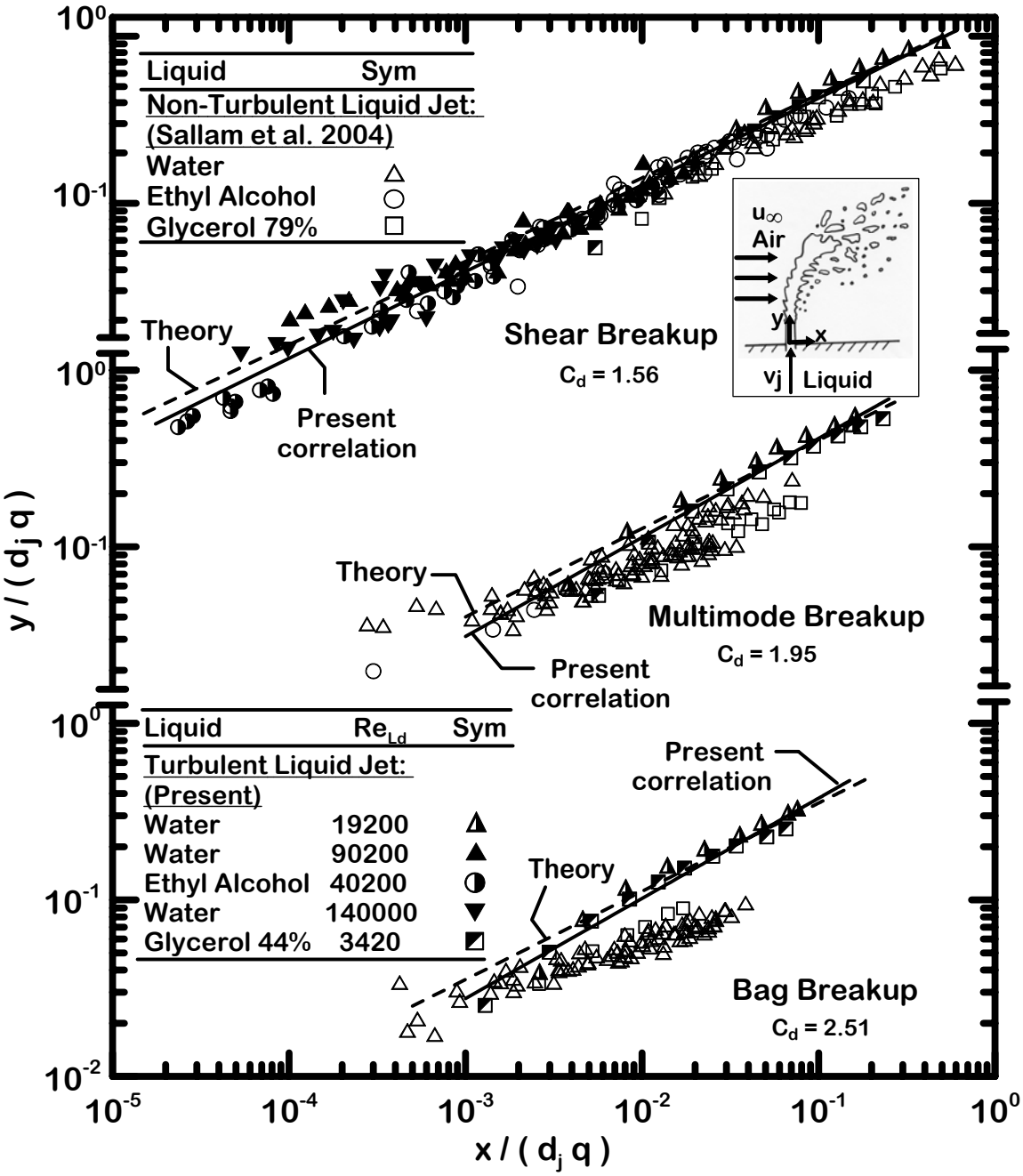

Figure 3.19 Liquid column trajectories for turbulent liquid jets in gaseous crossflow for shear, multimode and bag breakup regimes.

CHAPTER IV

SUMMARY AND CONCLUSIONS

4.1 Summary

Experimental investigation was performed for partially and fully turbulent round liquid jets in uniform gaseous crossflow. Measurements involved breakup regime transitions, properties of onset of breakup, properties of ligaments and drops along the liquid surface, breakup of liquid column as a whole, and liquid column trajectories. The liquid jets were injected into uniform gaseous crossflow generated by a subsonic wind tunnel at normal temperature and pressure, through round nozzles having smooth rounded entries and length/diameter ratios greater than 40:1 to ensure fully developed pipe flow at the jet exit. Test conditions included three liquids, water, ethyl alcohol (190 proof) and glycerol (44% glycerin by mass), jet exit Reynolds number, Re_{Ld} = 2,200 – 140,000, jet exit Weber numbers, We_{Ld} = 1000 – 105,000, jet exit Ohnesorge numbers, Oh_{Ld} = 0.002 – 0.014, liquid/gas density ratios of 820, 665 and 938 respectively, and crossflow Weber number, We_{∞} = 0 – 180. Small values of Ohnesorge numbers (Oh_{Ld} <0.1) implied that viscous effects were negligible.

4.2 Conclusions

The major conclusions of the present investigation of partially and fully turbulent round liquid jets in uniform gaseous crossflow are as follows:

1. Breakup of turbulent liquid jets in crossflow falls into two major regimes known as aerodynamic breakup regime and turbulent breakup regime, separated by the dimensionless parameter $We_{L\Lambda}q^{1/3}$ = 17,000. Aerodynamic breakup regimes of turbulent liquid jets ($We_{L\Lambda}q^{1/3}$ < 17,000) included column, bag, multimode and shear, similar to the non turbulent liquid jets in gaseous crossflow.
2. Time for the onset of aerodynamic breakup of turbulent liquid jets in crossflow resembles that of the nonturbulent liquid jets in crossflow within experimental uncertainties of 56%. However, the time of onset of turbulent breakup is independent of the crossflow Weber number indicating dominance of turbulent primary breakup over the aerodynamic effects.
3. Surprisingly, bag breakup (We_{∞} = 4 – 30) of turbulent round liquid jets exhibits ligament and drop formation on the upwind side. Moreover, the liquid column during bag formation does not undergo considerable deformation.
4. Within the turbulent breakup regime, drop to ligament size ratios support a Rayleigh-like breakup mechanism for the ligaments.
5. Ligament diameters at the onset for the upwind side are similar to those at the downwind side (within uncertainty of 30%) indicating weak crossflow effects.
6. For multimode, shear and turbulent breakup, drop size increases in streamwise distances from the jet exit which is typical of the breakup of turbulent jets in still gases. Drop size at the onset, however, is constant regardless of the liquid jet Weber number, $We_{L\Lambda}$.
7. Breakup of liquid column as a whole for turbulent liquid jets in the column, bag, multimode and shear breakup regime approximated the total times of breakup of

the nonturbulent liquid jets in the column, bag, multimode and shear breakup regime yielding $t_b/t^* = 2.5$ and $x_b/d_j = 8.0$.

8. Trajectories of turbulent liquid jets in crossflow resemble that of the nonturbulent liquid jets in crossflow and are unaffected by the presence of the turbulence in the shear breakup regime. In the bag and multimode breakup regimes, however, the turbulent liquid jet penetrated higher in the crossflow due to the fact that nonturbulent liquid jets in crossflow deform more in comparison with turbulent liquid jets causing them to have larger frontal area and therefore they experience higher drag forces than that of the turbulent liquid jets in crossflow.

4.3 Recommendations for Future Study

The following recommendations are made concerning future study of turbulent round liquid jets in gaseous crossflow, based on the results of the present study:

1. Present study was limited to liquids with moderate viscous effects ($Oh_{Ld} < 0.1$) and liquid/gas density ratios greater than 500. Test conditions with high values of Ohnesorge number and lower liquid/gas density ratios (<500) should be employed to find out the effects of liquid jet Ohnesorge number and aerodynamic effects on the breakup mechanism of turbulent liquid jets in crossflow.
2. Present study employed a nozzle with length to diameter ratio of 40:1 that would result in a fully developed pipe flow at the jet exit. The effects of length to diameter ratio of the injection nozzle should be investigated.

3. Present study was performed in a uniform gaseous crossflow. Effects of different levels of turbulence in the crossflow on the breakup of turbulent liquid jets should be investigated.

REFERENCES

Aalburg, C., Faeth, G.M. and Sallam, K.A. (2005) "Primary Breakup of Round Turbulent Liquid Jets in Uniform Crossflows," *43rd Aerospace Science Meeting and Exhibit*, 10-13 January 2005, paper no. AIAA-2005-0734.

Birouk, M., Stabler, T. and Azzopardi, B.J. (2003) "An Experimental Study of Liquid Jets Interacting with Cross Airflows," *Particle & Particle system characterization* **20**, Issue 1, 39-46.

Andreopoulos, J. and Rodi, W. (1984) "Experimental investigation of Jets in a Crossflow," *J. Fluid Mech.* **138**, 93-127.

Chen, T.-F. and Davis, J.R. (1964) "Disintegration of a Turbulent Water Jet," *J. Hyd. Div., Proc. ASCE* **90**, 175-206.

Chu, H.V. (1985) "Oblique Turbulent Jets in a Crossflow," *J. Engineering* **111**, No. 11, 1343-1360.

Crow, E.L., Davis, F.A. and Maxfield, M.W., "*Statistics Manual*," Dover Publications, New York, 1960, 47-48.

Fuller, P.R., Wu, P.-K., Kirkendall, A.K. and Nejad, S.A. (1995) "Effects of Injection Angle on Atomization of Liquid Jets in Transverse Airflow," *AIAA Journal* **38**, No. 1, 64-72.

Geary, E.L. and Margettes, M.J. (1969) "Penetration of a High Velocity Gas Stream by a Water Jet," *Journal of Spacecraft* **6**, No. 1, 79-81.

Grant, R.P. and Middleman, S. (1966) "Newtonian Jet Stability," *A.I.Ch.E. J.* **12**, 669-678.

Hinze, J.O. (1959) *Turbulence; an introduction to its mechanism and theory*, 1st ed. McGraw-Hill, New York, 427, 724-734.

Hsiang, L.-P. and Faeth, G.M. (1992) "Near-Limit Drop Deformation and Secondary Breakup," *Int. J. Multiphase Flow* **18**, 635-652.

Hsiang, L.-P. and Faeth, G.M. (1993) "Drop Properties after Secondary Breakup," *Int. J. Multiphase Flow* **19**, 721-735.

Hsiang, L.-P. and Faeth, G.M. (1995) "Drop Deformation and Breakup Due to Shock Wave and Steady Disturbances," *Int. J. Multiphase Flow* **21**, 545-560.

Mazallon, J., Dai, Z. and Faeth, G.M. (1999) "Primary Breakup of Nonturbulent Round Liquid Jets in Gas Crossflows," *Atom. Sprays* **9**, 291-311.

Ranger, A.A. and Nicholls, J.A. (1969), "The Aerodynamic Shattering of Liquid Drops," *AIAA Journal* **7**, No. 2, 285-290.

Reichenbach, P.R. and Horn, K.P. (1971) "Investigation of Injectant Properties in Jet Penetration in a Supersonic Stream," *AIAA Journal* **9**, No. 3, 469-471.

Sallam, K.A. (2002) "Properties of Spray Formation by Turbulent Primary Breakup" Ph.D. Dissertation, The University of Michigan.

Sallam, K.A., Dai, Z. and Faeth, G.M. (2002), "Liquid Breakup at the Surface of Turbulent Round Liquid Jets in Still Gases," *International J. Multiphase Flow* 28, No. 3, pp. 427-449.

Sallam, K.A. and Faeth, G.M. (2003), "Surface Properties During Primary Breakup of Turbulent Liquid Jets in Still air," *AIAA Journal* **41**, No. 8, 1514-1524.

Sallam, K.A., Aalburg, C. and Faeth, G.M. (2004) "Breakup of Round Nonturbulent Liquid Jets in Gaseous Crossflow," *AIAA Journal* **42,** No. 12, 2529-2540.

Schetz, A.J. and Padhye, A. (1977) "Penetration and Breakup of Liquids in Subsonic Airstreams," *AIAA Journal* **15**, No. 10, 1385-1390.

Schlichting, H., (1960) *Boundary Layer Theory*, 4th ed. McGraw-Hill, New York, 72-73.

Sherif, S.A. and Pletcher, R.H. (1989) "Measurements of the Flow and Turbulence Characteristics of Round Jets in Crossflow," *J. Fluids Engineering.* **111**, 165-171.

Simmons, H.C. (1977) “The correlation of drop-size distributions in fuel nozzle sprays,” *J. Eng. Power* **99**, 309-319.

Teng, H., Kinoshita, C.M. and Masutani, S.M. (1995) “Prediction of Droplet Size from the Breakup of Cylindrical Liquid Jets,” *Int. J. Multiphase Flow* **21**, 129-136.

Tennekes, H. and Lumley, J.L. (1972) *A First Course in Turbulence*, MIT Press, Cambridge, MA, 248-286.

Wu, P.-K., Tseng, L.-K. and Faeth, G.M. (1992) “Primary Breakup in Gas/Liquid Mixing Layers for Turbulent Liquids,” *Atom. Sprays* **2**, 295-317.

Wu, P.-K. and Faeth, G.M. (1993) “Aerodynamic Effects on Primary Breakup of Turbulent Liquids,” *Atom. Sprays* **3**, 265-289.

Wu, P.-K. and Faeth, G.M. (1995) “Onset and End of Drop Formation along the Surface of Turbulent Liquid Jets in Still Gases,” *Phys. Fluids* **7**, 2915-2917.

Wu, P.-K., Ruff, G.A. and Faeth, G.M. (1991) “Primary Breakup in Liquid-Gas Mixing Layers,” *Atom. Sprays* **1**, 421-440.

Wu, P.-K., Miranda, R.F. and Faeth, G.M. (1995) “Effects of initial flow conditions on primary breakup of non-turbulent and turbulent round liquid jets,” *Atom. Sprays* **5**, 175-196.

Wu, P.-K., Kirkendall, A.K., Fuller, P.R. and Nejad, S.A. (1997) “Breakup Processes of Liquid Jets in Subsonic Crossflows,” *J. Propulsion and Power* **13**, No. 1, 64-73.

Wu, P.-K., Kirkendall, A.K., Fuller, P.R. and Nejad, S.A. (1998) “Spray Structures of Liquid Jets Atomized in Subsonic Crossflows,” *J. Propulsion and Power* **14**, No. 2, 173-182.

APPENDIX A

EXPERIMENTAL DATA

Table A.1 (a) Turbulent Breakup Regime Data:

Liquid	We_{∞}	Re_{Ld}	q	We_{Ld}	$We_{L\Lambda}q^{1/3}$	$We_{L\Lambda}$
Ethanol	70.43	27300	347	24402	20349	3050
	161.52	40200	330	53243	43682	6655
	70.43	40200	756	53243	57162	6655
	16.76	40200	3180	53243	91103	6655
	3.71	40200	14300	53243	148377	6655
	1.2	20000	13149	13146	35652	1643
	0.5	20000	26300	13146	44644	1643
	13.5	19300	903	12198	13873	1525
	6	20000	2190	13146	19930	1643
	9.5	20000	1380	13146	17157	1643
Glycerol	0.5	6040	15000	7490	21199	936
	0.8	6040	9370	7490	18198	936
Water	16.76	140000	6280	105207	224493	13151
	3.71	140000	28400	105207	366298	13151
	161.52	140000	651	105207	107602	13151
	70.43	140000	1490	105207	140765	13151
	161.52	90200	271	43708	33639	5463
	70.43	90200	621	43708	44024	5463
	16.76	90200	2610	43708	70145	5463
	3.71	90200	11800	43708	114443	5463
	70.43	99500	755	53195	57086	6649
	16.76	99500	3170	53195	90928	6649
	70.43	99500	755	53195	57086	6649
	3.71	90000	11700	43526	113652	5441
	16.76	90000	2600	43526	69766	5441
	70.43	90000	618	43526	43771	5441
	161.52	90000	269	43526	33419	5441
	16.76	88500	2500	42038	66529	5255
	3.71	145000	32000	112797	408230	14100
	16.76	145000	7090	112797	250352	14100

Liquid	We_{∞}	Re_{Ld}	q	We_{Ld}	$We_{L\Lambda}q^{1/3}$	$We_{L\Lambda}$
	70.43	145000	1690	112797	157216	14100
	161.52	145000	735	112797	119999	14100
	3.71	90300	12500	43776	116785	5472
	16.76	90300	2760	43776	71540	5472
	70.43	90300	656	43776	44884	5472
	161.52	90300	286	43776	34286	5472
	4.8	77296	6685	32095	69888	4012
	20.8	77296	1543	32095	43430	4012
	86	77296	373	32095	27402	4012
	0.2	31800	27100	5419	18581	677
	0.1	31800	54200	5419	23267	677
	23	67400	10600	24402	61709	3050
	45	67400	542	24402	23517	3050

Table A.1 (b) Aerodynamic Breakup Regime Data:

Liquid	We_{∞}	Re_{Ld}	q	We_{Ld}	$We_{L\Lambda}q^{1/3}$	$We_{L\Lambda}$
Ethanol	3.71	19300	3290	12198	21104	1525
	16.76	19300	727	12198	12931	1525
	70.43	19300	173	12198	8116	1525
	161.52	19300	75.5	12198	6202	1525
	0.5	10800	1270	3802	4830	475
Glycerol	16.76	3420	144	2406	1508	301
	161.52	3420	14.9	2383	715	298
	70.43	3420	34.2	2383	937	298
	3.71	3420	649	2383	2434	298
	0.5	2210	2010	1004	1480	125
	1	2210	1000	1004	1180	125
	2.5	2210	401	1004	877	125
	10	2210	100	1004	559	125
	1.25	6040	5990	7490	15739	936
	3.7	6040	2020	7490	11061	936
	12.5	6040	599	7490	7456	936
	37	6040	202	7490	5240	936
	125	6040	59.9	7490	3532	936
Water	16.76	27400	240	4029	2981	504
	16.76	34700	386	6468	5583	808
	11.35	40000	756	8580	9211	1072
	2.7	40000	3180	8580	14681	1072
	3.71	40000	756	8580	9211	1072

Liquid	We_{∞}	Re_{Ld}	q	We_{Ld}	$We_{L\Lambda}q^{1/3}$	$We_{L\Lambda}$
	16.76	40000	512	8580	8117	1072
	16.76	17400	98	1634	903	204
	3.71	19200	532	1972	1889	246
	16.76	19200	118	1972	1159	246
	70.43	19200	28	1972	727	246
	161.52	19200	12	1972	555	246
	3.71	20200	623	2191	2208	274
	16.76	20200	138	2191	1354	274
	70.43	20200	33	2191	850	274
	161.52	20200	14	2191	649	274
	4.8	17445	341	1634	1355	204
	20.8	17445	79	1634	842	204
	86	17445	19	1634	531	204
	20.8	35624	328	6814	5578	852
	0.5	10900	1270	636	808	80
	1.25	10900	509	636	601	80
	6	10900	106	636	361	80
	18	10900	35	636	253	80
	0.21	10900	3030	636	1072	80
	80	40000	107	8580	4884	1072
	0.2	20000	10700	2140	5428	267
	2	20000	1070	2140	2571	267
	170	40000	51	8580	3828	1072
	5	20000	428	2140	1910	267
	0.5	31800	10800	5419	13786	677
	0.9	31800	6020	5419	11405	677
	2.2	31800	2460	5419	8531	677
	100	67400	244	24402	18152	3050
	180	67400	136	24402	15016	3050

Table A.2 Time at the Onset of Breakup:

Liquid	Re_{Ld}	We_{∞}	q	t_i/t^*_v	$(\mu_L/\mu_g)/We_{\infty}$
Ethanol	19300	3	3290	5.79E-04	1.79E+01
		16	727	4.56E-04	3.97E+00
		70	173	4.88E-04	9.44E-01
		161	76	8.48E-05	4.12E-01
	40200	3	14300	3.17E-05	1.79E+01
		16	3180	4.80E-05	3.97E+00
		70	756	2.33E-05	9.44E-01

Liquid	Re_{Ld}	We_{∞}	q	t_i/t^*_v	$(\mu_L/\mu_g)/We_{\infty}$
		161	330	3.49E-05	4.12E-01
Water	19700	3	532	4.08E-04	1.30E+01
		16	118	6.08E-04	2.88E+00
		70	33	1.44E-04	6.86E-01
		161	14	5.50E-05	2.99E-01
	90000	3	11800	5.30E-06	1.30E+01
		16	2610	6.48E-06	2.88E+00
		70	621	1.40E-05	6.86E-01
		161	271	6.48E-06	2.99E-01
	145000	3	28400	5.86E-06	1.30E+01
		16	6280	2.68E-06	2.88E+00
		70	1490	4.31E-06	6.86E-01
		161	651	3.64E-06	2.99E-01
Glycerol	3420	16	144	6.58E-04	3.97E+00
		70	34	3.78E-04	9.44E-01
		161	15	5.18E-05	4.12E-01

Table A.3 Time of Onset of Bag Formation:

Liquid	Re_{Ld}	We_{∞}	q	t_{bi}/t^*_v	$(\mu_L/\mu_g)/We_{\infty}$
Glycerol	3400	16	144	1.17E-03	3.97E+00
		70	34	4.05E-04	9.44E-01
Water	19200	16	118	6.83E-04	2.88E+00
		70	28	1.61E-04	6.86E-01
Ethanol	19300	3	3290	1.26E-04	1.79E+01
		70	173	4.49E-04	9.44E-01
	40200	16	3180	1.03E-04	3.97E+00
		70	756	3.85E-05	9.44E-01

Table A.4 Streamwise Location of Onset of Breakup (Refer to Fig. 3.9):

Liquid	$We_{L\Lambda}$	v_j (m/s)	u_{∞} (m/s)	y-axis
Water	808	14.8	21.5	1.25E+02
	504	11.7	21.5	1.55E+02
	242	8.2	44.1	1.88E+02
	5441	38.3	10.1	8.94E+00
	13624	60.6	10.1	6.92E+00
	242	8.2	21.5	1.94E+02

Liquid	$We_{L\Lambda}$	v_j (m/s)	u_∞ (m/s)	y-axis
	242	8.2	10.1	8.11E+01
	5441	38.3	21.5	1.38E+01
	5441	38.3	44.1	2.54E+01
	13624	60.6	21.5	3.68E+00
	13624	60.6	44.1	8.53E+00
	242	8.2	66.8	2.13E+02
	5441	38.3	66.8	2.27E+01
	13624	60.6	66.8	1.15E+01
	5406	38.3	0	7.88E+00
	13624	59.5	0	6.22E+00
Ethanol	1525	13.9	6.3	7.94E+01
	6655	29.0	27.3	1.33E+01
	6655	29.0	13.3	1.50E+01
	6655	29.0	6.3	1.06E+01
	6655	29.0	0	4.88E+00
	1525	13.9	13.3	9.21E+01
	1525	13.9	27.3	1.65E+02
	3050	19.7	27.3	8.10E+01
	6655	29.0	41.3	3.17E+01
	1525	13.9	41.3	8.47E+01
Glycerol	301	8.2	42.9	2.85E+02
	301	8.2	20.9	1.51E+02
	301	8.2	65	1.62E+02

Table A.5 Drop Sizes Measured by SMD along the Streamwise Distance:

Liquid	We_∞	Re_{Ld}	$We_{L\Lambda}$	SMD/Λ	$y/(\Lambda\ We_{L\Lambda}^{0.5})$
Water	0	90000	5441	6.31E-01	1.65E+00
				5.24E-01	1.48E+00
				4.98E-01	1.20E+00
				5.61E-01	9.75E-01
				3.68E-01	7.46E-01
	0	90200	5464	5.76E-01	1.42E+00
				5.62E-01	1.20E+00
				3.95E-01	7.34E-01
				3.86E-01	5.03E-01
	0	140000	13149	5.37E-01	4.88E-01
				7.08E-01	6.29E-01
				5.24E-01	7.69E-01

Liquid	We_{∞}	Re_{Ld}	$We_{L\Lambda}$	SMD/Λ	$y/(\Lambda\ We_{L\Lambda}^{0.5})$
				7.11E-01	9.02E-01
				6.66E-01	1.05E+00
Ethanol	0	40200	6654	6.08E-01	1.56E+00
				6.29E-01	1.35E+00
				5.67E-01	1.13E+00
				4.72E-01	9.12E-01
				4.34E-01	6.98E-01
				3.92E-01	5.16E-01
				2.85E-01	3.02E-01
Water	3	90000	5441	6.30E-01	1.65E+00
				7.14E-01	1.48E+00
				6.70E-01	1.20E+00
				6.53E-01	9.75E-01
				4.58E-01	7.46E-01
	3	90200	5464	6.20E-01	1.66E+00
				6.61E-01	1.42E+00
				6.52E-01	1.20E+00
				6.86E-01	9.65E-01
				5.04E-01	7.34E-01
				4.01E-01	5.03E-01
				2.36E-01	2.72E-01
	3	140000	13149	4.14E-01	2.07E-01
				4.10E-01	3.44E-01
				3.68E-01	4.88E-01
				4.45E-01	6.29E-01
				4.67E-01	7.69E-01
				4.96E-01	9.02E-01
				5.54E-01	1.05E+00
Ethanol	3	19300	1524	1.05E+00	3.17E+00
				1.13E+00	2.75E+00
				9.26E-01	9.48E-01
				9.23E-01	3.26E+00
	3	40200	6654	5.23E-01	1.56E+00
				5.39E-01	1.35E+00
				5.00E-01	1.13E+00
				4.47E-01	9.12E-01
				3.92E-01	6.98E-01
				3.21E-01	5.16E-01
				3.46E-01	3.02E-01
				2.99E-01	1.49E-01
Water	16	17400	204	1.13E+00	1.19E+01
				8.89E-01	1.03E+01
				4.65E-01	8.69E+00

Liquid	We_{∞}	Re_{Ld}	$We_{L\Lambda}$	SMD/Λ	$y/(\Lambda\ We_{L\Lambda}^{0.5})$
				6.04E-01	7.04E+00
				6.65E-01	5.44E+00
	16	27400	503	6.65E-01	5.75E+00
				6.30E-01	4.99E+00
	16	34700	808	5.98E-01	4.57E+00
	16	88500	5256	7.76E-01	2.34E+00
				7.69E-01	2.03E+00
				7.12E-01	1.71E+00
				6.62E-01	1.39E+00
				5.01E-01	1.07E+00
				3.94E-01	4.45E-01
	16	90000	5441	5.76E-01	1.65E+00
				5.59E-01	1.48E+00
				6.16E-01	1.20E+00
				6.26E-01	9.75E-01
				4.14E-01	7.46E-01
	16	90200	5464	5.27E-01	1.66E+00
				5.35E-01	1.42E+00
				5.94E-01	1.20E+00
				4.35E-01	9.65E-01
				3.97E-01	7.34E-01
				2.99E-01	5.03E-01
				2.39E-01	2.72E-01
	16	99500	6649	5.21E-01	1.62E+00
				4.53E-01	1.41E+00
				5.64E-01	1.21E+00
				5.65E-01	1.01E+00
				4.91E-01	7.91E-01
				3.44E-01	5.86E-01
				3.34E-01	3.72E-01
				5.30E-01	1.49E+00
				4.89E-01	1.30E+00
				4.66E-01	1.10E+00
				4.62E-01	9.07E-01
				2.88E-01	6.93E-01
				3.25E-01	4.93E-01
				2.03E-01	2.98E-01
	16	140000	13149	3.79E-01	2.07E-01
				3.64E-01	3.44E-01
				3.57E-01	4.88E-01
				3.84E-01	6.29E-01
				4.28E-01	7.69E-01
				4.35E-01	9.02E-01

Liquid	We_{∞}	Re_{Ld}	$We_{L\Lambda}$	SMD/Λ	$y/(\Lambda\ We_{L\Lambda}^{0.5})$
				4.83E-01	1.05E+00
				4.68E-01	1.13E+00
				4.29E-01	9.93E-01
				4.62E-01	8.40E-01
				4.01E-01	6.95E-01
				3.95E-01	5.49E-01
				3.32E-01	4.00E-01
				3.45E-01	2.51E-01
				2.83E-01	1.24E-01
Ethanol	16	19300	1524	7.74E-01	3.15E+00
	16	40200	6654	5.84E-01	1.49E+00
				4.96E-01	1.30E+00
				5.29E-01	1.10E+00
				4.92E-01	9.07E-01
				4.82E-01	6.93E-01
				4.52E-01	4.93E-01
				3.13E-01	2.98E-01
				5.55E-01	1.56E+00
				5.42E-01	1.35E+00
				5.21E-01	1.13E+00
				4.43E-01	9.12E-01
				4.21E-01	6.98E-01
				2.88E-01	5.16E-01
				2.64E-01	3.02E-01
Glycerol	16	3420	301	4.94E-01	9.79E+00
				4.18E-01	8.48E+00
Water	70	90000	5441	5.50E-01	1.65E+00
				4.29E-01	1.48E+00
				4.70E-01	1.20E+00
				4.31E-01	9.75E-01
				3.62E-01	7.46E-01
				3.25E-01	5.20E-01
	70	90200	5464	3.80E-01	1.66E+00
				3.86E-01	1.42E+00
				3.88E-01	1.20E+00
				3.38E-01	9.65E-01
				3.72E-01	7.34E-01
				3.19E-01	5.03E-01
				2.38E-01	2.72E-01
	70	99500	6649	5.28E-01	1.62E+00
				5.09E-01	1.41E+00
				3.43E-01	1.21E+00
				3.52E-01	1.01E+00

Liquid	We_{∞}	Re_{Ld}	$We_{L\Lambda}$	SMD/Λ	$y/(\Lambda\ We_{L\Lambda}^{0.5})$
				3.74E-01	7.91E-01
				4.90E-01	5.86E-01
				3.86E-01	3.72E-01
				4.67E-01	2.28E-01
	70	140000	13149	4.33E-01	1.13E+00
				3.86E-01	9.93E-01
				3.58E-01	8.40E-01
				3.18E-01	6.95E-01
				2.98E-01	5.49E-01
				2.86E-01	4.00E-01
				2.88E-01	2.51E-01
				2.70E-01	1.24E-01
Ethanol	70	19300	1524	5.46E-01	3.15E+00
				4.56E-01	2.70E+00
				4.77E-01	2.27E+00
	70	27300	3051	6.55E-01	2.35E+00
				5.67E-01	2.03E+00
				4.26E-01	1.63E+00
				6.11E-01	1.31E+00
				4.13E-01	9.62E-01
				2.74E-01	2.92E-01
				3.40E-01	7.73E-01
				3.39E-01	1.08E+00
				3.63E-01	1.41E+00
				4.98E-01	1.72E+00
				5.44E-01	2.04E+00
				4.64E-01	2.37E+00
				4.33E-01	1.12E+00
				5.00E-01	1.46E+00
				4.47E-01	1.79E+00
	70	40200	6654	4.30E-01	1.56E+00
				4.09E-01	1.35E+00
				3.54E-01	1.13E+00
				3.03E-01	9.12E-01
				3.47E-01	6.98E-01
				2.69E-01	5.16E-01
				2.57E-01	3.02E-01
				2.40E-01	1.49E-01
Water	161	90200	5464	4.75E-01	1.66E+00
				3.21E-01	9.65E-01
				2.77E-01	7.34E-01
				2.91E-01	5.03E-01
				3.16E-01	2.72E-01

Liquid	We_∞	Re_{Ld}	$We_{L\Lambda}$	SMD/Λ	$y/(\Lambda\ We_{L\Lambda}^{0.5})$
				1.67E-01	1.08E-01
	161	140000	13149	3.41E-01	8.40E-01
				3.22E-01	6.95E-01
				2.78E-01	5.49E-01
				2.93E-01	4.00E-01
				2.98E-01	2.51E-01
				2.60E-01	1.24E-01
Ethanol	161	19300	1524	5.21E-01	3.15E+00
				5.48E-01	2.70E+00
				4.84E-01	2.27E+00
				3.96E-01	1.83E+00
				3.64E-01	1.39E+00
				3.62E-01	9.52E-01
				3.94E-01	5.15E-01
				3.00E-01	2.04E-01
	161	40200	6654	4.92E-01	1.56E+00
				4.44E-01	1.35E+00
				3.40E-01	1.13E+00
				3.13E-01	9.12E-01
				3.10E-01	6.98E-01
				2.58E-01	5.16E-01
				2.39E-01	3.02E-01
				2.42E-01	1.49E-01

Table A.6 Drop Sizes at the Onset Measured by SMD:

Liquid	$We_{L\Lambda}$	v_j (m/s)	u_∞ (m/s)	SMD_i/Λ
Water	504	11.7	21.5	4.40E-01
	808	14.8	21.5	2.70E-01
	13151	59.5	21.5	3.08E-01
	1072	17.0	21.5	4.20E-01
	6649	42.3	44.1	3.44E-01
	6649	42.3	21.5	3.39E-01
	204	7.4	21.5	4.84E-01
	5255	37.6	21.5	2.77E-01
	246	8.2	21.5	3.56E-01
	14100	61.6	10.1	3.97E-01
	13151	59.5	10.1	4.07E-01
	5460	38.4	44.1	3.59E-01
	5460	38.4	10.1	4.94E-01

Liquid	$We_{L\Lambda}$	v_j (m/s)	u_∞ (m/s)	SMD_i/Λ
	246	8.2	44.1	1.97E-01
	14100	61.6	21.5	2.97E-01
	5460	38.4	21.5	3.14E-01
	14100	61.6	44.1	4.34E-01
	13151	59.5	44.1	2.87E-01
	5460	38.4	10.1	2.34E-01
	5460	38.4	66.8	3.29E-01
	13151	59.5	66.8	2.55E-01
	246	8.2	66.8	2.31E-01
	14100	61.6	66.8	4.81E-01
	13151	59.5	0	4.01E-01
	5452	38.4	0	3.68E-01
Ethanol	3050	19.7	27.3	2.72E-01
	1525	13.9	6.3	9.92E-01
	1525	13.9	13.3	3.26E-01
	1525	13.9	27.3	2.79E-01
	6655	29.0	27.3	2.96E-01
	6655	29.0	13.3	2.87E-01
	6655	29.0	6.3	3.00E-01
	6655	29.0	41.3	3.57E-01
	1525	13.9	41.3	4.28E-01
	6655	29.0	0	3.15E-01
Glycerol	301	8.2	42.9	1.40E-01
	301	8.2	65	4.67E-01

Table A.7 Drop and Ligament Diameters at Onset on Downwind Side:

Liquid	Re_{Ld}	v_j (m/s)	u_∞ (m/s)	d_{pi}/d_{li}	d_{li}/d_j	$(\mu_L/\mu_\infty)/We_\infty$
Water	19200	8.2	21.5	6.36E-01	1.20E-01	2.88E+00
	19200	8.2	44.1	9.68E-01	6.06E-02	6.86E-01
	19200	8.2	66.7	1.10E+00	4.80E-02	2.99E-01
	27400	11.7	21.5	5.72E-01	1.40E-01	2.88E+00
	34700	14.8	21.5	2.29E-01	1.87E-01	2.88E+00
	90200	38.4	66.7	1.23E+00	5.71E-02	2.99E-01
	90200	38.4	44.1	6.76E-01	8.43E-02	6.86E-01
	90200	38.4	21.5	6.76E-01	8.05E-02	2.88E+00
	90200			9.12E-01	7.33E-02	1.30E+01
	99500			6.89E-01	6.67E-02	6.86E-01
	99500			1.00E+00	4.17E-02	2.88E+00
	140000			7.36E-01	1.02E-01	2.88E+00

Liquid	Re_{Ld}	v_j (m/s)	u_∞ (m/s)	d_{pi}/d_{li}	d_{li}/d_j	$(\mu_L/\mu_\infty)/We_\infty$
	140000			1.18E+00	5.67E-02	1.30E+01
	140000	59.5	66.7	4.26E-01	1.16E-01	2.99E-01
	140000	59.5	44.1	4.96E-01	1.58E-01	6.86E-01
Ethanol	19300	13.9	6.3	1.11E+00	1.12E-01	1.79E+01
	19300	13.9	13.3	4.89E-01	1.41E-01	3.97E+00
	19300	13.9	27.3	5.15E-01	9.67E-02	9.44E-01
	19300	13.9	41.3	7.55E-01	8.52E-02	4.12E-01
	27300	19.7	27.3	7.98E-01	6.71E-02	9.44E-01
	40200	29.0	41.3	1.09E+00	4.70E-02	4.12E-01
	40200	29.0	27.3	1.01E+00	5.05E-02	9.44E-01
	40200	29.0	13.3	9.55E-01	5.19E-02	3.97E+00
	40200	29.0	6.3	9.45E-01	5.22E-02	1.79E+01
Glycerol	3420	8.2	20.9	1.05E+00	7.06E-02	1.85E+01
	3420	8.2	65.0	1.00E+00	1.26E-01	1.92E+00
	3420	8.2	42.9	6.52E-01	9.13E-02	4.41E+00

Table A.8 Drop and Ligament Diameters at Onset on Upwind Side:

Liquid	Re_{Ld}	v_j (m/s)	u_∞ (m/s)	d_{pi}/d_{li}	d_{li}/d_j	$(\mu_L/\mu_\infty)/We_\infty$
Water	19200	8.2	44.1	1.80E+00	3.45E-02	6.86E-01
	19200	8.2	66.7	9.29E-01	5.66E-02	2.99E-01
	90200	38.4	66.7	8.51E-01	7.92E-02	2.99E-01
	90200	38.4	44.1	1.16E+00	7.06E-02	6.86E-01
	90200	38.4	21.5	1.05E+00	7.15E-02	2.88E+00
	90200	38.4	10.1	7.42E-01	8.62E-02	1.30E+01
	99500	42.3	44.1	1.40E+00	5.45E-02	6.86E-01
	99500	42.3	21.5	1.01E+00	6.48E-02	2.88E+00
	140000	59.5	21.5	9.08E-01	9.07E-02	2.88E+00
	140000	59.5	10.1	1.17E+00	6.49E-02	1.30E+01
	140000	59.5	66.7	5.75E-01	9.06E-02	2.99E-01
	140000	59.5	44.1	5.93E-01	1.09E-01	6.86E-01
Ethanol	19300	13.9	6.3	7.89E-01	1.38E-01	1.79E+01
	19300	13.9	41.3	3.91E-01	1.29E-01	4.12E-01
	27300	19.7	27.3	1.03E+00	4.73E-02	9.44E-01
	40200	29.0	41.3	1.04E+00	4.61E-02	4.12E-01
	40200	29.0	27.3	9.80E-01	5.08E-02	9.44E-01
	40200	29.0	13.3	1.48E+00	4.21E-02	3.97E+00
	40200	29.0	6.3	1.22E+00	5.27E-02	1.79E+01
Glycerol	3400	8.2	65.0	6.77E-01	4.96E-02	1.92E+00
	3400	8.2	42.9	1.11E+00	4.83E-02	4.41E+00

Table A.9 Time of Breakup of Liquid Core and Location of End of Liquid Core:

Liquid	We_∞	Re_{Ld}	q	x_b/d_j	t_b/t^*
Water	3	19200	532	9.19E+00	3.78E+00
	10	19200	197	9.93E+00	3.33E+00
	16	19200	118	1.03E+01	3.42E+00
	50	24900	67	7.00E+00	2.40E+00
	89	33300	67	9.45E+00	2.95E+00
	130	40000	66	9.78E+00	2.87E+00
	170	45700	66	9.84E+00	2.90E+00
Glycerol	3	3420	649	8.86E+00	3.49E+00
	16	3420	144	1.10E+01	3.12E+00

Table A.10 Liquid Column Trajectories:

Liquid	We_∞	Re_{Ld}	q	$x/(d_j\ q)$	$y/(d_j\ q)$
Water	161	19200	12	7.41E-03	9.51E-02
				1.96E-02	1.90E-01
				3.41E-02	2.85E-01
				5.01E-02	3.80E-01
				7.65E-02	4.75E-01
				1.17E-01	5.70E-01
				1.70E-01	6.65E-01
				2.31E-01	7.60E-01
				3.23E-01	8.56E-01
				5.02E-01	9.51E-01
	161	90200	272	2.12E-03	8.02E-02
				3.86E-03	9.09E-02
				5.79E-03	1.02E-01
				8.55E-03	1.12E-01
				9.99E-03	1.23E-01
				1.10E-02	1.34E-01
				1.44E-02	1.44E-01
				1.73E-02	1.55E-01
				1.37E-02	1.66E-01
				1.02E-02	1.77E-01
	161	140000	653	3.27E-04	3.07E-02
				3.47E-04	3.63E-02
				6.72E-04	4.18E-02

Liquid	We_{∞}	Re_{Ld}	q	$x/(d_j\ q)$	$y/(d_j\ q)$
				1.06E-03	4.74E-02
				1.63E-03	5.30E-02
				1.91E-03	5.86E-02
				2.62E-03	6.42E-02
				3.10E-03	6.97E-02
				4.43E-03	7.53E-02
				5.49E-0	8.09E-02
Ethanol	161	40200	330	4.75E-04	3.85E-02
				1.18E-03	4.95E-02
				1.84E-03	6.05E-02
				2.76E-03	7.15E-02
				3.77E-03	8.25E-02
				5.44E-03	9.36E-02
				6.89E-03	1.05E-01
				6.89E-03	1.16E-01
				1.14E-02	1.27E-01
				1.41E-02	1.38E-01
Glycerol	161	3420	15	5.42E-03	5.42E-02
				1.25E-02	1.08E-01
				2.06E-02	1.63E-01
				2.98E-02	2.17E-01
				4.34E-02	2.71E-01
				5.97E-02	3.25E-01
				7.76E-02	3.80E-01
				9.98E-02	4.34E-01
				1.32E-01	4.88E-01
				1.78E-01	5.42E-01
Water	70	19200	28	3.81E-03	6.21E-02
				8.24E-03	1.24E-01
				1.66E-02	1.86E-01
				2.79E-02	2.49E-01
				4.43E-02	3.11E-01
				5.81E-02	3.73E-01
				8.49E-02	4.35E-01
				1.23E-01	4.97E-01
				1.61E-01	5.59E-01
				1.56E-01	4.97E-01
	70	90200	621	4.82E-04	3.50E-02
				7.78E-04	3.97E-02
				8.78E-04	4.44E-02
				1.40E-03	4.90E-02
				1.91E-03	5.37E-02
				2.19E-03	5.84E-02

Liquid	We_∞	Re_{Ld}	q	$x/(d_j\ q)$	$y/(d_j\ q)$
				2.90E-03	6.30E-02
				3.55E-03	6.77E-02
				4.45E-03	7.24E-02
				5.33E-03	7.70E-02
	70	140000	1490	2.02E-04	2.56E-02
				4.54E-04	2.93E-02
				5.60E-04	3.29E-02
				7.92E-04	3.66E-02
				9.66E-04	4.02E-02
				1.45E-03	4.39E-02
				1.55E-03	4.75E-02
				2.14E-03	5.12E-02
				2.54E-03	5.48E-02
				3.25E-03	5.85E-02
Ethanol	70	40200	756	4.62E-04	2.64E-02
				9.46E-04	3.51E-02
				1.38E-03	4.37E-02
				2.03E-03	5.24E-02
				2.78E-03	6.10E-02
				3.95E-03	6.97E-02
				4.15E-03	7.83E-02
				5.59E-03	8.70E-02
				7.28E-03	9.56E-02
				9.27E-03	1.04E-01
Glycerol	70	3420	34	5.67E-03	5.32E-02
				1.09E-02	1.06E-01
				1.91E-02	1.59E-01
				3.02E-02	2.13E-01
				4.61E-02	2.66E-01
				6.95E-02	3.19E-01
				9.36E-02	3.72E-01
				1.29E-01	4.25E-01
				1.73E-01	4.78E-01
				2.32E-01	5.32E-01
Water	16	19200	118	2.62E-03	3.93E-02
				4.61E-03	7.86E-02
				8.07E-03	1.18E-01
				1.39E-02	1.57E-01
				2.26E-02	1.97E-01
				3.58E-02	2.36E-01
				4.74E-02	2.75E-01
				6.73E-02	3.15E-01
				7.59E-02	3.32E-01

Liquid	We_∞	Re_{Ld}	q	$x/(d_j\ q)$	$y/(d_j\ q)$
				2.61E-02	7.86E-02
	16	90200		1.01E-04	2.05E-02
				1.23E-04	2.26E-02
				1.68E-04	2.47E-02
				2.18E-04	2.68E-02
				4.44E-04	2.89E-02
				4.09E-04	3.10E-02
				6.24E-04	3.32E-02
				8.21E-04	3.53E-02
				1.00E-03	3.74E-02
				1.52E-03	3.95E-02
	16	140000	6280	5.33E-05	1.24E-02
				9.85E-05	1.33E-02
				8.51E-05	1.42E-02
				2.32E-04	1.50E-02
				1.46E-04	1.59E-02
				1.78E-04	1.68E-02
				3.25E-04	1.76E-02
				3.64E-04	1.85E-02
				3.78E-04	1.94E-02
				6.00E-04	2.02E-02
Ethanol	16	40200	3180	2.05E-04	1.60E-02
				2.95E-04	1.83E-02
				3.23E-04	2.06E-02
				3.30E-04	2.28E-02
				6.10E-04	2.51E-02
				8.46E-04	2.74E-02
				7.57E-04	2.97E-02
				8.94E-04	3.20E-02
				1.13E-03	3.43E-02
				1.44E-03	3.65E-02
Glycerol	16	3420	144	1.29E-03	2.53E-02
				2.97E-03	5.05E-02
				5.16E-03	7.58E-02
				8.47E-03	1.01E-01
				1.23E-02	1.26E-01
				1.74E-02	1.52E-01
				2.51E-02	1.77E-01
				3.42E-02	2.02E-01
				5.08E-02	2.27E-01
				6.53E-02	2.53E-01

APPENDIX B

UNCERTAINTY ANALYSIS

B.1 General Formulation

In the present study, estimates of overall uncertainties based on t distribution were obtained following the analysis of Crow et al. (1960). In this analysis, the variable X, which is the measured quantity, is considered for the uncertainty analysis. This method assumed that the sample is a random one with the measurements following a normal distribution. The mean value $\overline{X}$ obtained from the measurements is given as follows:

$$\overline{X} = \frac{\sum_{i=1}^{n} x_i}{n} \tag{B.1}$$

where, x_i's are the variables in the measurements and n is the number of samples of data. Then, the uncertainty of the result is then given by the following expression:

$$u = \pm t_{\alpha/2,n-1} \frac{s}{\sqrt{n}} \tag{B.2}$$

where, $(1 - \alpha)$ = the confidence level

s = the standard deviation

n = the number of samples of data

t denotes the t-distribution (Refer to Crow et al., 1960)

The standard deviation of n samples of data (refer to Crow et al., 1960) is given as follows:

$$s = \sqrt{\frac{\sum_{i=1}^{n} (x_i - \overline{X})^2}{n-1}} \tag{B.3}$$

For present measurements, all the uncertainties reported are taken to be those for the 95% confidence level, i.e.

$$(1 - \alpha) = 0.95 \tag{B.4}$$

B.2 Uncertainties of the Measured Quantities

For the present study, all measurements obtained using the imaging system were made initially in pixel dimensions and then converted to a length scale. Therefore, the uncertainty of the calibration measurement affects the uncertainty of all other measurements. The lowest magnification used during the present study was 1.9x and that yielded a maximum uncertainty value of 3.3% when converting the pixel dimensions to length scale. The following section details the uncertainties in various measurements for the present study.

B.2.1 Uncertainties for Location of Onset of Breakup

The location of onset of breakup was measured by measuring the distance from the jet exit to the location of appearance of first ligament. Measurements from different images were averaged using Eqn. (B.1) and the uncertainty was determined using Eqns. (B.2) and (B.3). The minimum and maximum uncertainty values for the location of onset

of breakup were found to be 6% and 74% at 95% confidence level. The average uncertainty was found to be 54%.

Time of onset of breakup was found by using the assumption that ligaments convect along the liquid jet surface with the liquid jet velocity, v_j. The minimum and maximum uncertainty values for the location of onset of breakup were found to be 30% and 84% at 95% confidence level. The average uncertainty was found to be 56%.

B.2.2 Uncertainties for Ligament and Drop sizes

Ligament diameters for downwind and upwind side at onset were measured at four different locations along the ligament length and then averaged them to find the average ligament diameter. The mean of the averaged ligament diameter were determined using Eqn. (B.1) and the uncertainty was determined using Eqns. (B.2) and (B.3). The minimum and maximum uncertainty values for the ligament diameter at the onset on downwind side were found to be 12% and 86% at 95% confidence level. The average uncertainty was found to be 32%. For the upwind side, the minimum and maximum uncertainty values for the ligament diameter at the onset were found to be 6% and 44% at 95% confidence level and the average uncertainty was found to be 20%.

Drop diameters for downwind and upwind side at onset were determined based on the assumption drops are perfectly spherical and that the surface area of the actual ellipsoidal drop is equal to the surface area of the spherical drop. Then, the major and minor diameters of the 2-D ellipse were measured and then the average drop diameter was found using:

$$d_p = \sqrt{d_{max} \text{ x } d_{min}} \tag{B.5}$$

where, d_{max} = the maximum diameter measured for a drop

d_{min} = the minimum diameter measured for the drop

The mean value of the measured drop diameter was determined using Eqn. (B.1) and the uncertainty was determined using Eqns. (B.2) and (B.3). The minimum and maximum uncertainty values for the drop diameter at the onset on downwind side were found to be 11% and 75% at 95% confidence level. The average uncertainty was found to be 30%. For the upwind side, the minimum and maximum uncertainty values for the drop diameter at the onset were found to be 18% and 62% at 95% confidence level and the average uncertainty was found to be 32%.

Sauter mean diameter (SMD) was defined by the following equation:

$$SMD \equiv \sum_{i=1}^{n} d_{pi}^3 / \sum_{i=1}^{n} d_{pi}^2 \qquad (B.6)$$

Measurements for drop diameters for finding out the SMD was performed in the same manner as previously discussed for drop size measurements at onset. The minimum and maximum uncertainty values for the SMD measurements at the onset were found to be 1% and 81% at 95% confidence level and the average uncertainty was found to be 40%.

B.2.3 Uncertainties for Liquid Core Breakup Length

Measurements for the location of the liquid core breakup involved locating the point where the complete fracture of the liquid core occurred. The streamwise location of the end of liquid core was measured from the jet exit was converted into breakup time based on the assumption that the surface of the jet convets with the jet velocity.

Crosswise location was measured as a length scale from the jet exit. The mean value of the measured breakup times and locations were determined using Eqn. (B.1) and the uncertainty was determined using Eqns. (B.2) and (B.3). The minimum and maximum uncertainty values for the time of breakup of liquid core in streamwise direction were found to be 0.3% and 24% at 95% confidence level. The average uncertainty was found to be 9%. Measurements of crosswise distances from the jet exit yielded minimum and maximum uncertainty values to be 5% and 32% and the average uncertainty value of 20%.

B.2.4 Uncertainties for Liquid Column Trajectories

Measurements for liquid column trajectories were performed by measuring the x- and the y-location along the liquid jet for ten different locations along the liquid jet. The measured values fore the same test conditions were averaged and the mean value and the uncertainties were found using Eqns. (B.1), (B.2) and (B.3) respectively. The minimum and maximum uncertainty values for the liquid column trajectories were found to be 3% and 88% at 95% confidence level and the average uncertainty was found to be 26%.

VITA

Ramprakash Sankarakrishnan

Candidate for the Degree of

Master of Science

Thesis: BREAKUP OF TURBULENT ROUND LIQUID JETS IN UNIFORM GASEOUS CROSSFLOW

Major Field: Mechanical and Aerospace Engineering

Biographical:

Education:

Received Bachelor of Engineering degree in Mechanical Engineering from Sri Venkateswara College of Engineering (affiliated to the University of Madras, Chennai, India) in April 2003. Completed the requirements for the Master of Science degree with a major in Mechanical and Aerospace Engineering at Oklahoma State University, Stillwater, Oklahoma in December, 2005.

Experience:

1. Graduate Research Assistant: 12/2003 to present, School of Mechanical and Aerospace Engineering, Oklahoma State University, Stillwater, OK. Conduct an experimental investigation of breakup of turbulent round liquid jets in uniform gaseous crossflow using laser diagnostics. Research objectives involve measurements of breakup regime transitions and ligament behavior, discovering the effect of turbulence on breakup mechanisms and developing methods to obtain spray size at the nano scale. Responsibilities include: setting up optical arrangement for double-pulsed shadowgraphy and holography, specifying and purchasing a wind tunnel, high-pressure air compressor and air-tank, pulse generator, CCD camera, a complete PIV system, design of nozzles and test chamber, building test chamber enclosure and installing high pressure air-lines. The research is supported by the NSF-EPSCoR.

2. Graduate Teaching Assistant: 08/2004 to 05/2005, School of Mechanical and Aerospace Engineering, Oklahoma State University, Stillwater. Responsibilities include: setting up new lab experiments, designing lab manuals, conducting fluid flow laboratory sessions, holding office hours, grading homework, quizzes, projects, and exams, conducting problem session lectures, and mid-term exams. Courses handled: Compressible Fluid Flow, and Experimental Fluid Dynamics.

3. Undergraduate Training and placement Assistant: 05/2002 to 05/2003, Dept of Mechanical Engineering, SVCE, India. Responsibilities include: inviting companies to the campus, informing students of the incoming job interviews and listing candidates for appearance in interviews.

Honors and Awards:

1. Among the top 3 positions in the 23rd Annual Phoenix Award for the Outstanding Master's Student. (April 2005)

2. University of Madras Gold medalist in the Department of Mechanical engineering in the undergraduate program. (1999-2003)

3. Awarded "THE SIR GABRIEL STOKES AWARD" & "THE Dr. A.L. MUDALIAR AWARD" for undergraduate engineering. (2003)

4. Awarded Scholarship & Grant for 5000 INR from University of Madras for being in the Top 2 Ranks in the Mechanical Department. (February 2003)

5. Awarded the 2nd Best Final year Project Award for undergraduate engineering in the Mechanical Engineering Department for the academic year 2002-2003

Professional Memberships:

Member of the American Society of Mechanical Engineers (ASME), Member of the American Physical Society (APS).

Name: Ramprakash Sankarakrishnan Date of Degree: December, 2005

Institution: Oklahoma State University Location: Stillwater, Oklahoma

Title of Study: BREAKUP OF TURBULENT ROUND LIQUID JETS IN UNIFORM GASEOUS CROSSFLOW

Pages in Study: 101 Candidate for the Degree of Master of Science

Major Field: Mechanical and Aerospace Engineering

Scope and Method of Study: An experimental investigation of breakup of partially and fully turbulent round liquid jets in uniform gaseous crossflow was undertaken. Measurements of the properties of primary breakup were obtained using pulsed shadowgraphy. A turbulent round liquid jet was injected vertically in a 12"x12" subsonic wind tunnel having a contraction ratio greater than 16:1 with test section velocities of 3-62.5 m/s at normal temperature and pressure. Test conditions included various liquids (water, ethyl alcohol, and glycerol), nozzle with large length/diameter ratios (L/d > 40), liquid jet exit diameter of 2 mm, crossflow Weber numbers of 0-180, liquid/gas momentum ratios of 5-55,000, liquid jet Ohnesorge numbers of 0.002-0.014, and jet Reynolds number of 2000-140,000 in uniform crossflow typical of afterburners in jet engines. Measurements included developing a breakup regime map, conditions required for the onset of breakup, ligament properties along the liquid surface, drop size after primary breakup along the liquid surface, conditions required for breakup of the liquid jet as a whole, and liquid jet trajectories. Phenomenological analyses were used to interpret and correlate the new measurements.

Findings and Conclusions: The breakup of turbulent liquid jets in gaseous crossflow could be classified into two breakup regimes namely turbulent breakup regime and aerodynamic breakup regime. This classification is based on a dimensionless parameter $We_{L\Lambda}q^{1/3}$. Turbulent liquid jets in crossflow exhibit breakup regimes similar to the nonturbulent liquid jets in uniform gaseous crossflow for $We_{L\Lambda}q^{1/3} <$ 17,000. Turbulent primary breakup dominated the surface breakup mechanism for turbulent jets with $We_{L\Lambda}q^{1/3} >$ 17,000. Drop sizes increased with streamwise distance from jet exit. The drop size at the onset of breakup was found to remain a constant regardless of the level of liquid turbulence. Drop to ligament size ratio were typical of Rayleigh breakup mechanism for the ligaments. For turbulent breakup the ligament and drop sizes at the onset of breakup in the upwind and downwind side were similar indicating weak crossflow effects. Locations and times for liquid core breakup were found to be similar to nonturbulent liquid jets in uniform gaseous crossflow. Liquid column trajectories in the shear breakup regime were similar for turbulent jets and non-turbulent jets in uniform gaseous crossflow. However, within the bag and multimode breakup regimes, the turbulent liquid jets penetrated more than nonturbulent liquid jets.

ADVISER'S APPROVAL: Khaled A. Sallam